

THESIS FOR THE DEGREE OF DOCTOR OF PHILOSOPHY

**Polymer-Nanoparticle Hybrid Materials for Plasmonic Hydrogen Detection**

IWAN DARMADI

Department of Physics

CHALMERS UNIVERSITY OF TECHNOLOGY

Gothenburg, Sweden 2021

# **Polymer-Nanoparticle Hybrid Materials for Plasmonic Hydrogen Detection**

IWAN DARMADI

ISBN 978-91-7905-453-3

©IWAN DARMADI, 2021.

Doktorsavhandlingar vid Chalmers tekniska högskola

Ny serie nr 4920

ISSN 0346-718X

Department of Physics

Chalmers University of Technology

SE-412 96 Gothenburg

Sweden

Telephone + 46 (0)31-772 1000

Cover:

Schematic illustration of the synergies between plasmonic nanoparticles and polymers that I explored to contribute to the safety of hydrogen energy technology.

(Parts of the illustration were obtained from the free-licensed resources designed by *Freepik* and *Rawpixel* from [www.freepik.com](http://www.freepik.com)).

Printed by Chalmers Reproservice

Gothenburg, Sweden 2021

# Polymer-Nanoparticle Hybrid Materials for Plasmonic Hydrogen Detection

Iwan Darmadi

Department of Physics

Chalmers University of Technology

## Abstract

Plasmonic metal nanoparticles and polymer materials have independently undergone rapid development during the last two decades. More recently, it has been realized that combining these two systems in a hybrid or nanocomposite material comprised of plasmonically active metal nanoparticles dispersed in a polymer matrix leads to systems that exhibit fascinating properties, and some first attempts had been made to exploit them for optical spectroscopy, solar cells or even pure art. In my thesis, I have applied this concept to tackle the urgent problem of hydrogen safety by developing Pd nanoparticle-based “plasmonic plastic” hybrid materials, and by using them as the active element in optical hydrogen sensors. This is motivated by the fact that hydrogen gas, which constitutes a clean and sustainable energy vector, poses a risk for severe accidents due to its high flammability when mixed with air. Therefore, hydrogen leak detection systems are compulsory in the imminent large-scale dissemination of hydrogen energy technologies. To date, however, there are several unresolved challenges in terms of hydrogen sensor performance, whereof too slow sensor response/recovery times and insufficient resistance towards deactivation by poisoning species are two of the most severe ones. In this thesis, I have therefore applied the plasmonic plastic hybrid material concept to tackle these challenges. In summary, I have (i) developed hysteresis-free plasmonic hydrogen sensors based on PdAu, PdCu and PdAuCu alloy nanoparticles; (ii) demonstrated ultrafast sensor response and stable sensor operation in chemically challenging environments using polymer coatings; (iii) introduced bulk-processed and 3D printed plasmonic plastic hydrogen sensors with fast response and high resistance against poisoning and deactivation.

*Keywords: nanoplasmonic, polymer, hybrid material, hydrogen, sensor, palladium, alloy, nanofabrication, nanocomposite*

## List of Appended Papers

This thesis is based on work presented in the following papers:

- I. *Universal Scaling and Design Rules of Hydrogen-Induced Optical Properties in Pd and Pd-Alloy Nanoparticles*  
F. A. A. Nugroho, I. Darmadi, V. P. Zhdanov, and C. Langhammer  
*ACS Nano*, 2018, 12 (10), 9903–9912.
- II. *Rationally Designed PdAuCu Ternary Alloy Nanoparticles for Intrinsically Deactivation-Resistant Ultrafast Plasmonic Hydrogen Sensing*  
I. Darmadi\*, F. A. A. Nugroho\*, S. Kadkhodazadeh, J. B. Wagner, and C. Langhammer.  
(\*equal contribution)  
*ACS Sensors*, 2019, 4, 5, 1424–1432.
- III. *Systematic Composition Optimization of PdAuCu Ternary Alloy Nanoparticles for Plasmonic Hydrogen Sensing*  
I. Darmadi, S. Zulfa Khairunnisa, D. Tomeček and C. Langhammer  
*In manuscript*.
- IV. *Metal–Polymer Hybrid Nanomaterials for Plasmonic Ultrafast Hydrogen Detection*  
F. A. A. Nugroho, I. Darmadi, L. Cusinato, A. Susarrey-Arce, H. Schreuders, L. J. Bannenberg, A. B. da Silva Fanta, S. Kadkhodazadeh, J. B. Wagner, T. J. Antosiewicz, A. Hellman, V. P. Zhdanov, B. Dam and C. Langhammer  
*Nature Materials*, 2019, 18, 489–495.
- V. *Impact of Surfactants and Stabilizers on Palladium Nanoparticle–Hydrogen Interaction Kinetics: Implications for Hydrogen Sensors*  
A. Stolaś\*, I. Darmadi\*, F. A. A. Nugroho, K. Moth-Poulsen\*, and C. Langhammer.  
(\*equal contribution)  
*ACS Applied Nano Materials*, 2020, 3, 3, 2647–2653.
- VI. *Bulk-Processed Pd Nanocube–Poly(methyl methacrylate) Nanocomposites as Plasmonic Plastics for Hydrogen Sensing*  
I. Darmadi\*, A. Stolaś\*, I. Östergren\*, B. Berke, F. A. A. Nugroho, M. Minelli, S. Lerch, I. Tanyeli, A. Lund, O. Andersson, V. P. Zhdanov, M. Liebi, K. Moth-Poulsen, C. Müller and C. Langhammer (\*equal contribution)  
*ACS Applied Nano Materials*, 2020, 3, 8, 8438–8445.
- VII. *A Highly Hydrogen Permeable Fluorinated Polymer-Pd Nanoparticle Nanocomposite for Plasmonic Hydrogen Sensing*  
I. Östergren\*, A. M. Pourrahimi\*, I. Darmadi\*, R. R. da Silva, A. Stolaś, S. Lerch, B. Berke, M. Liebi, M. Minelli, K. Moth-Poulsen, C. Langhammer and C. Müller (\*equal contribution)  
*Submitted manuscript*.

- VIII. *Colloidal Synthesis of Palladium-Gold Alloy Nanoparticles for Hydrogen Sensing*  
S. Lerch, A. Stolaś, I. Darmadi, X. Wen, M. Strach, C. Langhammer, K. Moth-Poulsen  
*Submitted manuscript.*
- IX. *High-Performance Nanostructured Palladium-Based Hydrogen Sensors—Current Limitations and Strategies for Their Mitigation*  
I. Darmadi, F. A. A. Nugroho, and C. Langhammer\*  
*ACS Sensors, 2020, 5, 11, 3306–3327. (Perspectives paper)*

## **My Contribution to the Appended Papers**

### *Paper I*

I did the nanofabrication, material characterization, experiments and data analysis for the PdCu part.

### *Paper II*

I did the nanofabrication, material characterization (XPS, SEM), sensing tests, data analysis, and wrote the first draft of the manuscript.

### *Paper III*

I supervised S. Z. Khairunnisa during her master thesis project, which forms the basis of this work and I wrote the first draft of the manuscript.

### *Paper IV*

I did the nanofabrication, sensing tests and data analysis for the PMMA and PTFE/PMMA tandem part.

### *Paper V*

I did the nanofabrication, material characterization (XPS, SEM), sensing tests, data analysis, and wrote the first draft of the manuscript.

### *Paper VI*

I did the sensing tests, data analysis, and wrote the first draft of the manuscript.

### *Paper VII*

I did the sensing tests, data analysis, and assisted in the writing of the manuscript.

### *Paper VIII*

I did the sensing tests and data analysis.

### *Paper IX*

I did the literature study and wrote the first draft of the manuscript.

## Related Publications not Included in This Thesis

- I. *A Nanofabricated Plasmonic Core–Shell-Nanoparticle Library*  
A. Susarrey-Arce, K. M. Czajkowski, I. Darmadi, S. Nilsson, I. Tanyeli, S. Alekseeva,  
T. J. Antosiewicz and C. Langhammer  
*Nanoscale*, 2019, 11, 21207–21217.
  
- II. *Dual-Peak Plasmonic Nanorulers*  
F. A. A. Nugroho, D. Świtlik, A. Armanious, P. O’Reilly, I. Darmadi, S. Nilsson, V. P.  
Zhdanov, F. Hook, T. J. Antosiewicz and C. Langhammer  
*In manuscript*.





## Contents

Chapter 1 - Introduction .....	1
1. Why Hydrogen Sensors? .....	3
1.1. Hydrogen Economy and Hydrogen Safety .....	3
1.2. Hydrogen Safety Sensors: Challenges and State of the Art .....	4
2. This Thesis: The Strategy and the Outline.....	6
Chapter 2 - Palladium-Hydrogen Interactions .....	9
1. Palladium-Hydrogen Interactions and Hydride Formation .....	9
1.1. Consequences of Pd Nanostructuring to Hydrogen Sorption Kinetics and Isotherm..	12
1.2. Pd Surface Modification Effects to Hydrogen Sorption Kinetics .....	14
1.3. Implications of Carbon Monoxide (CO) Poisoning to Hydrogen Sorption Kinetics.....	15
2. Palladium-Coinage Metal Alloys.....	16
2.1. The Pd-Alloy Structure.....	16
2.2. Pd-Alloy Hydrides.....	17
2.3. Alloy Stability: Surface Segregation .....	18
Chapter 3 - Nanoplasmonic Sensing .....	21
1. Palladium-Hydride Optical Properties.....	21
2. Localized Surface Plasmon Resonance (LSPR).....	22
3. LSPR-based Pd Hydrogen Sensors.....	23
Chapter 4 - Gas Transport in Polymers .....	27
1. Gas Transport Through Polymer Membranes: Solution-Diffusion Theory .....	27
1.1. Gas Transport from a Microscopic Point of View .....	29
1.1.1. Gas Diffusivity and Solubility.....	29
1.1.2. PMMA and Amorphous Fluorinated Polymers .....	30
2. Permeability-Selectivity Trade-off.....	31

3. Gas Transport through Polymer Thin Films.....	31
4. H <sub>2</sub> Sorption Kinetics in Pd-nanoparticles:Polymer 3D Sensors .....	33
Chapter 5 - Nanoparticle-Polymer Hybrid Material Fabrication and Processing.....	35
1. Metallic Nanoparticle Synthesis: Top-down vs Bottom-up.....	36
2. Embedding Nanoparticles in a Polymer Matrix.....	38
3. Hole-Mask Colloidal Lithography (HCL) .....	40
3.1. Alloying via Annealing .....	42
3.2. Applying a Polymer Thin Film Coating on the Nanofabricated Surface.....	42
4. Bulk-Processing of Pd Nanoparticle-Polymer Hybrid Materials.....	44
4.1. Colloidal Synthesis of Pd Nanocubes .....	44
4.2. Nanoparticle-Polymer Hybrid Material Compounding.....	44
4.3. Post-Processing: Melt-Pressing of Thin Plates or 3D printing.....	45
Chapter 6 - Material Characterization .....	47
1. Scanning Electron Microscopy (SEM).....	48
2. Energy Dispersive X-Ray Spectroscopy (EDX).....	49
3. Transmission Electron Microscopy (TEM).....	50
4. X-Ray Photoelectron Spectroscopy (XPS).....	51
5. Quartz Crystal Microbalance (QCM).....	52
6. Small Angle X-ray Scattering (SAXS).....	53
Chapter 7 Hydrogen Sensor Test Setups.....	55
1. Vacuum Chamber .....	55
2. Atmospheric Pressure Flow Reactor (Insplorion X1) .....	57
3. The Fiber Optic Feedthrough Reactor.....	58
4. Fast-Switch Mini Reactor .....	59

Chapter 8 – Conclusion and Outlook.....	63
1. Conclusion .....	63
2. Next Steps .....	64
2.1. 2D sensors .....	64
2.2. 3D sensors .....	65
3. Outlook.....	65
Acknowledgement.....	67
References .....	69



## List of Abbreviations

CTAB	Cetyltrimethylammonium bromide
CTAC	Cetyltrimethylammonium chloride
CVD	Chemical vapor deposition
LSPR	Localized surface plasmon resonance
PE-RIE	Plasma-enhanced reactive ion etching
PLA	Poly(lactic acid)
PMMA	Poly(methyl methacrylate)
PTFE	Polytetrafluoroethylene
PVD	Physical vapor deposition
PVP	Polyvinylpyrrolidone
TOAB	Tetraoctylammonium bromide

# Chapter 1 - Introduction

Nanoplasmonic-polymer hybrid materials that are the focus of this thesis offer almost limitless potential for a wide range of applications, thanks to the fact that they rely on a large “library” of material properties provided by the plasmonic nanoparticle and polymer constituents. These two classes of materials have been studied independently and developed intensively during recent years, which promises a high level of rational design opportunities to tailor nanoplasmonic-polymer hybrid materials for a specific application.

*The first ingredient*, plasmonic metal nanoparticles in the sub-100 nm size range, have been created by humans for many centuries. It started in the Roman era in the 4<sup>th</sup> century AD, when such nanoparticles were used as a dye in artwork, such as stained glass windows, cups, and tesserae, i.e. small square tiles used in colorful mosaics.<sup>1</sup> Their application has been limited to art until the age of modern science in the 19<sup>th</sup> century, when Gustav Mie (1868-1957) developed the first theoretical understanding of the beautiful coloring obtained upon interaction of noble metal nanoparticles with light.<sup>2</sup> The theoretical understanding revealed great potential for more technical applications, which finally were enabled by the rapid development of nanofabrication and characterization techniques during the last three decades. Since, the dynamic field of nanoplasmonics has developed and diversified rapidly and plasmonic nanoparticles today find application in sensors, catalysis, spectroscopy, solar cells and medicine,<sup>3-7</sup> and they come in a large variety of materials, shapes, and sizes.<sup>8-10</sup>

*The second ingredient*, polymer, is another class of materials that is used in almost all sectors of human life today due to their unique properties: low cost, lightness, ease to process, excellent thermal/electrical insulation, and high corrosion resistance, to name a few. Like for plasmonic nanoparticles, polymer materials had been used before the modern era. Long before the term “polymer” was coined, ancient cultures, like for example Mesoamericans in 1600 BC, utilized natural rubber to make bands, balls or figurines.<sup>11</sup> However, just like with nanoplasmonics, our ability to manipulate polymers systematically began with the dawn of polymer science and engineering in the 20<sup>th</sup> century, whereof polystyrene (PS) and polyvinyl chloride (PVC) that are heavily used polymers today, are two good examples of the earliest synthesized polymers.<sup>12</sup> The present detailed knowledge about how to tailor polymer materials has emerged from the simple concept of combining monomers into long polymer chains.

The rich chemical and physical features of both (plasmonic) nanoparticles and polymers make it intrinsically attractive to attempt to combine both systems in one and the same *hybrid* material, with the anticipated outcome to enhance overall material performance, to alleviate an inherent weakness of one of the components, or to create completely new functionality. Driven by these prospects, numerous forms of hybrid materials comprising nanoparticles and polymers have been crafted, and to embed plasmonic metal nanoparticles in a polymer matrix is one of the *foci* of my thesis. This is motivated by a number of factors. For example, it is known that the plasmonic near field is enhanced by the polymer coating.<sup>13,14</sup> This effect is for example employed in nanoplasmonic sensing and surface-enhanced Raman spectroscopy (SERS).<sup>15-18</sup> Furthermore, a polymer matrix can be utilized to prevent nanoparticle aggregation or to protect the metallic nanoparticle from oxidation and contaminants, or as a “molecular sieve”.<sup>19,20</sup> These functions are crucial for many plasmonic systems, as for example Ag

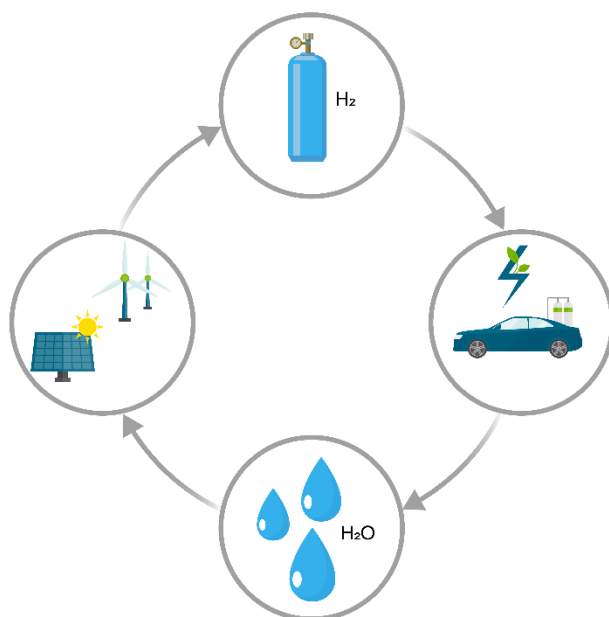
nanoparticles are prone to oxidize. The sieving function is attractive for sensing and catalysis applications. Beyond these traits, a polymer matrix adds functionality to the hybrid material thanks to, for example, its optical transparency, mechanical flexibility and scalable and cost-effective processing. Furthermore, with the polymer in the form of a light- or pH-sensitive hydrogel, plasmonic-polymer hybrid materials have been successfully used for data recording and plasmonic display applications.<sup>21,22</sup>

Considering the outlined potential of nanoplasmonic-polymer hybrid materials, in the *first track* of this thesis, I have applied this concept on 2-dimensional (2D) nanofabricated Palladium (Pd) nanoparticle-based hydrogen sensors with the aim (i) to accelerate sensor response/recovery times; (ii) to enable sensor operation in the presence of poisoning/deactivating species like carbon monoxide (CO); and (iii) to create hysteresis-free sensor response. To achieve this performance, I rationally designed and optimized the hybrid material structure at all levels, i.e., from the nanoparticles to the nanoparticle-polymer interface, to the chosen polymer materials themselves. Specifically, at the nanoparticle level, I experimented with nanoparticle size to optimize the response/recovery time, and with alloying with Gold (Au) to suppress the hysteresis, and with Copper (Cu) to promote the poisoning resistance. At the nanoparticle-polymer interface level, I studied the effect of different polymer coatings on hydrogen ab/desorption kinetics into the nanoparticles. Finally, at the polymer level, I studied the molecular sieving properties of poly(methyl methacrylate) – PMMA – and polytetrafluoroethylene – PTFE – in combination with the identified “best” alloy nanoparticles.

In the *second track* of this thesis, I focused on transferring the developed hydrogen sensor platform from its 2D nanofabrication based version to a more scalable scheme based on colloidal synthesis of the plasmonic Pd nanoparticles and bulk polymer processing for the creation of hydrogen sensor signal transducers based on nanoparticle-polymer hybrid materials. The use of colloidally synthesized nanoparticles is not only interesting from a scalability point of view, but also from the perspective that it offers ample opportunities to create nanoparticles with high crystallinity, controlled shapes and faceting, and more complex structures like core-shell architectures. Finally, to advance the hybrid material concept for hydrogen sensor applications closer to a real application, I demonstrated the possibility to use the developed hybrid materials as a precursor for 3D printing of plug-and-play hydrogen sensor caps compatible with off-the-shelf fiber optics and a commercial hydrogen sensor prototype device.

# 1. Why Hydrogen Sensors?

## 1.1. Hydrogen Economy and Hydrogen Safety



*Scheme 1: Hydrogen economy concept:  $H_2$  is the energy vector. It is produced by splitting water molecules using energy produced from sustainable resources. In a fuel-cell,  $H_2$  and  $O_2$  are then recombined, thereby generating electricity and only water as by-product in a sustainable energy cycle (parts of the illustration were obtained from free-licensed resources in ref.<sup>23</sup>).*

Global warming is an alarming and serious issue, which already has started to affect our ecosystem and social life.<sup>24</sup> Being a person who enjoys the underwater world, I have personal concerns since the only 1°C temperature rise in the past decades has already damaged large areas of coral reefs around the world.<sup>25,26</sup> In an attempt to keep the global warming below 2°C, in 2010 all countries through the Intergovernmental Panel on Climate Change (IPCC) have agreed to cut the CO<sub>2</sub> emission by at least half by 2030 and to net zero by 2050.<sup>27</sup> Several solutions have been proposed to accelerate the emission cut, whereof one is to implement a so-called hydrogen economy.

In the hydrogen economy concept, hydrogen plays the role as the main energy carrier (**Scheme 1**).<sup>28–30</sup> Within a fuel cell device, hydrogen reacts with oxygen and generates electricity with pure water as the only byproduct. This is in contrast to the conventional fossil fuels, which emit CO<sub>2</sub>, health-damaging pollutants such as CO, NO<sub>x</sub>, and solid particulates upon combustion in an internal combustion engine or a gas turbine. In the ideal scenario of the hydrogen economy, hydrogen production is to be done in a sustainable way, for example by water electrolysis using renewable energy resources like solar cells or wind turbines. To promote the hydrogen economy development in Sweden, for example, The Swedish Foundation of Strategic Research (SSF) has recently granted 50 million Swedish kronor (~ 5 million Euro) to a large research effort encompassing the production, use, and storage of hydrogen gas.<sup>31</sup>



Despite these recently intensified efforts, before a large-scale implementation of hydrogen as energy carrier, numerous challenges along the entire hydrogen value chain – from hydrogen production, to transport, storage, usage in fuel-cells to safety – need to be overcome. My project contributes to this quest by developing hydrogen sensors for safety systems that will have to be deployed at a large scale along the entire value chain. Hydrogen safety systems are critical for a hydrogen economy because hydrogen has a wide flammability range (4-75 vol.%) and low ignition energy (0.02 mJ) when mixed with air.<sup>32,33</sup> The flammability limit of other flammable gases like methane and propane are 5-15 and 2-10 vol.% respectively.<sup>34</sup> In addition, both methane and propane require ignition energy in the order of 0.1 mJ.<sup>35</sup> Furthermore, hydrogen gas is odorless and transparent, as well as prone to leak; therefore, high speed sensors are critical for leak detection. A very recent example for the importance of hydrogen safety systems is the hydrogen explosion accident in one of Norway’s hydrogen filling stations due to a high-pressure storage leak, which took place in 2019.<sup>36,37</sup>

## 1.2. Hydrogen Safety Sensors: Challenges and State of the Art

	Stationary	Automotive
Dynamic range [vol.%]	≤ 4	≤ 4
Detection limit [vol.%]	≤ 4	0.1
Response/recovery time [s]	< 30 / < 30	< 1 / < 1
Accuracy [%]	± 10	± 5
Power consumption [W]	N.A.	< 1
Lifetime	3 - 5 years	6000 hours
Ambient temperature [°C]	-50 to +50	-40 to +85
Ambient pressure [kPa]	80 to 110	62 to 107
Ambient humidity [%]	20 to 80	0 to 95

Scheme 2: Technical requirements for hydrogen safety sensors for automotive and stationary applications<sup>38</sup> (parts of the illustration were obtained from free-licensed resources in ref.<sup>23</sup>).

In 2007, the National Renewable Energy Laboratory (NREL) and the United States Department of Energy (US DOE) arranged a workshop attended by hydrogen sensor stakeholders to formulate the technical requirements for hydrogen safety sensors for automotive and stationary applications (**Scheme 2**).<sup>39</sup>

In a large and cross-disciplinary effort to reach the set goals, a large number of hydrogen sensor materials have been developed and investigated, with Pd being one of the most promising ones, thanks to a number of intrinsic properties that I will discuss in detail in **Chapter 2**. In brief, the key property that makes Pd so attractive is its ability to dissociate and absorb hydrogen. However, despite its potential, Pd also has some inherent limitations, such as relatively slow hydrogen diffusion, poisoning/deactivation by CO or sulfuric compounds, and hysteresis in the hydride phase. Translated to the sensor application, the slow hydrogen diffusion leads to slow sensor response/recovery. Furthermore, sensor poisoning/deactivation leads to poor sensor lifetime and even failure. To this end, CO is particularly problematic because it is ubiquitous with 0.2 ppm concentration in the atmosphere or even higher in urban

areas<sup>40</sup> and small amounts of CO are sufficient to deactivate Pd-based sensors.<sup>33,38</sup> Finally, the hysteresis effect causes ambiguous sensor readout, and thus, low sensor accuracy. The aim of Pd-based hydrogen sensor development is to resolve these issues.

The hysteresis-issue is somewhat less challenging than the response/recovery time and poisoning resistance issues, as it has been demonstrated that alloying Pd with coinage metals like Au, Cu, Ag or Ni is an efficient strategy to suppress hysteresis via lattice pre-straining/pre-compression<sup>41-45</sup> and it has already been adapted to hysteresis-free Pd-based hydrogen sensors.<sup>46,47</sup>

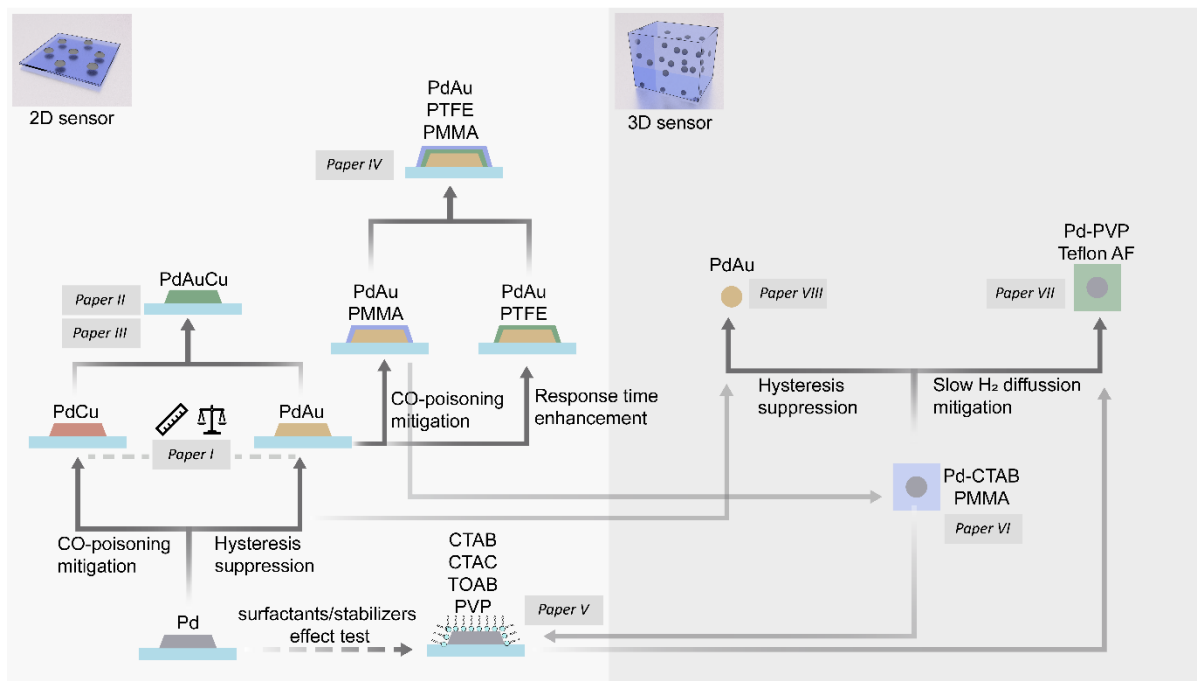
When it comes to sensor response/recovery, it is commonly identified as one of the most challenging US DOE targets and it has therefore been subject to significant research efforts over the last 20 years. They efforts were pioneered by a Pd nanowire hydrogen sensor reported in 2001, which attained a response time in the millisecond regime at the low explosion limit (LEL = 4 vol.%) of hydrogen gas in air at room temperature.<sup>48,49</sup> Prior to the nanowire sensor, hydrogen sensors had response times in the minutes regime, which is insufficient for safety applications. After the breakthrough in response time, it took almost two decades to reach the next milestone of response/recovery times of few seconds for hydrogen concentrations below LEL and for measurements at room temperature. Some examples of these recently developed ultrafast sensors are a porous Pd nanoparticle-coated CPPy polymer, which exhibits a 4.5 s response time at extremely low 20 ppm H<sub>2</sub><sup>50</sup> and a Pd/Au thin film on pSiC, which claims 2.3 s at 40 ppm H<sub>2</sub>.<sup>51</sup> This progress has mainly been driven by miniaturization and complex nanoarchitectures, which today can be made thanks to the rapid development of nanofabrication techniques. However, none has explicitly investigated nor developed a hydrogen sensor with fast response/recovery time (< 1s) at the designated dynamic range (0.1 vol.% = 1000 ppm) at room temperature, as required by the US DOE.

Finally, the issue with long term stability in poisoning conditions is a significant challenge, which has only very recently started to be addressed by the community, mainly using polymer layers as molecular filters. The core concept is that certain polymer materials are microporous enough to pass H<sub>2</sub>, while blocking larger molecules. This approach is not entirely new in gas sensor technology where polymer filters have been implemented in the gas inlet of gas sensor devices.<sup>52</sup> While effective from a filtering perspective, the problem with polymer layers is that they significantly hamper the gas transport to the active sensor surface, and thus, dramatically increase response and recovery times. Therefore, in my thesis I have developed a different approach, where the polymer is applied directly onto or even mixed with the transducer material.

In summary, there has been remarkable progress in the development of hydrogen sensors during recent years with respect to improving both response/recovery time and resistance to poisoning/deactivating environments. However, the progress has been made independently for the two aspects. In other words, sensors developed for fast response/recovery time have not been characterized with respect to their poisoning resistance, and vice versa. Furthermore, hydrogen sensors with reasonable poisoning resistance exhibit very long response/recovery times.<sup>53,54</sup> This is unfortunate because in the real application both performance parameters are equally crucial and not to be compromised. Nevertheless, to date, such hydrogen sensors do not exist. One of the main goals of this thesis to overcome this current limitation, i.e., to

develop a hydrogen sensor that is both ultrafast and deactivation/poisoning resistant for long periods of time.

## 2. This Thesis: The Strategy and the Outline



*Scheme 3: Mind map of my thesis. The work is divided into two different types of hydrogen sensor architectures, which are made from 2D- and 3D- Pd nanoplasmonic-polymer hybrid nanomaterials. My general strategy has been to address a specific weakness of a sensor at a certain stage by systematically introducing a new material component, e.g. a different alloyant, polymer matrix, or surfactant/stabilizer. A second strategy I employed, was to rationally design and develop the 3D sensors based on insights gained from the nanofabricated 2D sensors, which are more well-established and fundamentally understood. The mind map can be used to identify specific development steps made, how they came about, and in which of the appended papers they are reported.*

This thesis is focused on the development of Pd-based nanoplasmonic-polymer hybrid material hydrogen sensors and my work can be divided into two tracks, defined by the nature of the nanoparticle-polymer architecture used. The first track is the *2D sensor track* and the second track is the *3D sensor track*. The nomenclature is inspired by the dimensionality of the used nanocomposite material that constitutes the sensor transducer. A 2D sensor is comprised of Pd (alloy) nanoparticles nanofabricated as a 2D array onto a flat transparent substrate using hole mask colloidal lithography<sup>55</sup>, explained in detail in **Chapter 5**. Polymers are then applied as thin films onto the surface with the nanoparticles, to achieve a quasi-2D nanocomposite. A 3D sensor is instead, comprised of a 3D nanocomposite where colloidal Pd nanoparticles are embedded in the polymer matrix via bulk-processing techniques and then shaped into a sensor transducer via 3D printing or melt-pressing of the nanocomposite. The 2D sensor concept used in this thesis builds on earlier work from the Langhammer group,<sup>56,57</sup> whereas the 3D concept was entirely new and untested. I developed the 3D sensor from scratch together with my collaborators Alicja Stolás, Dr. Sarah Lerch and Dr. Robson da Silva in the group of Prof. Kasper Moth-Poulsen (responsible for colloidal synthesis of nanoparticles) and

Ida Östergren and Dr. Amir Pourrahimi in the group of Prof. Christian Müller (responsible for the polymer composite compounding and 3D printing). Below, I will summarize the key achievements of my work and how it is reported in the papers and manuscripts that constitute to this thesis (also see **Scheme 3**).

**Paper I** laid the foundation for the 2D Pd-alloy based nanoplasmonic hydrogen sensor design. This paper discusses the correlation between the amount of absorbed hydrogen by PdAu and PdCu alloy nanoparticles and the optical plasmonic response. We learnt that in the alloys, the amount of hydrogen absorbed is proportional to the amount of Pd in the system, and the sensitivity of the sensor to hydrogen, i.e., the magnitude of optical signal per amount of hydrogen absorbed, is dictated by the spectral position of the localized surface plasmon resonance of the nanoparticles in the non-hydrogenated state. These design rules served as a basis for further sensor development.

The introduction of Cu as an alloyant for Pd nanoparticles was motivated by the reported ability of Cu to reduce CO poisoning effects on Pd surfaces. Unfortunately, as we found, adding Cu to the alloy also reduces sensor sensitivity. Therefore, I attempted to combine the best of two worlds by making a 2D ternary PdAuCu alloy, where the Au is responsible for high sensitivity and small amounts of Cu for CO poisoning resistance. This concept indeed yielded a fast, hysteresis-free, highly sensitive and CO-poisoning resistant hydrogen sensor reported in **Paper II**. In **Paper III**, I also executed a systematic screening of the alloyant stoichiometry in the PdAuCu system to obtain the best possible performance. Furthermore, I implemented a more realistic and harsh protocol for the CO poisoning resistance testing.

In parallel to the Cu alloying strategy, I also investigated the use of thin polymer coating layers to achieve CO-poisoning resistance of the 2D sensors. Two structurally and chemically different polymers were examined, namely Poly(methyl methacrylate) (PMMA) and Polytetrafluoroethylene (PTFE). PMMA turned out to be superior to PTFE in terms of the CO blocking function. However, we also found that PTFE reduces the hydrogen (de)absorption apparent activation energy to a larger extent than PMMA and thus accelerated sensor response time to a larger degree than PMMA. Therefore, we developed a tandem PTFE-PMMA thin film protection layer to again combine the poisoning protection offered by PMMA and the response acceleration provided by PTFE. These results are reported in **Paper IV**.

Turning to the 3D sensor track, the 3D sensor development began with combining colloidal Pd nanocubes with a PMMA matrix, as reported in **Paper VI**. PMMA was rationally chosen based on its superior CO blocking capability identified on the 2D sensors in **Paper IV**. Extensive characterization of the developed nanocomposite material as some of the key results revealed that hydrogen response/recovery time is limited by H<sub>2</sub> diffusion through the PMMA matrix.

In **Paper VII** we investigated the use of the amorphous fluorinated polymer Teflon AF 1600 as the matrix for 3D sensors, since it is known to have two orders of magnitude higher H<sub>2</sub> diffusivity compared to PMMA. Using Teflon AF 1600, we indeed succeeded to reduce the response time of bulk-processed 3D printed hydrogen sensors down to the level of a few seconds. Moreover, we used Polyvinylpyrrolidone (PVP) as the colloidal Pd nanoparticle stabilizer during their synthesis instead of Cetrimonium bromide (CTAB), which we had used for the Pd-PMMA nanocomposite.

This exchange of ligand was motivated by a separate preceding study in **Paper V**, where we specifically investigated the impact of surfactants/stabilizers used in the colloidal synthesis of Pd nanoparticles on the hydrogen sorption kinetics of Pd, using the 2D sensor platform as the model. Specifically, we studied the four most common stabilizers/surfactants used: Cetrimonium bromide (CTAB), Cetrimonium chloride (CTAC), Tetraoctylammonium bromide (TOAB), and Polyvinylpyrrolidone (PVP). As the key result, we found that CTAB, CTAC, and TOAB decelerate hydrogen sorption kinetics, whereas the sorption kinetics is accelerated by PVP.

Next, focusing on the colloidal nanoparticles used in the 3D sensors, we applied neat Pd nanocubes in **Paper VI** and **Paper VII**. This means that the corresponding sensors exhibit hysteresis, which, as mentioned above, is detrimental for sensor accuracy. Therefore, we also developed a colloidal synthesis route for the synthesis of colloidal PdAu alloy nanoparticles in **Paper VIII**. I successfully applied the colloidal nanoparticle for optical hydrogen detection and together with Energy Dispersive X-Ray Spectroscopy (EDX) characterization, was able to confirm homogeneous alloy formation based on hydrogen sorption isotherm measurements, which were hysteresis-free for Au concentrations of 40 at.%.

Finally, I summarized and discussed the state-of-the art of Pd-based hydrogen safety sensors and summarized the key learnings from **Paper I - VIII** in the Perspectives **Paper IX**.

Now turning to the outline of the rest of this thesis, the basis of plasmonic hydrogen sensing, Pd hydride formation and Pd plasmonics, are discussed in-depth in **Chapter 2** and **Chapter 3**, respectively. Gas transport through polymer materials is described in **Chapter 4**. A detailed discussion of hybrid nanomaterial fabrication is presented in **Chapter 5**. The used material characterization techniques and hydrogen sensing test setups are described in **Chapter 6** and **Chapter 7**, respectively. Lastly, the conclusion and outlook are presented in **Chapter 8**.

# Chapter 2 - Palladium-Hydrogen Interactions

Palladium (Pd) was discovered accidentally in 1803 by English chemist William Hyde Wollaston just after the asteroid Pallas was found in 1802, from which the name “palladium” name was inspired.<sup>58</sup> From its discovery, it took six decades to realize that Pd absorbs large amounts of hydrogen (analog to a sponge that absorbs water!). This was work pioneered by Scottish chemist Thomas Graham (1866), almost one hundred years after Antoine Lavoisier discovered hydrogen gas in 1783.

Known as jewelry metal in daily life, Pd is also an important element used in many high-tech applications. For example, it is extensively used as catalyst in the chemical industry and emission control. To illustrate its importance, the 2010 Nobel prize in chemistry was even awarded for Pd as organic catalyst. Beyond that, Pd is found in electronic components, as well as in dental fillings.

In the hydrogen economy, Pd will be a vital element that likely will find application in virtually all aspects, from hydrogen production, to storage, and safety systems,<sup>59</sup> due the unique way hydrogen and Pd interact with each other.

## 1. Palladium-Hydrogen Interactions and Hydride Formation

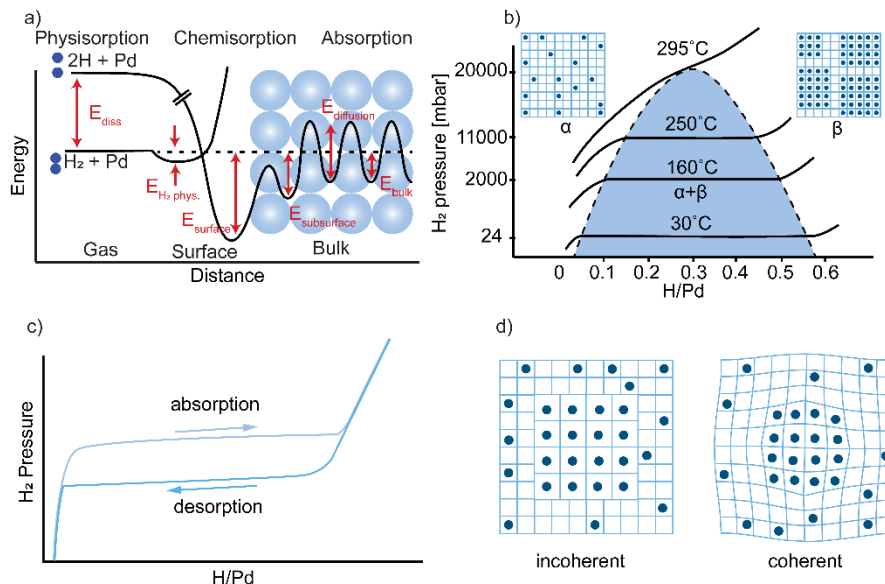


Figure 1: Pd-hydrogen interactions and hydride formation. (a) Energy landscape when  $H_2$  encounters Pd. On the Pd surface,  $H_2$  dissociates spontaneously into  $2H$  without activation barrier. Next, the dissociated H enters the Pd subsurface atomic layer by overcoming a first energy barrier. Subsequently, H must overcome energy barriers for each interstitial diffusion step on its way into the Pd bulk (adapted from ref.<sup>60</sup>). (b) Pressure-composition isotherms for the Pd – hydrogen system and the corresponding phase diagram. At low hydrogen pressure,

interstitial hydrogen (H) sparsely occupies the Pd lattice forming a solid solution, also known as  $\alpha$ -phase. At high hydrogen pressure, H clusters form the so-called  $\beta$ -phase, the hydride. Below the critical temperature  $T_c$ , a plateau region exists and denotes the co-existence of  $\alpha$ - and  $\beta$ -phase. Above the  $T_c$ , the plateau disappears and thus  $\alpha$  and  $\beta$ -phases are not distinguishable anymore and the phase-transformation is no longer first-order (the figure is adapted from ref.<sup>61</sup>). (c) Hysteresis: the absorption and desorption processes follow different paths in the pressure-composition isotherm. (d) Two mechanisms of  $\alpha \rightarrow \beta$  transformation: incoherent and coherent. In the incoherent transformation, the hydrogen-rich and -poor regions are separated with discontinuous lattice transition while in the coherent transformation the transition is continuous.

When the diatomic hydrogen ( $H_2$ ) molecule adsorbs on a Pd surface, it dissociates into two hydrogen (H) atoms instantaneously and essentially without activation barrier. As presented in **Figure 1(a)**, from the surface, these atoms diffuse first into subsurface interstitial sites and then into bulk interstitials in the Pd, forming Pd-hydride (Pd-H<sub>x</sub>). In Pd, the hydrogen absorption process occurs at room temperature at a high rate, which sets it apart from another hydride-forming metals, such as Ir, Rh, Ti or Mg, which require higher pressure or temperature to dissociate and absorb H into their lattice.<sup>62</sup>

When it comes to the rate-determining step of hydrogen absorption, various studies have shown different outcomes. Some studies argued that the rate-determining step is the hydrogen dissociation,<sup>63,64</sup> while others claimed it is the filling of subsurface sites<sup>60,63,65</sup> or bulk-diffusion.<sup>66-68</sup> It is worth noting that those studies were done for different film thickness/particle size, surface (facets), temperatures and hydrogen pressure, which might explain the different outcomes. In the case of nanoparticles, the absorption rate-determining factor is different than in bulk/film and a corresponding discussion is presented in the following subsection. For the desorption process, the rate-determining step argument is more uniform, i.e., that it is determined by hydrogen recombination on the Pd surface and  $H_2$  desorption.<sup>69,70</sup>

Focusing again on Pd, the energy landscape encountered by a  $H_2$  molecule depends on the chemical and physical properties of the Pd surface. For example,  $H_2$  dissociation rates have been shown to depend on the crystal structure of the surface<sup>71-73</sup> and the rate of diffusion depends on the hydrogen coverage on the surface.<sup>74</sup>

After dissociation of the  $H_2$  molecule on the Pd surface, the formed H-atoms will diffuse into the Pd bulk. At low hydrogen pressures, this leads to interstitial H-atoms being sparsely distributed in the Pd lattice, in a so-called solid solution termed  $\alpha$ -phase. In this regime, Sieverts' law applies, i.e. *the content of diluted hydrogen is proportional to square root of applied hydrogen (partial) pressure*.<sup>67</sup> Upon increasing the hydrogen pressure, at a critical pressure where the chemical potential of hydrogen in the gas phase and in the hydride are in equilibrium, attractive H-H interactions mediated by lattice strain induce the nucleation of the hydride or  $\beta$ -phase, as indicated by the onset of the so-called "plateau" in the isotherm. At room temperature, the maximum hydrogen solubility (expressed as H/Pd) in bulk Pd in the  $\alpha$ - and  $\beta$ -phase are 0.017 and 0.6, respectively.<sup>75</sup> For bulk Pd, the equilibrium plateau, across which the  $\alpha$ - and  $\beta$ -phase co-exist, occurs at pressures around 24 mbar at 30°C.<sup>61</sup>

From isotherms measured at different temperatures, one can derive the phase diagram for the Pd – H system (the phase boundary is the bell-shaped dashed-line in **Figure 1(b)**). As temperature is increased, the plateau elevates to higher pressure and the width of the two-phase coexistence region becomes narrower, until it vanishes at the critical temperature ( $T_c$ ).

At  $T \geq T_c$ ,  $\alpha$ - and  $\beta$ -phase are not distinguishable anymore and the phase transformation is no longer of first order. For bulk Pd,  $T_c$  is in the range of 290 °C.<sup>61,75</sup>

Hydrogen absorption into Pd has also structural implications. Pd has a face-centered-cubic (fcc) crystal structure with lattice constant 3.887 Å. In the  $\alpha$ -phase, the lattice constant increases up to 3.895 Å, before it more dramatically increases to 4.025 Å in the  $\beta$ -phase.<sup>75</sup> Thus, upon hydride formation, the lattice volume grows by approximately 10%. The volume expansion makes Pd prone to structural degradation (e.g., cracking and peeling) after cycle(s) of hydrogen (de)absorption, which is a problematic issue in applications like separation membranes and hydrogen sensors. It is also worth noting, however, that the volume expansion is not always a shortcoming for applications as, for instance, mechanical hydrogen sensors rely on this effect.<sup>76,77</sup>

The relation between pressure and the H-Pd ratio (H/Pd) depends on the direction of pressure increase/decrease due to the inherent hysteresis of the Pd-H system (**Figure 1(c)**). Specifically, experiments have shown that the plateau pressure of the absorption branch is always higher than the one of the desorption branch. The origin of hysteresis has been a point of scientific interest for long time. The earliest theory suggested that upon increasing hydrogen pressure, the formed  $\beta$ -phase creates lattice dislocations due to the volume difference compared to the  $\alpha$ -phase. Thus, the energy needed upon dislocation creation equals to energy gained by the phase transformation from  $\alpha \rightarrow \beta$  phase. In the desorption process, similar dislocation formation occurs in the  $\beta \rightarrow \alpha$  transformation but the required energy is less than for absorption, giving rise to hysteresis. This mechanism is known as *incoherent* phase transformation (**Figure 1(d)**).<sup>78,79</sup>

Upon multiple repetitions of the absorption-desorption cycle, the incoherent theory assumes that the created dislocations are annihilated entirely in each cycle, which is its main weakness because physically, complete annihilation of dislocations is not very likely. Therefore, an alternative model has been developed, which assumes a *coherent* phase transformation (**Figure 1(d)**). In this scenario, the  $\alpha$ - and  $\beta$ -phases are separated by a coherent phase boundary, rather than an incoherent one involving dislocations. This coherent phase transformation mechanism has recently been verified in several *in situ* studies of the hydride formation in single Pd nanocrystals, which revealed that hysteresis indeed is observed in a phase transformation that does not involve the formation and annihilation of dislocations.<sup>80-82</sup> These findings imply that hysteresis is an intrinsic thermodynamic process which does not involve the generation/annihilation of dislocations; at least not in nanoparticles.<sup>83,84</sup>

Hysteresis is a problem for a number of reasons when Pd is used for hydrogen sensor. For example, the two-phase coexistence plateau dominates the overall sensor readout and makes the readout large in narrow pressure range. Furthermore, hysteresis leads to ambiguous readout because the sensor response depends on the sensor history. In the appended **Paper IX**, I summarized strategies to overcome the plateau and hysteresis issues by (i) limiting sensor operation to the  $\alpha$ -phase, (ii) elevating the operation temperature above  $T_c$ , (iii) alloying Pd with other coinage metals, and (iv) reducing the size of the Pd transducer down to few nanometers. Using only the  $\alpha$ -phase, however, limits the sensor dynamic range up to the Pd plateau pressure. However, this issue can be overcome by increasing the operational temperature to elevate the plateau pressure.<sup>85</sup> Operating above  $T_c$  exploits the disappearance of the first order  $\alpha \leftrightarrow \beta$  transition above  $T_c$ , as discussed earlier in this subsection. Alloying,



which I have applied in this thesis, involves pre-straining/compression of the Pd lattice by larger/smaller coinage metal atoms and is discussed in more detail in the Pd alloy subsection below. The reducing size strategy will be discussed in the following subsection.

## 1.1. Consequences of Pd Nanostructuring to Hydrogen Sorption Kinetics and Isotherm

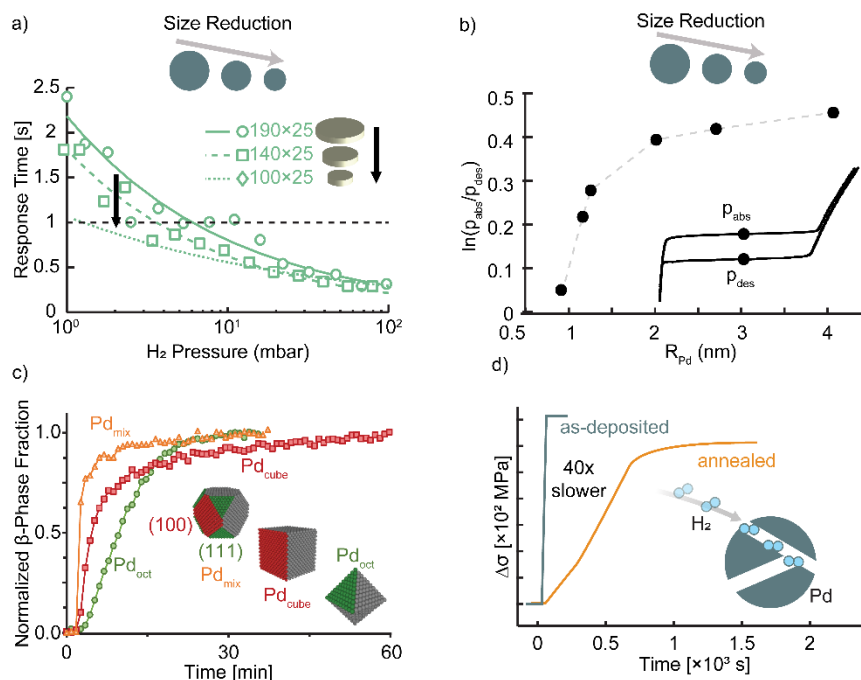


Figure 2: Consequence of nanostructuring for Pd-H interactions. (a) The response time of a PdAu nanoplasmonic hydrogen sensor is decreasing for all applied hydrogen pressures when nanoparticle size is reduced (adapted from ref.<sup>86</sup>(Paper IV)). (b) The hysteresis gap ( $\ln(p_{abs}/p_{des})$ ) is closing with decreasing the nanoparticle size. (adapted from ref.<sup>87</sup>). (c) Hydride ( $\beta$ -phase) formation rate of three differently shaped Pd nanoparticles: cube, octahedron, and truncated-cube. (adapted from ref.<sup>88</sup>). (d) Hydrogen absorption rate at a 6 mbar H<sub>2</sub> pressure step of and as-deposited and annealed Pd film showing the annealed one responding 40 times slower than the as-deposited one. The faster kinetics exhibited by the as-deposited film are due a higher density of grain boundaries, which enable rapid H-diffusion into the film, as depicted in the inset. (adapted from ref.<sup>89</sup>)

In this thesis, I used nanostructured Pd and therefore it is imperative to discuss nanosizing effects on the Pd hydride formation thermodynamics and kinetics. As a first effect, the hydrogenation kinetics in Pd nanoparticles are faster than in the bulk because of the larger surface to volume ratio (SVR), which provides more hydrogen dissociation sites per unit Pd volume and because the small size of nanoparticles shortens the hydrogen diffusion path length (**Figure 2(a)**). Hence, hydrogen absorption and desorption times fall exponentially with decreasing Pd nanoparticle radius.<sup>90</sup>

Pd nanoparticles also exhibit notably different pressure-composition isotherm profiles than Pd bulk. Specifically, the plateau region is typically more slanted in nanoparticle ensembles and the hysteresis gap is narrower.<sup>91–93</sup> The slanted plateau is a consequence of nanoparticle size distribution because it was not observed in single particle Pd.<sup>81,82</sup> The narrower hysteresis gap is the consequence of small nanoparticle ability to relieve hydride volume expansion stress and hysteresis vanishes when the nanoparticle size below  $\sim 5$  nm.<sup>92</sup> The hysteresis gap

dependence on the nanoparticle size is discussed thoroughly by Langhammer *et al* (**Figure 2(b)**).<sup>90</sup>

Recent in-situ spectroscopy and imaging experiments have also uncovered the role of Pd nanoparticle facets and vertices in the hydrogen sorption process (**Figure 2(c)**). Specifically, Johnson *et al.*'s, in their study of 20 nm-sized octahedral (6 vertices), cubic (8 vertices), and truncated cubic (24 vertices) Pd nanocrystals, showed that nanostructures with higher number of vertices tend to absorb hydrogen at faster rate, suggesting vertices as the hydride nucleation point,<sup>88</sup> in agreement with previous reports.<sup>94,95</sup> It is also worth mentioning that in a similar but earlier study, Li *et. al* argued that the faster absorption rate of octahedral nanoparticles with (111) facets compared to that of cubes with (100) facets is due to a lower hydrogen absorption energy barrier at the (111) facet.<sup>96</sup> For the desorption process, Johnson *et al.* observed a faster rate for nanoparticles with more (100) facets compared to (111) facets, suggesting that hydrogen recombination takes place at faster rate on the (100) surface, which is corroborated by their Density Functional Theory (DFT) calculations that show the recombination energy barrier for (100) to be lower than for (111).

Finally, also the presence of grain boundaries in polycrystalline Pd has been reported to result in a faster hydrogen absorption rate because grain boundaries exhibit enhanced hydrogen diffusion.<sup>89,97-101</sup> Delmelle *et al.* reported that a Pd thin film of average grain size 20 nm absorbed hydrogen 40 times faster than a film with 46 nm grain size, when measured for a 6 mbar hydrogen pressure step (**Figure 2(d)**).<sup>89</sup> However, the accelerating effect of grain boundaries on hydrogen absorption is only significant when the absolute hydrogen pressure is not too low because at very low hydrogen pressures, the low-coordination sites along the grain boundaries act as hydrogen traps, thereby slowing absorption kinetics in this regime.<sup>100,101</sup> This aspect is important to consider for when the hydrogen sensor is aimed at hydrogen detection in the ultralow concentration regime.

## 1.2. Pd Surface Modification Effects to Hydrogen Sorption Kinetics

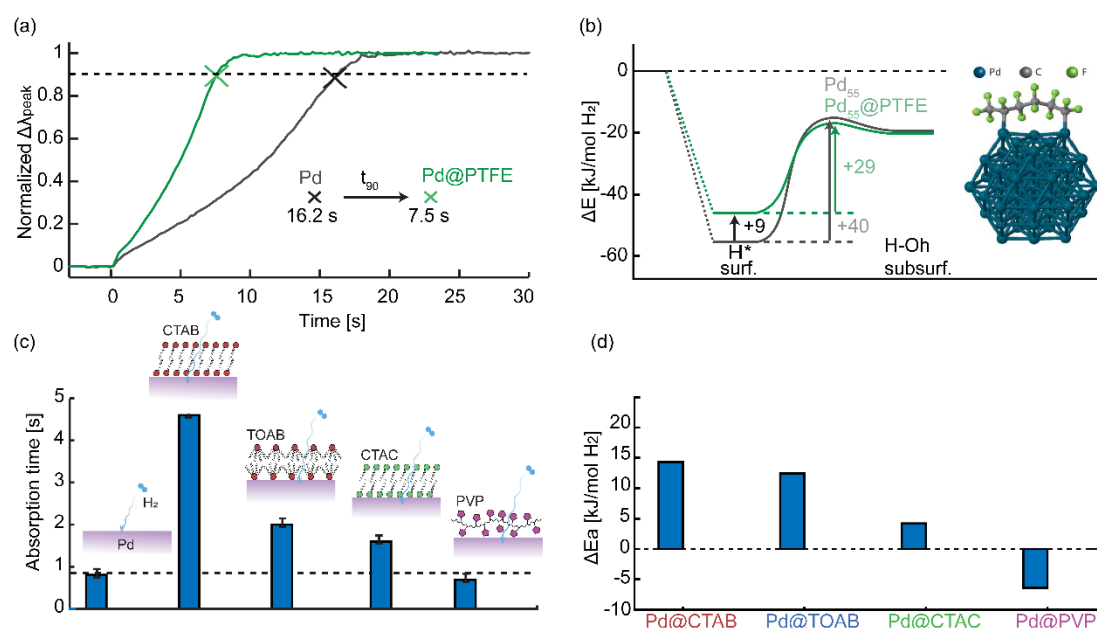


Figure 3: Polymer and surfactant/stabilizer effects on the hydrogen absorption rate in Pd. (a) Temporal response of neat Pd nanodisks and of Pd nanodisks coated with 50 nm PTFE to a 40 mbar  $H_2$  pressure step. (b) Hydrogen absorption energy barrier of neat Pd and PTFE-coated Pd calculated with density functional theory (DFT). The used PTFE-Pd nanoparticle model is depicted in the inset (**Paper IV**). (c) Hydrogen absorption time for Pd nanodisks coated with the capping agents/surfactants CTAB, TOAB, CTAC, and PVP, respectively. Note that, as illustrated, the cationic head of the surfactant is attracted to the Pd surface while the ligand is facing away. The surfactants also form a bilayer structure on the surface. (d) Apparent hydrogen absorption activation energy change induced by the respective capping agent. (**Paper V**).

Furthermore, surface modifications induced either by polymers and surfactant molecules used in colloidal synthesis or by metal-organic frameworks (MOFs), may alter the energy landscape. **Paper IV** shows that the presence of a thin PTFE layer on a Pd surface accelerates the hydrogen sorption rate (**Figure 3(a)**) by reducing the hydrogen (de)absorption activation energy (**Figure 3(b)**). A similar effect, however weaker, was also observed when the Pd was coated by PMMA (**Paper IV**) and PVP (**Paper V**), implying that the acceleration effect is a generic phenomenon with the magnitude of the effect controlled by the polymer type. On the other hand, the presence of cationic surfactants increases the hydrogen sorption time as I observed in **Paper V** (**Figure 3(c)**) and as also reported by others.<sup>102</sup> This deceleration effect is clearly reflected in an increase of the apparent activation energy ( $\Delta E_a$ ), as shown in **Figure 3(d)**. Mechanistically, the slowing effect is an interplay between two factors: (i) the surface density of the surfactant and (ii) the chemical interaction of the surfactant cationic head (Br or Cl) with the metal surface. The first factor is obviously shown by the dramatic hydrogen absorption time difference between CTAB and TOAB (**Figure 3(c)**). Since the apparent activation energy between those two surfactants is similar (**Figure 3(d)**), as one can expect due to the identical Br- head group, the faster absorption observed for TOAB can be attributed to its lower surface coverage due to the steric hindrance induced by its larger size. The second factor is observed when comparing the absorption time and  $\Delta E_a$  of CTAB vs CTAC. CTAB

and CTAC have similar surface coverage, but the absorption times are very different due to the different cationic head groups, which induce distinct  $\Delta E_a$ .

### 1.3. Implications of Carbon Monoxide (CO) Poisoning to Hydrogen Sorption Kinetics

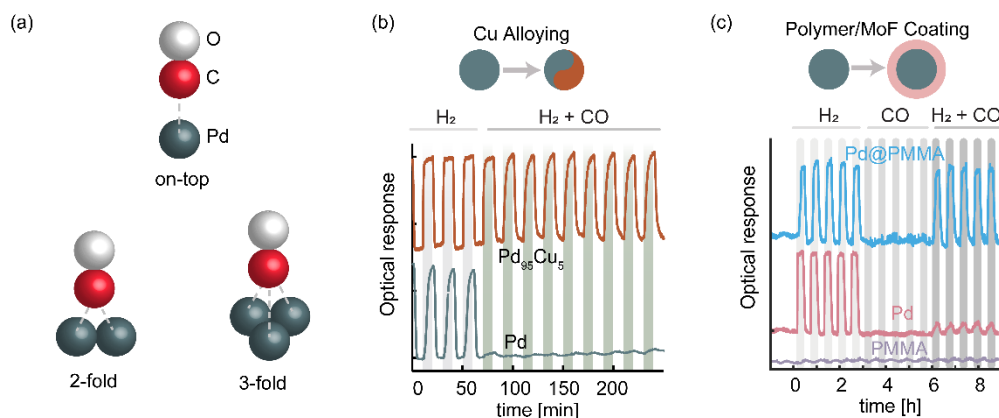


Figure 4: (a) Three different carbon monoxide adsorption geometries on Pd. Two strategies to mitigate CO poisoning on Pd: alloying with Cu (b) and polymer coating (c). (b) Temporal response of Pd and Pd<sub>95</sub>Cu<sub>5</sub> sensor to 4% H<sub>2</sub> and 4% H<sub>2</sub>+0.5% CO (in synthetic air background) at room temperature (**Paper II**). (c) Similar, temporal response of Pd and PMMA-encapsulated Pd to 10% H<sub>2</sub>, 0.5% CO, and mixture of 10% H<sub>2</sub> + 0.5% CO (**Paper VI**).

Generally, carbon monoxide (CO) adsorbs strongly on *d*-band metals like Pd with C atom coordinated to the surface.<sup>103–105</sup> On Pd, CO thereby blocks the hydrogen dissociation sites, which is detrimental for the hydrogen sensing application, especially at low temperature operation where essentially no thermal CO desorption takes place.<sup>106–109</sup> This blocking effect is known as CO-poisoning and its strength depends on the temperature and pressure, as well as the Pd surface facet. On the Pd surface, CO adsorption can take place in several locations: (i) on-top, (ii) in a two-atom bridge, and (iii) in a three-atom configuration (**Figure 4(a)**). Scenarios (ii) and (iii) are the favored ones for CO adsorption on Pd<sup>110–112</sup> and unfortunately, these sites are also the most stable sites for hydrogen.<sup>113,114</sup>

CO poisoning of Pd can be mitigated with several strategies: (i) Pd alloying with Cu, (ii) using selective polymer coatings, and (iii) combining Pd with metal-oxide (e.g. CeO<sub>2</sub>). Strategy (i) is discussed in more detail in **Paper II** and **III**, while strategy (ii) is discussed in **Paper IV** and **VI**.

In **Paper II**, we have demonstrated that as low as 5 at.% Cu is sufficient to promote resistance to CO poisoning (**Figure 4(b)**). The role of Cu to promote the CO poisoning resistance is supported by numerous studies of hydrogen separation membrane technology<sup>115</sup> and by first-principle calculations.<sup>116–118</sup> The calculations show that CO binds less strongly on PdCu than on pure Pd due to both an electronic ligand effect and a geometrical (ensemble) effect.<sup>119</sup> The ensemble effect in this case means that alloying reduces the number of three-atom sites to which CO strongly binds.<sup>120</sup>

Poly(methyl methacrylate) (PMMA) is a polymer known to selectively pass the small H<sub>2</sub> molecules, while blocking larger ones like CO.<sup>53,54</sup> We applied the coating strategy to both our 2D and 3D sensors to mitigate the CO-poisoning and the positive impact of a PMMA coating on my H<sub>2</sub> sensors is presented in **Figure 4(c)**.

Finally, though not applied in this thesis, metal oxides like CeO<sub>2</sub> have been demonstrated to alleviate CO poisoning in Pd catalysts. It is believed that the unique ability of Ceria to switch between multiple oxidation states allows it to store and release oxygen reversibly and thereby enable the oxidation of CO at low temperature.<sup>121,122</sup> It has also been demonstrated that CeO<sub>2</sub> is more preferential for CO adsorption than Pd.<sup>123</sup> This strategy may be worth to explore for hydrogen sensing applications in the future.

## 2. Palladium-Coinage Metal Alloys

As mentioned in the introduction, Pd possesses several major drawbacks, when used in sensor applications. One of the drawbacks is the hysteresis between hydrogen absorption and desorption, which can be mitigated by alloying. In addition, alloying improves the poisoning resistance of the sensor and accelerate the hydrogen sorption rate. In my work, three Pd alloys were of interest, namely the binary systems PdAu and PdCu, and the ternary system PdAuCu.

### 2.1. The Pd-Alloy Structure

Pd and Au form a solid solution upon alloying, which has an fcc crystal structure. Since the lattice parameter of Au is larger than the one of Pd ( $a_{\text{Au}} = 4.078 \text{ \AA}^{124}$ ,  $a_{\text{Pd}} = 3.887 \text{ \AA}^{75}$ ), the PdAu alloy lattice constant increases linearly according to Vegard's law with increasing Au content.<sup>125</sup> In contrast to the PdAu system, PdCu shows a decreasing lattice parameter as the Cu content is increased.<sup>126</sup> The reason behind this trend is that the lattice parameter of Cu is smaller than the one of Pd ( $a_{\text{Cu}} = 3.627 \text{ \AA}^{127}$ ).

PdCu alloys exist in fcc form across most of the phase diagram. At higher Cu contents, however, when the Pd concentration is in the range of 36-47at.-%, the alloy takes a bcc crystal structure. Due to the lattice compression induced by Cu, the hydrogen permeability of the fcc and bcc PdCu alloys is lower than in neat Pd.<sup>128</sup> When comparing the fcc and the bcc structures, however, higher permeability and diffusivity is found for the bcc structure, due to a less compact lattice.<sup>129-132</sup> The bcc PdCu, thus, may worth to investigate for fast hydrogen sensor application.

In two of the articles included in this thesis (**Paper II** and **Paper III**), we have developed a ternary PdAuCu alloy to combine the best features of the two binary PdAu and PdCu alloys for plasmonic hydrogen sensor applications. Ternary PdAuCu alloys have been studied mainly driven by the development of hydrogen separation membranes<sup>133-137</sup> and they have been produced using a number of techniques, namely arc melting,<sup>133</sup> pulsed laser deposition,<sup>135</sup> magnetron co-sputtering,<sup>134</sup> multilayer electroless plating,<sup>136</sup> and mechanical alloying.<sup>137</sup> For Cu-poor alloys, the PdAuCu system has an fcc crystal structure, dictated by

the fcc structure of PdAu. In binary PdCu on the other hand, it is known that also bcc crystal structure exists when the Cu content is in the range of 53-64 at.-%. Hence, Cu-rich PdAuCu ternary alloys exhibit a bcc structure. According to Guerreiro *et al.*,<sup>137</sup> the bcc structure is obtained when the alloy composition is  $30 \% \leq \text{Pd} \leq 46 \%$ ,  $45 \% \leq \text{Cu} \leq 63 \%$  and  $0 \% \leq \text{Au} \leq 17\%$ ; with  $\text{Pd}+\text{Cu}+\text{Au} = 100 \%$ . Finally, also the PdAuCu ternary alloy system lattice constant obeys Vegard's law, which means that it scales linearly with both the Cu and Au constituents.<sup>135</sup>

## 2.2. Pd-Alloy Hydrides

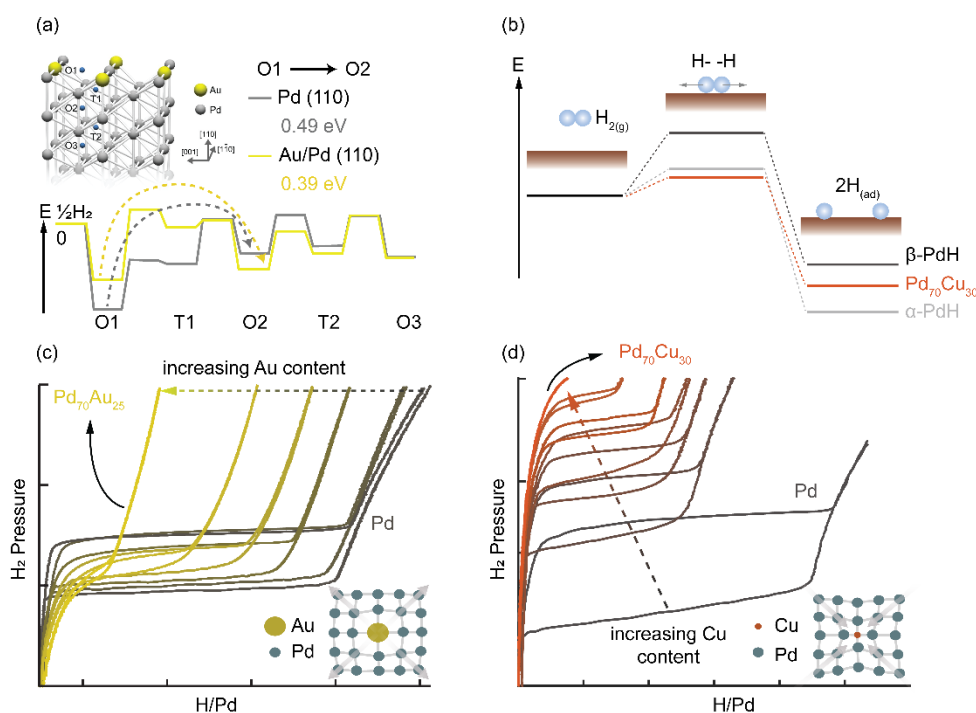


Figure 5: PdAu and PdCu alloy – hydrogen interaction and hydride formation. (a) The PdAu alloy - hydrogen absorption energy landscape calculated with density functional theory (DFT). Mixing Pd with Au lowers the hydrogen sub-surface absorption energy barrier (adapted from ref.<sup>138</sup>). (b) Hydrogen dissociation-adsorption activation energy on a Pd and PdCu surface. Lower dissociation-adsorption energy is observed experimentally for the PdCu alloy (adapted from ref.<sup>139</sup>). Pressure-composition isotherms of (c) PdAu and (d) PdCu alloy nanoparticles obtained at 30°C and in the 1-1000 mbar hydrogen pressure range. For PdAu, increasing Au content reduces hysteresis width. At 25 at.% Au, the isotherm is hysteresis-free. For PdCu, increasing Cu content reduces hysteresis width and elevates de/absorption plateau pressures simultaneously. At 30 at.% Cu, only the  $\alpha$ -phase exists even at 1 bar  $\text{H}_2$ . The pressure-composition isotherm evolution is the consequence of the lattice pre-straining (pre-compression) by the Au (Cu) alloyant, as depicted in the illustration.

Alloying alters the energy landscape for hydrogen absorption in Pd, as shown in several experimental and DFT studies of the PdAu and PdCu systems (Figure 5(a) and (b), respectively). As reported by Namba *et al.*, Au addition to Pd reduces the hydrogen energy barrier required to diffuse from the surface to subsurface sites.<sup>140</sup> This may explain the faster hydrogen absorption rates typically observed for PdAu-based hydrogen sensors.<sup>57,141</sup> Similarly, for PdCu, an experimental study by O'Brien *et al.* suggests that Pd<sub>70</sub>Cu<sub>30</sub> exhibits

significantly lower adsorption-dissociation and recombination-desorption activation energies compared to neat Pd, when tested in Ar background.<sup>139</sup> In contrast to PdAu, hydrogen (de)sorption kinetics of PdCu alloys have never been addressed.

In line with the different energy landscapes, hydrogen sorption isotherms for alloy systems are different from those of neat Pd and depend strongly on the alloyant concentration. For example, in the PdAu binary system, the hysteresis gap tends to be narrower (i.e., absorption plateau pressure drops while desorption plateau pressure raises) with increasing Au concentration (**Figure 5(c)**). This, in brief, is the consequence of the Au atomic radius being larger than that of Pd. Hence, it induces lattice expansion to the Pd host, which consequently reduces the energy barrier (pressure) to transform from the  $\alpha$  to the  $\beta$  phase. On the other hand, the PdCu binary system behaves differently compared to PdAu (**Figure 5(d)**). As the Cu content is increased, both absorption and desorption plateaus elevate to higher pressure and, at the same time, the hysteresis gap shrinks. In contrast to Au, the atomic radius of Cu is smaller than that of Pd and its presence contracts the Pd host lattice. At 30 at.-% Cu, only the  $\alpha$ -phase exists within the 1-1000 mbar hydrogen pressure range. These trends that I have obtained from my nanoparticle samples are consistent with previous studies of PdAu<sup>57,142</sup> and PdCu<sup>126,143,144</sup> thin film/bulk systems. For the ternary PdAuCu system, the corresponding isotherms contain contributions of both PdAu and PdCu, where the former introduces the hysteresis gap narrowing character and the latter is responsible for the plateaus elevation. The PdAuCu isotherms are discussed further in **Paper III**.

### 2.3. Alloy Stability: Surface Segregation

For alloy systems, the concentrations of the alloy constituents in the bulk and at the surface are not necessarily identical due to surface segregation effects. Hence, surface segregation may have significant implications for the initial steps of hydrogen ab/desorption and, thus, the function of such alloys in sensor applications. It is well known that Pd alloys with other coinage metals exhibit surface segregation, with the segregation depth profile being both monotonous and oscillatory. For example, using density functional theory (DFT) calculations, Løvvik has shown that PdCu alloys exhibit the latter type of depth profile, which may explain why in some cases the surface is rich in Pd while in other cases it is Cu-rich.<sup>145</sup> Other calculations predict that, in vacuum, Au has a higher tendency to segregate to the surface than Cu.<sup>145,146</sup>

Mechanistically, there are multiple factors that may induce surface segregation, for instance geometrical effects (i.e. atomic radius of the constituents) and electronic effects.<sup>145,146</sup> Accordingly, DFT calculations on Pd alloys by Løvvik show that alloyant atoms of larger diameter than that of Pd have a strong tendency to migrate to surfaces. In the same report, Løvvik also concludes that alloyants of lower surface energy than Pd are inclined to segregate to the surface.

Furthermore, external conditions, such as temperature and certain gases, have an impact on surface segregation. For example, surface segregation less likely occurs at high temperature due to entropic reasons, and since gases adsorb more strongly on certain metals than others, the gas environment will have a higher affinity to a specific constituent than to others, thereby

making it migrate to the alloy surface.<sup>145,146</sup> In hydrogen rich atmospheres, as relevant in this thesis, the surface tends to be Pd rich due to the high affinity of Pd to hydrogen.<sup>131,146,147</sup> Mezey *et al.*'s theoretical calculations and experimental observations indicate that even at very low concentration, O<sub>2</sub> drastically promotes surface segregation in PdAu and PdCu alloys. Pd tends to migrate to the surface in the PdAu alloy but in the PdCu, it is Cu which has that tendency.<sup>148</sup> Similarly, in the presence of O<sub>2</sub> and H<sub>2</sub>S, Cu tends to surface segregate in ternary PdAuCu systems.<sup>137</sup> Interestingly, CO adsorption can also induce segregation of Pd to the surface of PdAg, PdCu, and PdAu alloys since CO adsorbs strongly on Pd.<sup>115,146,149</sup> Moreover, the presence of defects/vacancies is known to accelerate Pd surface segregation by CO in PdAu.<sup>149</sup> Finally, the amount of surface segregation in PdAu systems is also dependent on the nanoparticle size, where smaller nanoparticles tend to have lower surface Pd concentration due to the limited Pd available in the nanoparticle bulk.<sup>150</sup>

In summary, the presence of surface segregation effects is very relevant to consider for my work since the Pd alloy sensors I have developed are exposed to considerably high concentrations of CO and O<sub>2</sub>. For further development of the alloy hydrogen sensor, the segregation aspect should be investigated to investigate the sensor stability.





# Chapter 3 - Nanoplasmonic Sensing

In the previous chapter, I have discussed the unique capacity of Pd to spontaneously absorb hydrogen and form a hydride. This process leads to a change of observable and measurable physical quantities in Pd, which are the basis of the Pd-based hydrogen sensors I have developed. For example, the hydrogenation of Pd induces changes in the electronic properties (e.g. conductivity), mechanical properties (e.g. lattice constant and hardness), acoustical properties (e.g. lattice resonances), and optical properties (e.g. transmittance, scattering, reflectivity). Since my work was focused on developing optical hydrogen sensors, this chapter discusses the optical properties of Pd and its hydride, with specific focus on the localized surface plasmon resonance (LSPR) effect that is excited when Pd nanoparticles interact with light, which is the core principle of the sensors I have developed.

## 1. Palladium-Hydride Optical Properties

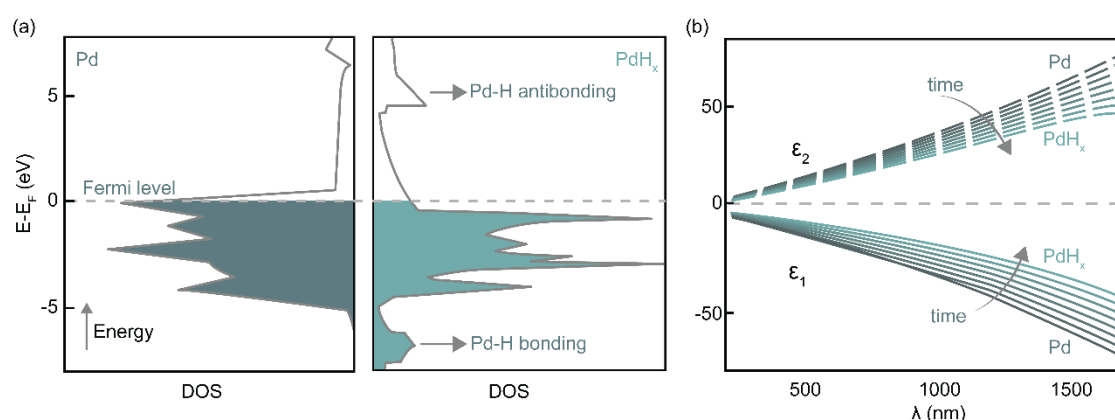


Figure 6: Pd and Pd-hydride electronic (a) and optical (b) properties. (a) The density of states (DOS) of pure Pd is characterized by the partially filled *d*-band, as denoted by the Fermi level. In the Pd-hydride, hydrogen atoms add more electrons to the system, thereby filling up the *d*-band. The Pd-H bonding and antibonding states are visible in the valence and conduction bands, respectively (adapted from ref.<sup>151</sup>). (b) Dielectric function evolution during Pd-hydride formation. The real ( $\epsilon_1$ ) and imaginary ( $\epsilon_2$ ) part of the dielectric function are represented by the solid and dashed-lines, respectively (adapted from ref.<sup>152</sup>).

Hydrogen sensing using Pd is possible thanks to the different properties of pure Pd and Pd with hydrogen occupying interstitial lattice sites. The differences can be traced back to the electronic structure since in the electronic density of states, the interstitial hydrogen atoms add electrons to the partially filled Pd *d*-band (**Figure 6(a)**). This partially filled *d*-band, as I will explain later, is also the reason why Pd does not have an equally strong plasmonic character compared to Au or Ag since in Pd, the absorbed light is partially used to excite electrons close to the Fermi level, instead of exciting the plasmon resonance.

From an optical property perspective, the electronic structure difference between the neat and hydrogenated Pd gives rise to an optical contrast. This optical contrast becomes apparent in the dielectric function evolution during the hydrogen absorption (**Figure 6(b)**).<sup>153,154</sup> The real

part ( $\epsilon_1$ ) describes how “loosely” the valence electrons of a material are bound and thus “lag” in an oscillation induced by an oscillation external field, such as light. The real part, therefore, carries information about the material’s metallic character. In metals, the real part is negative while in dielectrics/insulators, it is positive. In the case of Pd, the real part becomes more positive with more hydrogen being absorbed, implying a “less metallic” character of the Pd-hydride. The imaginary part ( $\epsilon_2$ ) determines how much light is being absorbed, transmitted, or scattered by the material. In the Pd case, the imaginary part noticeably decreases when the hydride is formed. This means that Pd-hydride absorbs less light than neat Pd. The distinct change of the imaginary part upon hydrogen sorption, therefore, is the basis for Pd-based optical hydrogen sensors. This optical contrast has been utilized in numerous optical hydrogen sensor platforms: measuring hydrogen-induced thin film optical transmittance,<sup>47,155</sup> reflectance<sup>156</sup> and interference (for eye-readable sensors)<sup>157</sup> or changes in surface plasmon resonance (SPR) of thin films<sup>158</sup> or in localized surface plasmon resonance (LSPR) of nanoparticles.<sup>159,160</sup>

## 2. Localized Surface Plasmon Resonance (LSPR)

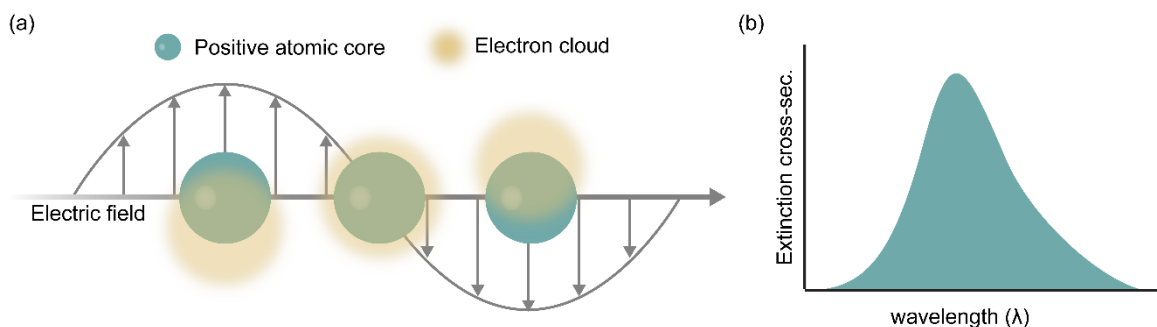


Figure 7: Schematic depiction of the localized surface plasmon resonance (LSPR) of a metallic nanoparticle. (a) At the resonance condition, the nanoparticle’s free electrons are driven by the electromagnetic field of an incoming plane wave at visible frequencies. (b) In the far field, the resonance appears as a distinct peak in the extinction spectrum. Note the width of the peak, which signifies the plasmon oscillation energy loss.

Localized surface plasmon resonance (LSPR) is a collective electron oscillation of metallic nanoparticles driven by an electromagnetic wave, i.e., light (**Figure 7(a)**). This strong nanoparticle - light interaction can be explained in the so-called quasi-static approximation, where the nanoparticle size is assumed to be much smaller than the wavelength of the incoming light ( $d \ll \lambda$ ). The interaction leads to light absorption ( $\sigma_{abs}$ ) and scattering ( $\sigma_{sca}$ ), which in sum is called extinction ( $\sigma_{ext}$ ) according to the optical theorem. For the special case of a sphere, they can be expressed analytically in terms of cross-sections ( $\sigma$ ) as follows:<sup>161</sup>

$$\sigma_{ext} = \frac{18\pi\epsilon_m^{3/2}V}{\lambda} \frac{\epsilon_2(\lambda)}{[\epsilon_1(\lambda) + 2\epsilon_m]^2 + \epsilon_2(\lambda)^2} \quad eq. 1$$

$$\sigma_{sca} = \frac{32\pi^4\epsilon_m^2V^2}{\lambda^4} \frac{(\epsilon_1 - \epsilon_m)^2 + \epsilon_2(\lambda)^2}{[\epsilon_1(\lambda) + 2\epsilon_m]^2 + \epsilon_2(\lambda)^2} \quad eq. 2$$

$$\sigma_{abs} = \sigma_{ext} - \sigma_{sca} \quad eq. 3$$

where  $\lambda$  is the light wavelength and  $V$  is the nanoparticle volume.  $\epsilon_1$  and  $\epsilon_2$  denote real and imaginary parts of the nanoparticle dielectric function, respectively.  $\epsilon_m$  denotes the real part of the nanoparticle's surrounding medium dielectric function. A resonance condition occurs when the cross-section is maximal, which is achieved by minimizing the denominator, i.e., when  $\epsilon_1 = -2\epsilon_m$ . This resonance appears as a peak in the extinction or absorption spectrum in the far field, when measured using a UV-visible spectrophotometer (**Figure 7(b)**). In practice, the peak is not singular but rather broad and the width of the peak correlates with the plasmon damping, which in turn is dictated by the imaginary part of the dielectric function. A broader peak implies stronger plasmon damping, which means that the plasmon excitation is not as strong and has a shorter lifetime.

In the visible light spectral range, Au and Ag have a small dielectric function imaginary part ( $\epsilon_2$ ), which means that Au and Ag nanoparticles scatter light efficiently.<sup>162</sup> This is why they are widely used as plasmonic materials. Other metals, e.g. Pt, Pd, Cu, Al,<sup>163</sup> are less attractive since they have larger  $\epsilon_2$ , which dampens the plasmonic resonance via interband transitions (see **Figure 6(a)**).

From the **eq. 1**, **eq. 2**, and **eq. 3**, it is clear that the interaction between metal and light depends both on the nanoparticle itself (i.e., size, shape and the material) and on the surrounding medium. Furthermore, beyond the approximation above, nanoparticle-light interactions also depend on the nanoparticle shape and arrangement in an array via far-field interactions, as well as on near-field coupling effects between closely adjacent nanoparticles.<sup>164,165</sup>

### 3. LSPR-based Pd Hydrogen Sensors

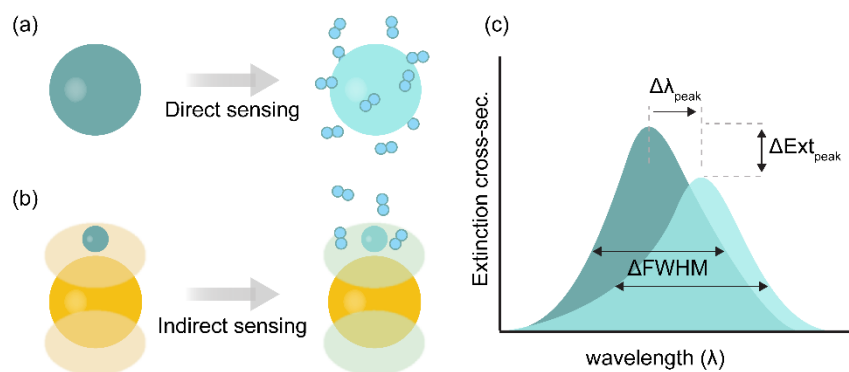


*Figure 8: Two conceptually different ways of LSPR-based  $H_2$  sensing using Pd: (a) direct sensing, where hydride formation leads to a change of the Pd nanoparticle LSPR condition and (b) indirect sensing, where the Pd nanoparticle is located closely adjacent to an inert plasmonic nanoparticle (e.g. Au or Ag) and within that particles' enhanced plasmonic near field. Thereby, the hydride formation in the Pd particle induces a refractive index change in the enhanced field region of the inert plasmonic nanoparticle "antenna", which via near-field coupling effects shifts the LSPR peak of the antenna, as depicted in (c). Peak position ( $\lambda_{peak}$ ), extinction ( $Ext_{peak}$ ), and full-width of half-maximum (FWHM) of the LSPR peak in the spectrum are then typically deployed as the sensor readout parameters, since they are proportional to the hydrogen concentration in the environment of the particle. The proportionality is discussed in **Paper I**.*

Since the interaction of a nanoparticle with light via LSPR excitation depends on the properties of both the nanoparticle and the surrounding medium, plasmonic nanoparticles can be used to “probe” nanoscale phenomena. Furthermore, the plasmon resonance is accompanied by a strong field enhancement ca. 10-20 nm away from the nanoparticle surface. These two phenomena constitute the principle of LSPR-based sensing.<sup>166,167</sup> In the specific case of H<sub>2</sub> detection using Pd in focus of my thesis, there are two ways to exploit the LSPR sensing principle: (i) *direct sensing* **Figure 8(a)** and (ii) *indirect sensing* as depicted in **Figure 8(b)**. Both mechanisms induce LSPR shifts upon hydrogen sorption in a Pd nanoparticle, as illustrated in **Figure 8(c)**. Technically, H<sub>2</sub> detection is carried out by tracking the change of the peak position ( $\lambda_{peak}$ ), peak extinction ( $Ext_{peak}$ ) or the full-width half-maximum ( $FWHM$ ) induced by hydrogen sorption in the Pd nanoparticle.<sup>168</sup>

In the *direct* sensing mode, the LSPR response of the hydride-forming nanoparticle itself, in my case Pd or a Pd alloy, constitutes the signal transducer. The first direct LSPR hydrogen sensing experiment was demonstrated by Langhammer *et al.* using a Pd nanodisk array and by tracking both LSPR peak position and extinction during hydrogen (un)loading.<sup>169</sup> From these two LSPR descriptors, a Pd-H isotherm was constructed. The isotherm correctly resolved the  $\alpha$ - and  $\beta$ - phase regions, the characteristic plateau and the hysteresis between ab- and desorption, indicating strong correlation between the absorbed hydrogen content and the optical descriptors. In **Paper I**, we experimentally confirmed this linear correlation by simultaneous monitoring of the LSPR response of arrays of neat Pd, PdAu and PdCu alloy nanoparticles and the absolute absorbed amount of hydrogen in the particles using a quartz crystal microbalance (QCM). Furthermore, for direct sensing, the geometry of the Pd nanostructure is an important aspect because it defines the LSPR spectral peak position, which, as we also discuss in **Paper I**, directly determines the sensor sensitivity. Specifically, we found that the more spectrally red-shifted (longer wavelengths) the Pd LSPR peak position is in the non-hydrogenated state, the larger the peak shift upon hydrogenation will be. For nanodisks, the LSPR peak position can be tuned by tailoring the diameter and the height. A longer wavelength LSPR peak can be achieved either by increasing the nanodisk diameter (**Figure 9(a)**) or by reducing the height (**Figure 9(b)**).<sup>170</sup>

In the *indirect* sensing mode, the Pd nanoparticle is positioned within the plasmonic near field of an inert plasmonic nanoparticle “antenna” (usually Au). Therefore, any change in the Pd particle is “detected” by the antenna via its near field. Mechanistically, this can be understood by the dependence of the plasmonic resonance on the surrounding medium refractive index, which can be derived from the Drude model:<sup>161</sup>

$$\lambda_{max} \propto n_m \quad \text{eq. 4}$$

where  $\lambda_{max}$  is the LSPR frequency and  $n_m$  denotes the refractive index of the surrounding medium. The equation implies that the LSPR peak shift is proportional to the refractive index. Based on this principle, plasmonic sensors for a wide area of applications have been developed, including biosensors,<sup>171–173</sup> gas sensors,<sup>174–176</sup> and spectroscopy.<sup>177,178</sup> When it comes to Pd nanoparticle-based hydrogen sensing in focus here, the indirect sensing scheme is most useful when the LSPR cross section of the use active sensor nanoparticles either is very small and/or shifted to the UV spectral range due to small size (diameter < 50 nm, ref.<sup>152</sup>). Examples of this approach are small Pd nanoparticles deposited onto SiO<sub>2</sub>-covered Au nanoparticle antennas,<sup>179</sup> where the SiO<sub>2</sub> spacer contributes to the enhancement of the plasmonic near field

of the Au antenna.<sup>180,181</sup> Another example is the placement of a Pd nanoparticle near the tip of a triangular Au nanoparticle<sup>182</sup> or in the gap of an Au nanoparticle dimer.<sup>183,184</sup> Up to five-fold increase of the hydrogen sensing response was observed by the dimer approach.<sup>184</sup> I employed indirect sensing in the **Paper VIII** to measure pressure-composition isotherms of colloiddally synthesized PdAu nanoparticles (average diameter ca. 50 nm).

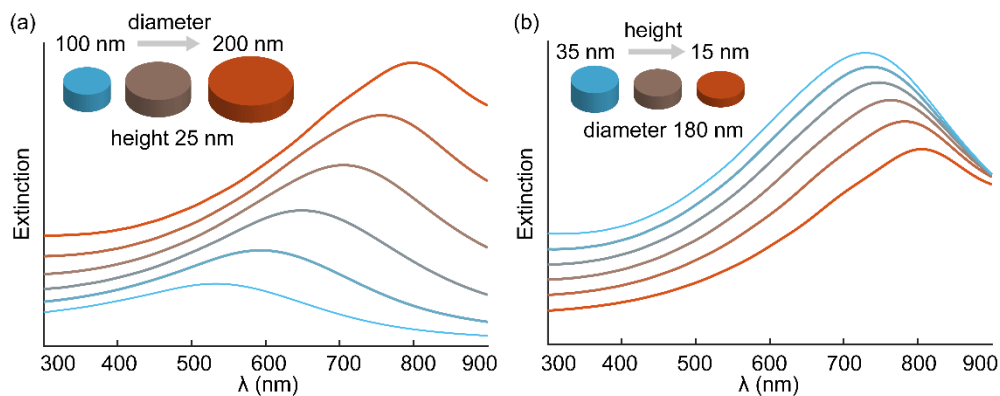


Figure 9: LSPR extinction spectra of a Pd nanodisk calculated by finite difference time domain (FDTD) numerical simulations for (a) disks with diameter ranging from 100 to 200 nm for constant height 25 nm. The extinction peak red-shifts with increasing diameter. (b) Same as (a) for a nanodisk with constant 180 nm diameter and height varying from 35 to 15 nm. Reducing the nanodisk thickness shifts the extinction peak towards longer wavelengths. Courtesy of C. Tiburski.



# Chapter 4 - Gas Transport in Polymers

The molecular sieving capability of polymers is a key reason for combining them with Pd nanoparticles to create a nanoparticle-polymer hybrid plasmonic hydrogen sensor. To this end, numerous polymers have been studied and developed for their molecular sieving function, mainly driven by gas purification and separation applications in the refinery and chemical industries.<sup>185</sup> In my project, polymers with high H<sub>2</sub> permeability and simultaneously high selectivity. In other words, the ideal polymer would pass H<sub>2</sub> only, while blocking any other molecules. While this in reality may sound almost like a dream scenario, in our case we can take advantage from the fact that H<sub>2</sub> is the smallest gas molecule, which means that it can easily penetrate materials that block larger molecules. In this respect, glassy polymers are particularly interesting, since they are known for their excellent molecular sieving capability.<sup>185,186</sup> In this chapter, I will therefore discuss: (i) the basic theory of gas transport through a polymer membrane, (ii) the implications of polymer microstructure, (iii) the permeability vs. selectivity issue, (iv) the implications of ultrathin polymer films for gas transport and (v) the H<sub>2</sub> transport in the Pd nanoparticles-embedded polymer.

## 1. Gas Transport Through Polymer Membranes: Solution-Diffusion Theory

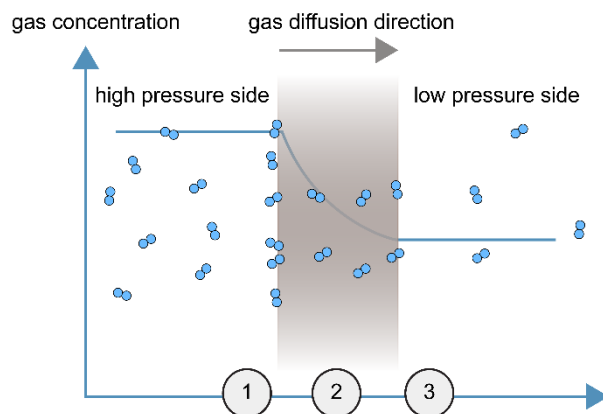


Figure 10: Illustration of gas flow through a polymer membrane from a high partial pressure to a low partial pressure chamber. The process begins with (1) gas sorption at the membrane's surface on the high partial pressure side, (2) diffusion through the membrane bulk leading to a gas concentration gradient across the membrane, and (3) gas desorption from the membrane's surface on the low pressure side.

To conceptually analyze the gas transport through a polymer membrane it can be broken down into the following individual and subsequent steps: (i) gas molecule sorption at the high partial pressure side, (ii) diffusion through the polymer bulk, and (iii) desorption at the lower pressure side, as depicted in **Figure 10**. In this picture the polymer's capability to transfer gas molecules from the high-pressure side to the low-pressure side is known as permeability ( $P$ ).  $P$  is the product of two factors: the solubility coefficient ( $S$ ) and the diffusivity coefficient ( $D$ ),



where  $S$  is a thermodynamic factor that portrays how many gas molecules dissolve in a polymer, and where  $D$  is a kinetic factor that describes the gas mobility across a polymer. This gas transport mechanism is also known as the *solution-diffusion mechanism*, which is applicable to both semi-crystalline and amorphous polymers.<sup>187</sup>

Semi-crystalline polymers consist of short-range highly-ordered (crystalline) domains joined by random coiled chains (**Figure 11(a)**).<sup>188</sup> Examples of popular semi-crystalline polymers are polylactic acid (PLA), polytetrafluoroethylene (PTFE), and polyethylene (PE).<sup>188</sup> Semi-crystalline polymer is often characterized by the so-called “degree of crystallinity”. The dense-packed crystalline domains are much less permeable to gas, thus gas occupy and diffuse only along the amorphous parts in between the crystallites. With that in hand, the higher the “degree of crystallinity” is the less impermeable the polymer is. In addition, permeability also depends on the arrangement/shape of the crystallites.<sup>189</sup>

Amorphous polymer entails a polymer whose molecule chains are disordered, thereby resembling boiled “spaghetti”, as depicted in **Figure 11(a)**. Optically, amorphous polymers are typically transparent, while semi-crystalline polymers are translucent and opaque.<sup>190</sup> Therefore, amorphous polymers are ubiquitous in everyday life, for example in acrylic glass or poly(methyl methacrylate) (PMMA) and polystyrene (PS)<sup>188</sup> and solution-diffusion theory can describe gas transport in amorphous polymers both in the glassy and in the rubbery regime.<sup>191,192</sup> The glassy and rubbery state of an amorphous polymer can be understood from the so-called glass transition perspective. Specifically, at relatively low temperature, amorphous polymer molecules are quite static, but when the temperature is increased beyond the glass transition temperature ( $T_g$ ), the molecules suddenly become very dynamic. As a consequence, an amorphous polymer in the glassy state is rigid, hard and brittle, while a polymer in the rubbery state is soft and elastic.<sup>193</sup> The term “glassy polymer” therefore often refers to polymers with relatively high  $T_g$ , while rubbery polymers have a low  $T_g$ . Hence, at room temperature, a polymer is categorized as glassy if  $T_g > 25$  °C and rubbery if  $T_g < 25$  °C.

## 1.1. Gas Transport from a Microscopic Point of View

### 1.1.1. Gas Diffusivity and Solubility

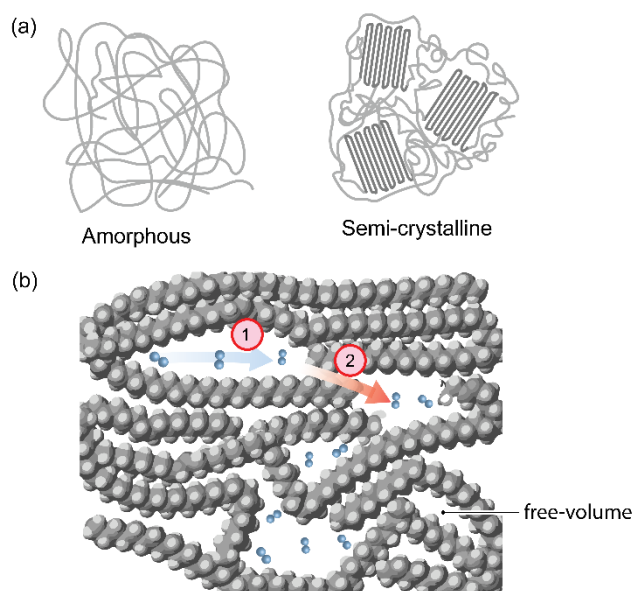


Figure 11: (a) Illustration of polymer chain arrangement in amorphous and semi-crystalline polymers. The amorphous polymer is characterized by randomly distributed polymer chains. The semi-crystalline polymer consists of high-order “crystalline” domains separated by amorphous regions.<sup>190</sup> (b) The microscopic mechanism of gas dissolution and diffusion in an amorphous polymer. The unoccupied space in between polymer electronic clouds is considered as free-volume. For gas dissolution, the gas molecules populate the free-volume. For the gas diffusion there are two mechanisms: (1) transfer through the free-volume and (2) “leak” transfer between free-volume regions.

A more sophisticated and atomistic way to describe gas transport through a polymer membrane is to assume that the gas molecule diffuses through spaces unoccupied by the polymer molecule and its “electron cloud”, as depicted in **Figure 11(b)**. This unoccupied space is known as *free-volume* and corresponds to interstitial space with sizes of few Å (this makes the nomenclature “micropores” a bit misleading but it nevertheless is the term used in the corresponding literature).<sup>185,194</sup> The free-volume network within the polymer resembles a nanoscopic labyrinth where not all micropores are interconnected. In a glassy polymer, these free-volume are not completely static, which allows “leaking” and thus for the permeant molecules to jump from one pore to another. Therefore, for a glassy polymer, diffusion along and jumping between micropores determines the polymer’s gas diffusion coefficient.<sup>195,196</sup> The correspondingly expected strong correlation of the diffusion coefficient with the fraction free volume (FFV) was clearly identified in Thran *et al.*’s extensive literature study of gas diffusion in glassy polymers, which concludes that high FFV polymers tend to have a higher diffusion coefficient.<sup>197</sup> Furthermore, a literature survey shows that the diffusion coefficient also depends on the properties of the gas itself, i.e. the molecular diameter and velocity.<sup>186,198</sup> Specifically, the gas diffusivity increases with decreasing molecule effective diameter.<sup>199,200</sup>

Another important aspect to consider about the gas transport is that a specific gas has different chemical affinity to different polymers. The degree of this affinity is manifested in the

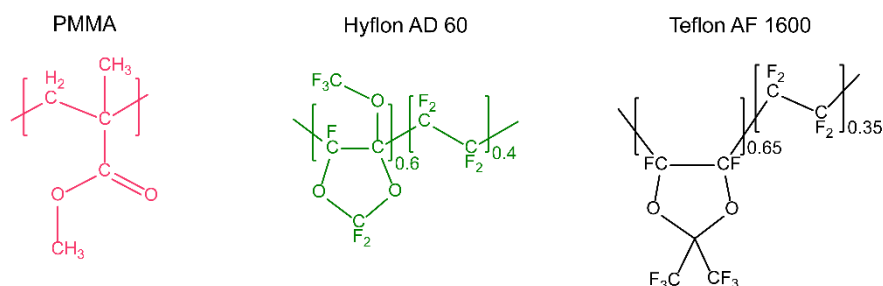
solubility coefficient  $S$ , where a higher  $S$  means a larger amount of gas being dissolved in the polymer. Microscopically, the gas molecules occupy the free-volume as depicted in **Figure 11(b)**.<sup>201,202</sup>

In summary, for glassy polymers like PMMA and Teflon AF used in this thesis, the gas permeability is dictated by  $D$ . Therefore, the gas permeability can be estimated based to the gas molecule size and the FFV of the polymer.

### 1.1.2. PMMA and Amorphous Fluorinated Polymers

Since we now have established that the free-volume plays a key role in the gas permeability of glassy polymers, it warrants a more detailed discussion with focus on the two polymer systems I have used in my thesis for bulk-processed 3D hydrogen sensors: (i) PMMA (**Paper VI**) and (ii) the amorphous fluorinated polymers (FP) Hyflon AD 60 and Teflon AF 1600 (**Paper VII**). Specifically, we employed PMMA in the first sensor generation and later, with the aim to dramatically improve the response/recovery times – we used the amorphous FPs since their hydrogen permeability and diffusivity are two orders of magnitude higher than for PMMA (**Table 1**). Experimentally, the free-volume of a specific polymer can be quantified using positron annihilation lifetime spectroscopy (PALS).<sup>195</sup> The topology or structure of the free-volume is usually investigated by modelling approaches, such as molecular dynamics (MD) simulations.<sup>196</sup>

The dramatic gas transport differences between PMMA and amorphous FPs can be explained by the respective microstructure. Focusing on the FPs, literature reports a remarkably high free-volume fraction for both Hyflon AD 60 and Teflon AF 1600 (**Table 1**). This can be understood when considering their molecular structure, which reveals bulky and hard-to-rotate dioxole-moiety branches along the polymer backbone (**Scheme 4**), and by the fact that interchain interactions in these systems are very weak.<sup>203</sup> This renders micropore volume for Teflon AF 1600 in the range of 270 – 630 Å<sup>3</sup> at room temperature, which implies micropore radii of 4 – 5 Å by assuming a circular cross-section.<sup>204</sup> In comparison, the reported micropore volume and radius for PMMA measured at similar conditions are 95 – 114 Å<sup>3</sup> and 2.8 – 3.0 Å, respectively,<sup>205</sup> which is significantly lower. Correspondingly, due to the larger micropore volume, it is indeed expected that gas diffusivity is significantly higher in Teflon AF 1600 compared to PMMA, in good agreement with the corresponding experimentally determined values (**Table 1**).



*Scheme 4 Monomer chemical structure of PMMA, Hyflon AD 60 and Teflon AF 1600.*

Polymer	$P$ (barrer) <sup>†</sup>	$D$ ( $\times 10^{-7}$ cm <sup>2</sup> /s) <sup>†</sup>	FFV
<b>MMA</b>	4.2	6.6	0.14 <sup>206</sup>
<b>Hyflon AD 60</b>	160	63.2	0.17 <sup>207</sup>
<b>Teflon AF 1600</b>	745	232.0	0.29 <sup>207</sup>

<sup>†</sup>data obtained by the group of Prof. M. Minelli at University of Bologna and presented in **Paper VII**.

Table 1 Hydrogen permeability,  $P$ , diffusivity,  $D$ , and fraction free volume, FFV, of PMMA, Hyflon AD 60, and Teflon AF 1600 at room temperature.

## 2. Permeability-Selectivity Trade-off

Permeability-selectivity (permselectivity for short) is expressed as the ratio between permeability of fast permeating gas A (in my case H<sub>2</sub>) and a slow-permeating gas B (in my case for example CO or NO<sub>2</sub>). Therefore, optimizing permselectivity is very important to create a selective, deactivation resistant and fast H<sub>2</sub> sensor. Unfortunately, however, in this respect there is always a trade-off between permselectivity and permeability. This trade-off is known as the “upper bound” introduced by Robeson in his studies of the correlations between permeability and permselectivity in various polymers.<sup>208</sup>

I experienced this upper bound dilemma in my work both for the bulk-processed Pd-PMMA (**Paper VI**) and Pd-FP systems (**Paper VII**). Specifically, PMMA showed an exceptional hydrogen selectivity and was able to efficiently protect the Pd nanoparticles from CO, but at the cost of low diffusivity in general, which also applies to H<sub>2</sub> and thus hampered the sensor response/recovery time significantly. In contrast, the Teflon AF 1600 and Hyflon AD 60 systems enhanced the H<sub>2</sub> response/recovery time by roughly two orders of magnitude but at the expense of lack of CO-poisoning protection.

## 3. Gas Transport through Polymer Thin Films

As mentioned earlier, H<sub>2</sub> must diffuse through the polymer as fast as possible to obtain a fast H<sub>2</sub> sensor. To achieve this, as an alternative to, or in combination with, selecting a high-diffusivity polymer, one can also decrease the characteristic diffusion time by reducing the polymer thickness and resort to thin films. To this end, solution-diffusion theory suggests that the characteristic diffusion time ( $\tau$ ) increases quadratically with increasing film thickness ( $l$ ):<sup>209</sup>

$$\tau = \frac{l^2}{6D} \quad \text{eq. 5.}$$

Consequently, decreasing the polymer thickness is advantageous for the characteristic diffusion time and thus it should provide a solution to achieve faster response to H<sub>2</sub>. Indeed, for polymer film thicknesses on the order of 50 nm, as I have used in **Paper IV** to coat nanofabricated hydrogen-sensitive nanoparticles, the diffusion times at room temperature for PMMA and PTFE calculated using eq. 5 are only 6.6  $\mu$ s and 5.2  $\mu$ s, respectively. This is far below the time constant for hydrogen ab/desorption from neat Pd and its alloys, which is on

the order of milliseconds.<sup>210</sup> Therefore, in this ultrathin film regime, the impact of H<sub>2</sub> diffusion through the polymer on sensor response time is essentially negligible. I also note that for the above calculation I assumed a thickness-independent diffusivity coefficient,  $D$ , which for PMMA ( $=6.7 \times 10^{-7}$  cm<sup>2</sup>/s) and PTFE ( $=8.0 \times 10^{-7}$  cm<sup>2</sup>/s) were obtained from refs.<sup>211,212</sup>

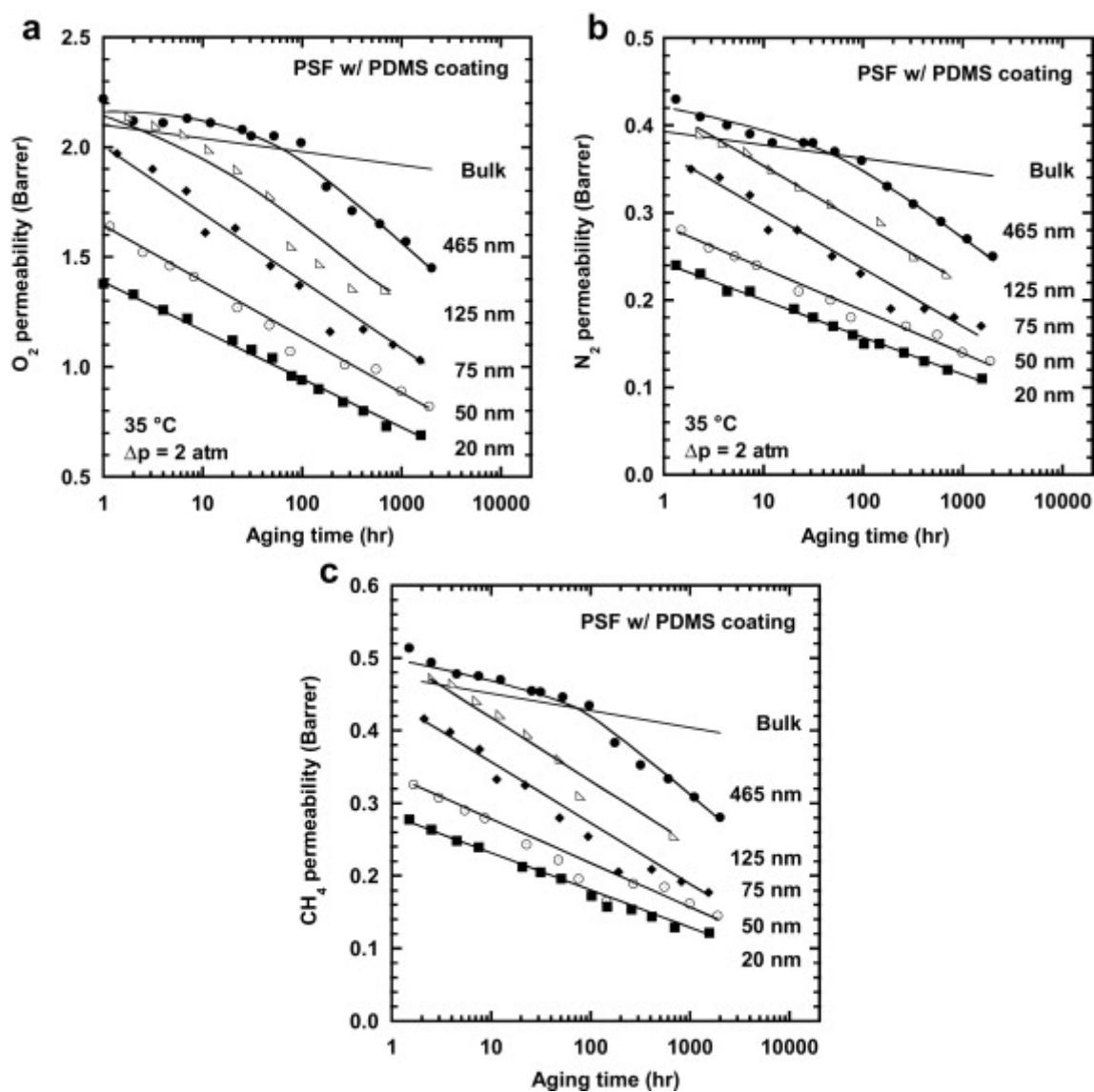


Figure 12 Thickness- and time-dependent permeabilities of O<sub>2</sub>, N<sub>2</sub>, and CH<sub>4</sub> in a polysulfone (PSF) polymer. Permeability tends to be lower in thinner films. Also, permeability is decreasing over time. Time zero is defined as the time when the polymer is cooled down to the glassy state after heating above the T<sub>g</sub>. A similar trend is observed for other glassy polymers, namely Matrimid® and poly(2,6-dimethyl-1,4-phenylene oxide) (PPO). Reprinted with permission from ref.<sup>213</sup>

However, it is not a priori clear, but equally relevant, what the implications of reducing the polymer thickness are for gas permselectivity. However, to the best of my knowledge neither H<sub>2</sub> permeability nor permselectivity studies of ultrathin PMMA nor PTFE films exist. However, there are some studies of the permeability/permselectivity of other glassy polymers, from which we can gain some insight in the question at hand. Specifically, the Paul group investigated the thickness dependence of the O<sub>2</sub> permeability/permselectivity for three different polymers commonly used in commercial gas separation membranes, namely polysulfone (PSF), poly(2,6-dimethyl-1,4-phenylene oxide) (PPO), and Matrimid® in the 60

$\mu\text{m}$  down to 20 nm thickness range.<sup>213–215</sup> They categorized the results into three groups: (i) the thick film regime for thickness  $> 10 \mu\text{m}$ , (ii) the thin film regime for  $400 \text{ nm} < \text{thickness} < 10 \mu\text{m}$ , and (iii) the ultrathin film regime for thickness  $< 400 \text{ nm}$ .<sup>213–215</sup> As the main result, they observed that permeability tends to decrease for decreasing film thickness and that, as expected, decreasing permeability is accompanied by increasing permselectivity (**Figure 12**). This trend is consistent across the three studied glassy polymers and across the tested gases  $\text{O}_2$ ,  $\text{N}_2$ , and  $\text{CH}_4$ . These trends can be explained by the fact that, in thin polymer films, the polymer chain length eventually becomes comparable to the film thickness, therefore forcing the chains to occupy the free space more efficiently. This more efficient free space occupation then leads to lower gas permeability<sup>214,215</sup>. Accordingly, these observations may explain that in **Paper IV**, a thin PMMA coating of ca. 50 nm still exhibits excellent  $\text{H}_2/\text{CO}$  selectivity. In addition, these studies also observed the physical aging of glassy polymers, meaning that the permeability (permselectivity) decreases (increases) over time. For gas sensing applications, this is an advantage because it means that the sensor selectivity will improve as it becomes older.

#### 4. $\text{H}_2$ Sorption Kinetics in Pd-nanoparticles:Polymer 3D Sensors

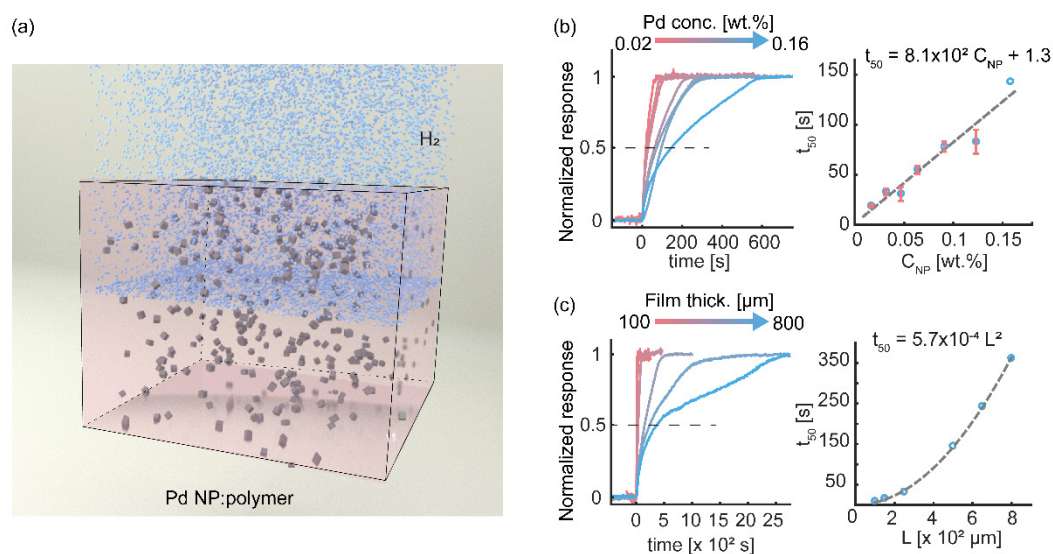


Figure 13: (a) Diffusion front approximation of  $\text{H}_2$  diffusion in a 3-dimensional Pd:PMMA hybrid material. Behind the “front”, Pd nanoparticles are fully hydrogenated. (b) Left: Temporal optical response of Pd:PMMA 3D sensors with different Pd concentrations. Right:  $t_{50}$  versus Pd concentration.  $t_{50}$  is defined as the required time to reach 50% of the sensor’s full response at a new pressure. (c) Left: temporal response of different Pd:PMMA film thicknesses at constant Pd loading and right:  $t_{50}$  versus the film thickness. (**Paper VI**).

The  $\text{H}_2$  sorption process in my Pd:polymer 3D sensors consists of two stages: (i) diffusion through the polymer matrix and (ii) sorption by the Pd nanoparticles hosted by the matrix. In the case of a PMMA matrix, stage (i) is much slower than stage (ii), which enables modeling of the sorption process in the so-called “diffusion front” approximation (**Figure 13(a)**). This implies that the total  $\text{H}_2$  sorption time ( $\tau$ ) correlates linearly with the Pd concentration ( $C_{\text{Pd}}$ )

in the composite (**Figure 13(b)**) and quadratically with the nanocomposite film effective thickness  $L$  (**Figure 13(c)**) (the detailed calculation is available in **Paper VI**):

$$\tau \propto C_{Pd} L^2 \quad \text{eq. 6}$$

In the case of Teflon AF in **Paper VII**, due to the high  $H_2$  diffusivity, stage (i) is comparable to stage (ii), meaning that the total sorption time now is *independent* of the Pd concentration, when the film is sufficiently thin i.e. 100  $\mu\text{m}$  or less. When the thickness is increased, however, stage (i) starts to dominate the sorption process and therefore exhibits a quadratic dependence, as in PMMA.

# Chapter 5 - Nanoparticle-Polymer Hybrid Material Fabrication and Processing

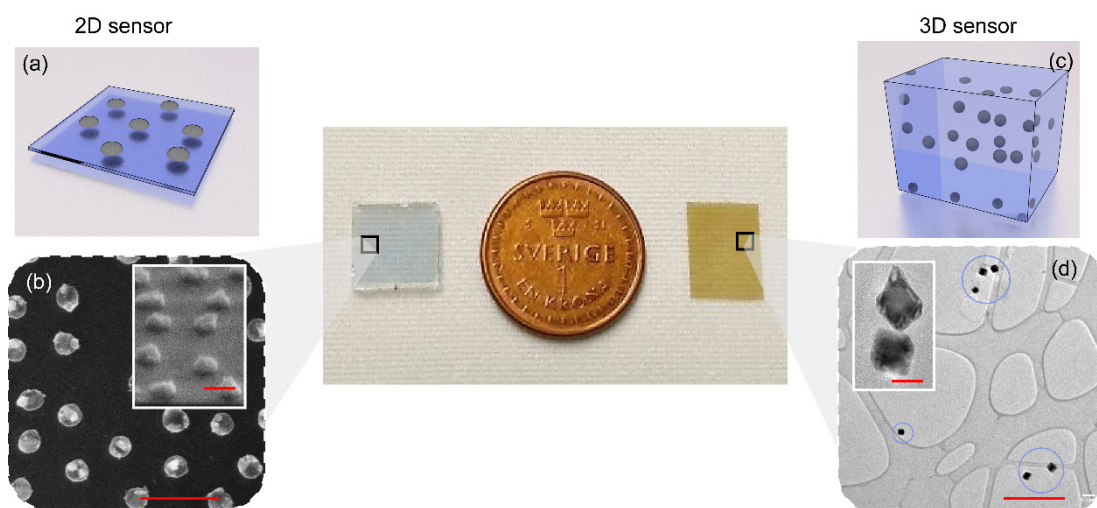


Figure 14: The two classes of hydrogen sensors I have studied: nanofabricated 2 dimensional- (left) and bulk-processed 3 dimensional- (right) nanoparticle - polymer composite hydrogen sensors with Pd nanoparticles as signal transducers, depicted together with a Swedish 1 krona coin. (a) Artist's rendition of a nanofabricated Pd nanoparticle array on a 2D support. (b) SEM image of a nanofabricated Pd-alloy nanodisk array (scale bar 500 nm). Inset: 70°tilted -view of the array (scale bar 200 nm). (c) Artist rendition of a bulk-processed 3D polymer matrix with dispersed colloidal Pd nanoparticles. (d) TEM image of Pd nanocubes in a PMMA matrix (blue circles are guides to the eye and the scale bar is 500 nm). Inset: HRTEM of two Pd nanocubes (scale bar 20nm). TEM and HRTEM images are courtesy of A. Stolaś and Dr. S. Lerch.

I have developed two different kinds of Pd nanoparticle - polymer composite hydrogen sensors, for which a photograph, showing an example each, is depicted in **Figure 14**. To the left, it shows the first type, which is comprised of a  $1 \times 1 \text{ cm}^2$  glass support patterned with an array of ca. 35 million Pd nanoparticles ready to capture hydrogen and signal its presence. To the right, it depicts an example of the second sensor type, which is comprised of a thick polymer film that contains an estimated 1 trillion colloidal Pd nanocubes per  $\text{cm}^3$ . I highlight that these two sensor types also are representatives for two fundamentally different approaches to fabricate nanostructured materials: *top-down* and *bottom-up*.

Since the two approaches constitute key concepts for my thesis, I have reserved this chapter to briefly discuss the top-down and bottom-up nanomaterial fabrication/synthesis strategies and to highlight their respective advantages and disadvantages.



# 1. Metallic Nanoparticle Synthesis: Top-down vs Bottom-up

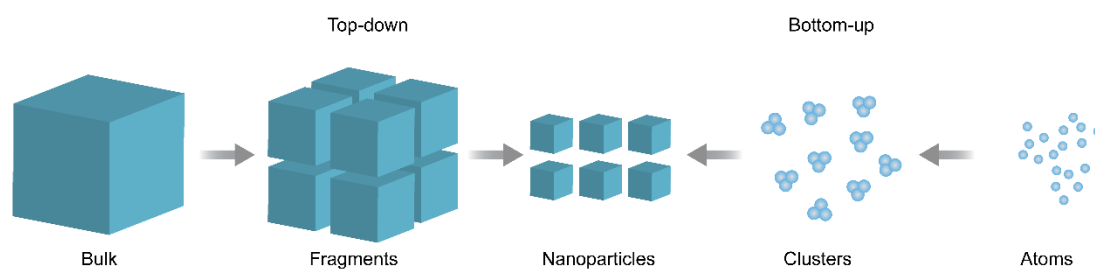


Figure 15: Top-down and bottom-up principles of nanoparticle creation. Top-down: A bulk piece of material is crafted into nanoparticles. Bottom-up: Atoms or other small building blocks assemble into small clusters, which further grow into nanoparticles.

The production of nanoparticles can be divided into two categories: top-down and bottom-up (Figure 15). The first strategy begins with a larger structure, which is crafted into smaller nanosized pieces. This is analogous to carving a figure from a large wooden block. On the other hand, the bottom-up concept starts with smaller units or building blocks (e.g. atoms, or molecules) and utilizes them to form larger structures by taking advantage of molecular interactions.<sup>216</sup> One can think of this approach as building a complex structure using Lego pieces – just at much smaller scale. Here, I limit the discussion of these two concepts to metallic nanoparticles only, since it is what I have worked with in my thesis.

Available techniques to form nanoparticles according to the top-down principle are numerous and include ball milling, focused ion beam nanomachining and nanolithography, to name a few.<sup>217,218</sup> Therefore, from this point forward, I will narrow down the discussion to nanolithography-based techniques only, due to their capacity to pattern nanoparticles on a support with high reproducibility. Nanolithography (ancient Greek: *lithos* = stone; *graphein* = to write), as the name suggests, is the creation of nanostructures in designated positions on a two-dimensional substrate. It comes in a large number of different versions, which can be grouped into two classes: direct inscription and pattern transfer. Examples of direct writing techniques are electron-beam and X-ray lithography and examples for pattern transfer techniques are photolithography, soft-lithography, and colloidal lithography. The direct inscription principle produces unmatched nanostructure feature size with freedom to assign the nanostructure location on the support, but the serial nature of the technique makes the production rate extremely slow, which escalates the cost. In contrast, pattern transfer techniques develop nanostructures in a parallel manner, thereby reducing the production rate and cost significantly.

Pattern transfer techniques rely on the use of a mask or a master cast to create a nanostructure. The most developed and heavily used technique of this class is probably photolithography, mainly driven by semiconductor industry in the effort to reduce the size of the transistors. Photolithography utilizes light (photons) to transfer the pattern from a mask to a sacrificial layer, which later serves as a template for the nanostructure development. Despite the excellent capacity to pattern complex nanostructures in parallel, photolithography is economically costly because the mask is prepared by direct inscription techniques mentioned

earlier. The cost issue has elicited efforts to avoid the use of masks by using a master cast or by employing colloidal nanobeads as self-assembled mask.

The master cast technique is also known as soft-lithography, due to its application of a self-assembly-patterned cast made from, e.g., the rubbery polymer PDMS. The use of colloidal nanobeads as masks for forming nanostructures on surfaces is known as colloidal lithography.<sup>219-221</sup> Although the patterned nanostructure in this case is defined by the shape and arrangement of the nanobeads, many complex shapes have been achieved, e.g. nanocrescents, nanotriangles, nanopillars, nanocones or nanoshuttlecocks.<sup>184,220,222,223</sup> One specific variant of colloidal lithography is hole-mask colloidal lithography (HCL) developed by Fredriksson *et. al.*,<sup>224</sup> which I have used widely to fabricate my 2D hydrogen sensors on flat surfaces. The key feature of HCL, compared to other colloidal lithography techniques, is the use of a sacrificial layer, which provides large freedom to customize the nanostructures in terms of used materials and in the third dimension.<sup>181,184,225</sup>

The number of methods that fall into the bottom-up category is also significant and the corresponding approaches can be classified according to from which phase the nanostructures are grown/synthesized, i.e. from the solid phase (e.g. physical vapor deposition), the liquid phase (e.g. chemical reduction, hydrothermal) or the gas phase (e.g. flame synthesis, laser pyrolysis).<sup>9</sup> Colloidal or wet-chemical synthesis in the liquid phase, is in general known to produce highly crystalline nanoparticles with narrow size distribution and the use of specific surfactants enables the growth of nanoparticles with non-trivial shapes, such as cubes, stars, or rods with well-define size. In wet-chemical synthesis, nanoparticles are grown on the basis of small clusters that precipitate from a super-saturated solution.<sup>226-228</sup> In this context, the chemical reduction of a metallic salt precursor is probably the most widely used wet-chemical synthesis approach for making metallic nanoparticles due to its simplicity. Moreover, the method allows the synthesis of particles in a wide range of size from 1 to 100 nm. On the downside, colloidal synthesis of nanoparticles is plagued by low reproducibility between synthesis batches, meaning that the nanoparticle properties will vary from batch to batch.

In this thesis, I have used colloidally synthesized Pd nanocubes (**Paper VI** and **VII**) and PdAu alloy nanoparticles (**Paper VIII**). These particles were synthesized by our collaborators in the group of Prof. Kasper Moth-Poulsen at the Department of Chemistry and Chemical Engineering at Chalmers.

## 2. Embedding Nanoparticles in a Polymer Matrix

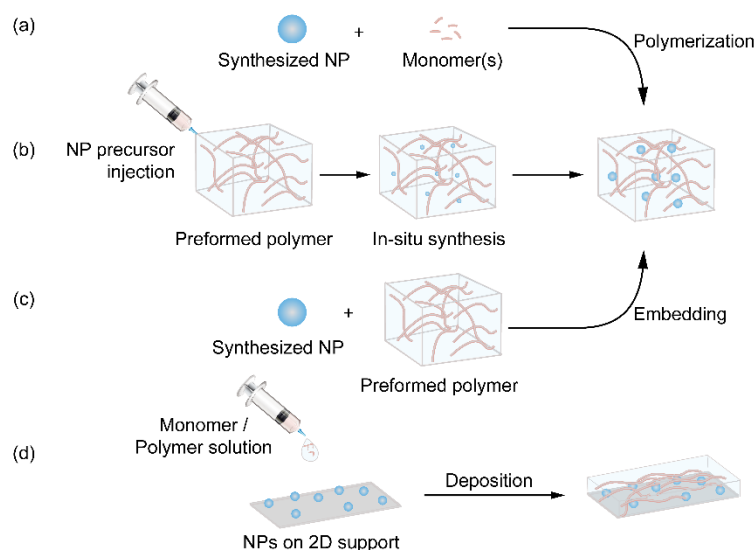


Figure 16: Four schemes for nanoparticle-polymer hybrid material creation: (a) Synthesized nanoparticles are premixed with monomer solution, followed by the polymerization step. (b) A nanoparticle precursor is injected into a preformed polymer matrix. The nanoparticles are subsequently synthesized in situ. (c) As-prepared nanoparticles are embedded into a preformed polymer matrix. (d) A polymer thin film is deposited onto nanoparticles, fabricated or by other means, deposited on a 2D support. Summarized from refs.<sup>21,22,229,230</sup>

The embedding of nanoparticles in a polymer matrix to form a nanoparticle-polymer hybrid material can be realized using different methods. The methods can be categorized as follows (illustrated in **Figure 16**):<sup>21,22,229,230</sup>

- Polymer formation in a nanoparticle suspension.* In this case, the monomers and crosslinker of the polymer precursor are mixed with a nanoparticle suspension. Polymerization is promoted by an external stimulus, such as heat or light.
- In situ nanoparticle synthesis.* A nanoparticle precursor is injected into the polymer matrix where the nanoparticles are subsequently synthesized in the polymer micropores. In this way, the micropores can be regarded as small microreactors.
- Physical embedding of nanoparticles into a preformed polymer matrix.* The embedding can be achieved for example by injecting a suspension of synthesized nanoparticles into a swollen polymer or by heating the polymer-nanoparticle mixture above the polymer melting point and compounding.
- Polymer coating on a nanopatterned substrate.* This method is usually applied to a nanopatterned 2D support. The coating can be applied for example using spin-coating or physical/chemical vapor deposition.

The choice on which of the above methods to use is often dictated by the nanoparticles and the polymer materials to be used. For example, method (b) requires a polymer of high free-

volume or a rubbery polymer. Physical embedding by heating above the polymer's melting point in method (c) might be problematic for high aspect ratio nanoparticles.

The chemical interaction between the nanoparticles and the polymer matrix can be either covalent or non-covalent, depending on the used material and the nanoparticle surface functionalization. For the plasmonic application I have targeted in my thesis, a covalent interaction is not intrinsically necessary but, as we have identified in **Paper IV**; plays a key role for the hydrogen sensing function.

Another aspect to consider when making nanoparticle-polymer hybrid materials is the fact that any heat treatment necessary during the embedding process might induce changes in the nanoparticle shape, size, distribution, crystallinity, and oxidation state.<sup>231</sup> For obvious reasons, the crystallinity degree is likely to improve by heat treatment. However, shape transformation is prone to take place for non-equilibrium shape nanoparticles, such as cubes and high aspect ratio rods. The nanoparticle size and distribution might change because polymer chains are dynamic above the glass transition temperature and therefore allow atomic diffusion (Ostwald ripening) and particles coalescence, which will lead to larger mean particle size. Example of this dynamic is the Au nanoparticle-PTFE composite where size and distribution changes was observed after heat treatment at 180°C for only 60 minutes.<sup>231</sup> As the final aspect to be mentioned here, I want to highlight that nanoparticles usually are highly reactive, meaning that they may oxidize by consuming oxygen from the polymer matrix already at low temperatures.<sup>231</sup>

In **Paper VI**, the Pd-PMMA hybrid material underwent heat treatment in 200°C for 10 minutes during the compounding process. HRTEM imaging revealed a slight transformation of the Pd-nanocubes (i.e., smoother edges) after embedding in the PMMA matrix. At the same time, both HRTEM and SAXS confirmed that the nanoparticle size as such did not change upon compounding, which indicates the absence of Oswald ripening or particle coalescence. This is most likely a consequence of the low Pd loading in the matrix (< 0.015 vol.%). In **Paper VII**, however, we observed Pd nanoparticle transformation from cube to sphere. The transformation might be due to the less stable nanoparticle which was synthesized using different surfactant/stabilizer (in this case PVP, instead of CTAB as in **Paper VI**) and the higher compounding process temperature (250°C).

### 3. Hole-Mask Colloidal Lithography (HCL)

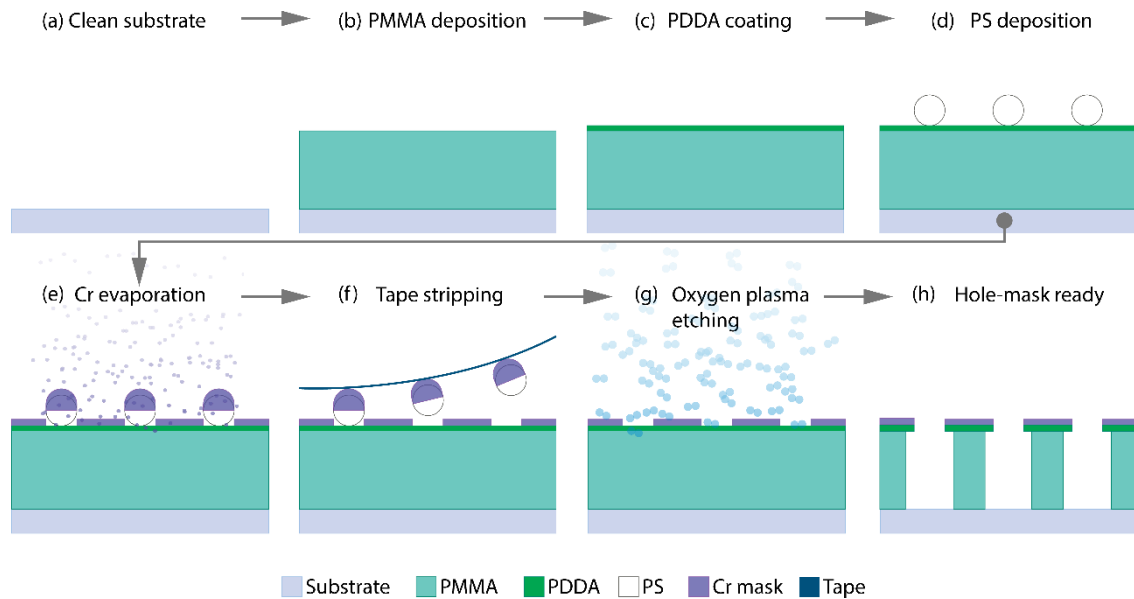


Figure 17: Hole-mask preparation steps in chronological order: (a) substrate preparation/cleaning, (b) PMMA sacrificial layer spin-coating, (c) application of positively-charged PDDA polyelectrolyte coating, (d) electrostatic self-assembly of PS nanobeads, (e) chromium mask evaporation, (f) tape stripping of PS nanobeads to create holes in the chromium mask, (g) oxygen plasma etch of the PMMA layer through the hole-mask. The final developed mask is illustrated in (h).

A schematic illustration of the hole-mask preparation sequence is presented in **Figure 17**, and below I provide some more detailed information about the individual steps:

- (a) The substrate (typically fused silica or a silicon wafer) is cleaned subsequently with isopropanol (IPA), acetone, methanol, and IPA (again). Cleaning with each solvent is performed for 30 seconds in an ultrasonicator. The purpose of this cleaning is to remove dust or any organic contaminants on the substrate.
- (b) PMMA sacrificial layer deposition by spin-coating and subsequent soft-baking. I use anisole-diluted PMMA A4 solution (Mw = 950 000, Microchem AB) for this purpose. The substrate is placed on a spinner and few drops of PMMA solution are applied on to the substrate. An approximately 200 nm thick PMMA film is then obtained by spinning at 2000 rpm for 60 seconds. Afterwards, the coated substrate is soft-baked at 170°C for 3 minutes to evaporate the remaining solvent. The spin-coating process is discussed in the “Nanofabrication Toolbox” panel below.
- (c) Positively-charged poly(diallyldimethylammonium chloride) (PDDA) solution is drop-coated onto the PMMA sacrificial layer. PDDA is purchased from Sigma Aldrich (Mw = 100 000 - 200 000 diluted in 20% H<sub>2</sub>O) and diluted in water to achieve 0.2 wt.% concentration. Prior to PDDA drop coating, the PMMA layer is exposed to oxygen plasma (50 W, 250 Torr, 10 sccm) for 5 seconds to reduce surface hydrophobicity. The drop coated PMMA is then incubated for 1 minute followed by washing with Milli-Q water for 10 seconds and nitrogen blow-dry.

- (d) Negatively-charged polystyrene (PS) nanobeads are drop cast onto the PDDA-coated PMMA sacrificial layer. The original PS nanobead stock-solutions were purchased from Life Technology and diluted in Milli-Q water to 0.2 wt% concentration. The diluted PS solution is then drop coated and incubated for 2 minutes to enable the self-assembly of a scarce monolayer of PS beads on the surface, followed by a 10 s rinse in Milli-Q water. The sample is later dried under a stream of nitrogen gas.
- (e) 15 nm Chromium mask growth by e-beam physical vapor deposition (PVD).
- (f) Tape stripping to remove the nanobeads, leaving holes in the Chromium mask where the PMMA now is exposed.
- (g) 5 min oxygen plasma etch (50 W, 250 Torr, and 10 sccm) to transfer the hole-pattern into the PMMA. The oxygen plasma etching was done using plasma reactive-ion etching (PE-RIE) discussed in the “Nanofabrication Toolbox” panel below.
- (h) The final structure of the hole-mask.

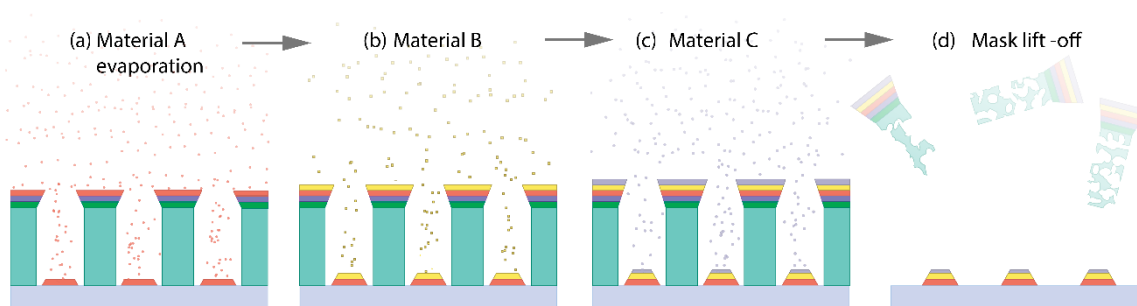


Figure 18: Material deposition through the hole-mask. One or more materials can be sequentially evaporated through the mask by e-beam PVD. Illustrated in (a)→(c): metal A, B, and C are sequentially deposited. Afterwards, the mask is lifted-off with organic solvent, leaving only the layered nanodisk structures on the surface (d). Note the truncated cone shape of the formed structures, which is the consequence of the mask slowly closing upon material deposition.<sup>184</sup>

After the hole-mask is prepared, material deposition through the mask is performed by using e-beam PVD (this technique is discussed more in detail in the “Nanofabrication Toolbox” panel below). If desired, multiple materials can be evaporated subsequently through the mask to, for example, enable the fabrication of layered structures (**Figure 18**). In the case of alloy fabrication, the alloyant composition is controlled by adjusting the thickness of the layers.<sup>232</sup> After the material deposition step, the mask together with all material deposited on top of it, is removed in a lift-off step by dissolving the PMMA in an organic solvent such as Acetone. This yields a quasi-random array of disk-like nanoparticles on the surface as shown in **Figure 14(b)**.

### 3.1. Alloying via Annealing

If the goal of the nanofabrication is to make metal alloy nanoparticles, the layered structures obtained by depositing different materials through the mask can be thermally annealed in reducing atmosphere (4% H<sub>2</sub> in Ar) to induce homogeneous alloy formation, if that is thermodynamically favored.<sup>57,232</sup> For the Pd-alloy sensors, I annealed the as-prepared sample, comprised of a Pd and Au or Cu layer adjusted to match the desired alloy stoichiometry, at 500°C for 24h in 100 mL/min 4vol.% H<sub>2</sub> in Ar carrier gas. In the case where the alloy was prepared on a QCM crystal, the annealing was done at 250°C for 72 h to on one hand avoid breakage of the QCM crystal and on the other hand, still provide enough time for homogeneous alloy formation, which is slower due to lower atomic mobility at lower temperature.

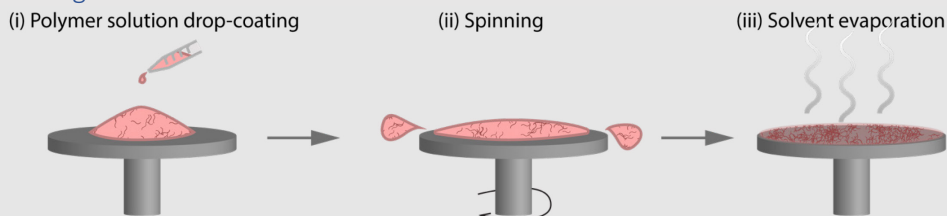
### 3.2. Applying a Polymer Thin Film Coating on the Nanofabricated Surface

Two types of polymers were used to coat the nanofabricated 2D hydrogen sensor surfaces: PMMA and PTFE. To achieve PMMA layers of ca. 50 nm thickness (**Paper IV**), anisole-diluted PMMA A1 (Mw 950 000, Microchem AB) was spin-coated at 2000 rpm for 30s, followed by soft-baking at 170°C on a hotplate for 3 minutes. The PTFE deposition was done via DC/radio frequency magnetron sputtering by our collaborators in the group of Prof. Bernard Dam at Delft University in the Netherlands, as described in detail in ref.<sup>233</sup>

## Supplementary Information: Nanofabrication Toolbox

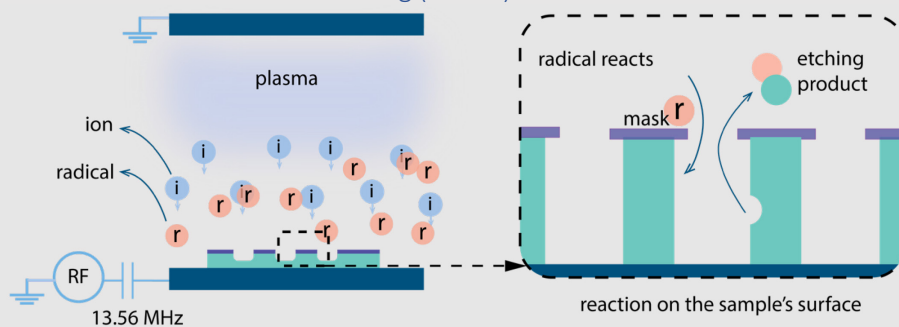
In this panel, I present schematics of the three tools I used for hole-mask colloidal lithography nanofabrication: (i) spin coating, (ii) plasma-enhanced reactive ion-etching (PE-RIE), and (iii) electron-beam physical vapor deposition (e-beam PVD).

### Spin coating



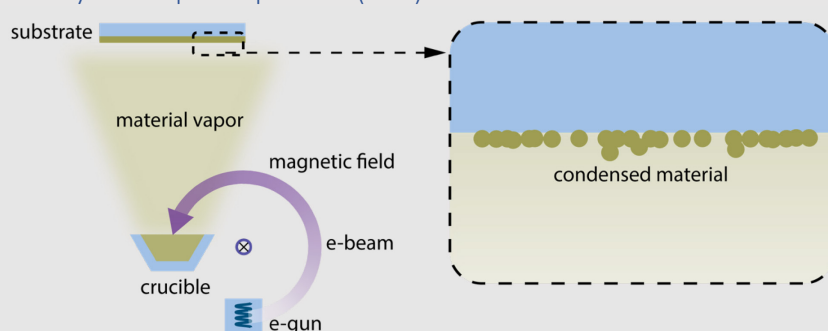
*Scheme SI 1: Polymer deposition by spin coating. The three main steps are (i) drop-coating of solvent-diluted polymer, (ii) spinning to create centrifugal force that removes excess solution, and (iii) soft baking to evaporate the solvent and form a dense polymer film.*

### Plasma-enhanced Reactive Ion Etching (PE-RIE)



*Scheme SI 2: Schematic of the plasma-enhanced reactive ion-etching process (adapted and modified from<sup>256</sup>). Plasma is generated in between the two electrodes. The anode is connected to a radio-frequency generator. Plasma induces ion and radical formation in the feeding-gas (in my case  $O_2$  for PMMA etching). In the inset, reactive radicals adsorb onto the sample surface to promote the etching reaction. In this case, I relate the illustration to the etching process of the PMMA sacrificial layer explained earlier in the hole-mask colloidal lithography section in Figure 17(g).*

### Electron-beam Physical Vapor Deposition (PVD)



*Scheme SI 3: Schematic of electron-beam physical vapor deposition (e-beam PVD). Electrons are generated by a heated-filament and directed by a perpendicular magnetic field onto the material source/crucible. The thereby heated material evaporates towards the substrate placed above the crucible in high vacuum. Material vapor adsorbs on the substrate and condenses and nucleates to form a thin film.*



## 4. Bulk-Processing of Pd Nanoparticle-Polymer Hybrid Materials

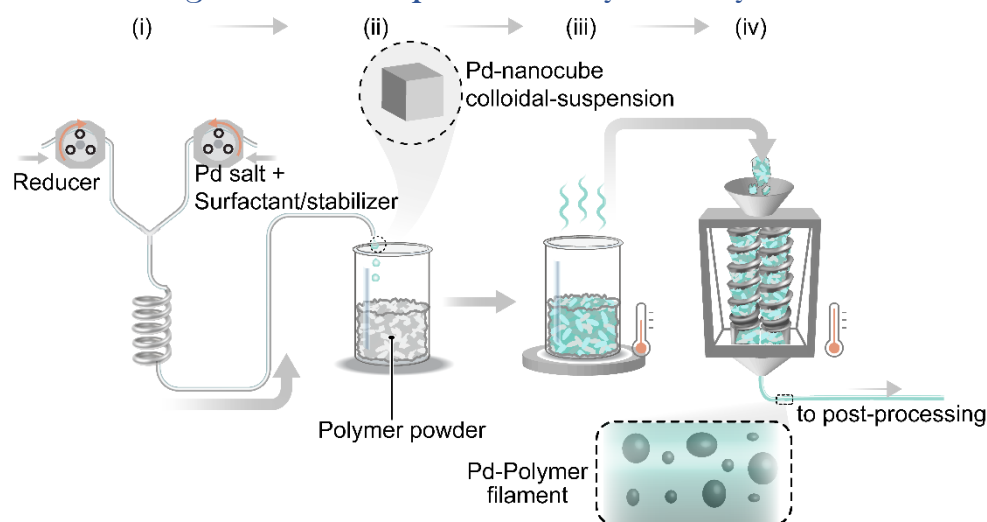


Figure 19: Bulk Pd-polymer hybrid material processing scheme. The process begins with the colloidal synthesis of Pd nanocubes (i), followed by mixing of the nanoparticle suspension with a polymer powder (ii). Next, the mixture is heated to evaporate excess solvent (iii) and the dried mixture is inserted into a twin-screw melt-extruder to produce uniform Pd-polymer hybrid filaments.

### 4.1. Colloidal Synthesis of Pd Nanocubes

The general steps of the colloidal synthesis of the Pd nanocubes (**Figure 19(i)**) I have worked with can be summarized as follows. First, a Pd-salt ( $\text{Na}_2\text{PdCl}_4$ ) solution is prepared and then mixed with a surfactant/stabilizer (CTAB or PVP). Next, the mixture is heated to certain temperature (80-95°C). Then, the reducing agent ascorbic acid (AA) is mixed into the metal-salt and surfactant/stabilizer solution. AA reduces the  $\text{Pd}^{2+}$  ions in the precursor into neutral  $\text{Pd}^0$ . At instant time,  $\text{Pd}^0$  atoms start to coalesce into small clusters/nuclei, which serve as the basis for subsequent nanoparticle growth. Furthermore, growing nanoparticles are covered by a layer of surfactant/stabilizer molecules that both prevent nanoparticle aggregation and stimulate the preferential growth of specific facets, thereby controlling the shape of the formed particles. In our case, we employed CTAB (**Paper VI**) and  $\text{KBr/KCl/PVP}$  (**Paper VII**) as surfactant/stabilizer, since they promote the growth of particles with cubical shape.<sup>234,235</sup>

### 4.2. Nanoparticle-Polymer Hybrid Material Compounding

The hybrid material compounding was initiated with pouring the colloidal nanoparticle suspension into the polymer powder, followed by a drying step at 80°C overnight to evaporate excess solvent, as depicted in **Figure 19(ii-iii)**. The dried mixture was then compounded in a twin-screw micro extruder for 5 minutes at temperatures above the polymer's melting point, and subsequently extruded into a filament with diameter of 1.75 mm **Figure 19(iv)**.

### 4.3. Post-Processing: Melt-Pressing of Thin Plates or 3D printing

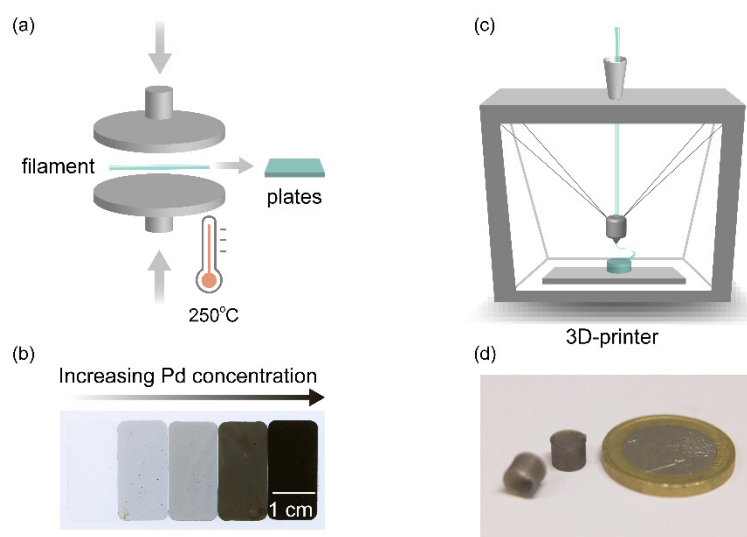


Figure 20 Pd-polymer nanocomposite material filament post processing: melt-pressing and 3D printing. (a) Filament melt-pressing to prepare Pd-polymer hybrid plates in the thickness range from 50 to 500  $\mu\text{m}$ . (b) Photograph of melt-pressed Pd nanocube-PMMA nanocomposite material plates for five different Pd concentrations (from left to right: 0.00, 0.02, 0.03, 0.06, and 0.16 wt %, respectively). (c) Scheme of the 3D printing process used to print Pd nanocube-PMMA sensor “caps” that can be mounted on optical fibers by “plug-and-play”. (d) Photograph of the 3D printed Pd nanocube-PMMA nanocomposite sensor caps together with a 1 Euro coin.

To create hydrogen sensors based on the Pd nanocube-PMMA nanocomposite we used two post-processing steps: (i) melt-pressing to prepare thin plates and (ii) fused filament fabrication (commonly known as 3D printing) to print Pd nanocube-PMMA “caps” that can be mounted on optical fibers by “plug-and-play”. For (i), the plate was produced by pressing a short filament piece with a hot press (AB Nike Hydraulics) at 250 °C by applying 5 tons for 3 min, followed by 10 tons for 2 min. The plate thickness is adjusted by using different thickness metal spacers yielding plates of 50-500  $\mu\text{m}$ . For (ii), we employed a Massportal Pharaoh XD 3D printer. The printing was done at 60°C build-stage temperature and 210°C nozzle temperature with 1000 mm/min printing speed.



# Chapter 6 - Material Characterization

I have utilized various material characterization techniques to verify successful nanofabrication or bulk processing of (alloy) nanoparticles and nanoparticle-polymer nanocomposite materials, and to be able to link structural features to sensor performance.

One example to illustrate the importance of, but also the challenge with, material characterization is the bulk-processed Pd-PMMA nanocomposite material developed and presented in **Paper VI**. Since this material was completely new when we first created it, detailed characterization from the atomic to the macroscopic level was critical to understand the factors that control its performance in a hydrogen sensor. One question was whether the long response time of the system upon exposure to hydrogen was due to aggregated Pd nanoparticles across the PMMA matrix or if it was solely due to low diffusivity of hydrogen in the PMMA matrix. Eventually, the conundrum was clarified with both transmission electron microscopy (TEM) and small angle X-ray scattering (SAXS), as discussed in the paper.

Because of the importance of material characterization to understand functionality, I discuss some main techniques here.

*Table 2: The material characterization techniques used in this thesis.*

No.	Technique	Purpose	Used in Paper-
1	Scanning electron microscopy (SEM)	to obtain images of the nanofabricated nanoparticle arrays to derive nanostructure size distribution and surface coverage.	I, II, III IV, V
2	Energy-dispersive X-ray spectroscopy (EDX)	to obtain information about the elemental composition of my samples.	II, IV, VIII
3	Transmission electron microscopy (TEM)	to obtain high resolution images of Pd and Pd alloy nanoparticles.	VI, VII, VIII
4	X-Ray photoelectron spectroscopy (XPS)	to measure the elemental surface composition of the nanofabricated samples, as well as surface oxidation state and alloyant surface segregation effects.	II, IV, V
5	Quartz crystal microbalance (QCM)	to quantify the amount of hydrogen absorption by the nanofabricated Pd-alloy nanostructures	I
6	Small Angle X-Ray Scattering (SAXS)	main purpose was to characterize the bulk-processed Pd-polymer nanocomposite materials, due to its ability to investigate material features over a wide range of length scales, i.e., from the level of the individual nanoparticle to the overall nanoparticle distribution at the macroscopic scale.	VI, VII

*Disclaimer:* I performed SEM, XPS, and QCM analysis myself. EDX, TEM analysis were done by my collaborators in the group of Prof. Kasper Moth-Poulsen and SAXS measurements were done by my collaborators in the group of Prof. Marianne Liebi, both at Chalmers.

# 1. Scanning Electron Microscopy (SEM)

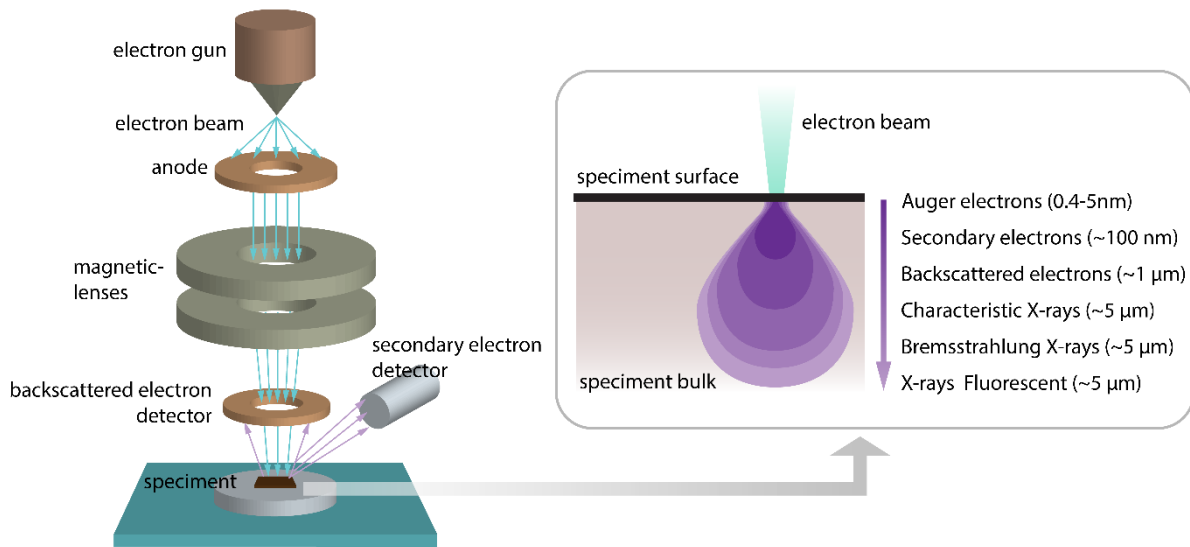


Figure 21: Schematic of a scanning electron microscope (SEM) (not to scale). The electrons are generated by an electron gun and then focused onto and rastered across the specimen by magnetic lenses. Inset: the profile of the generated signals from the specimen depending on the depth. For SEM imaging only the secondary and the backscattered electrons are used (adapted from refs.<sup>236,237</sup>)

The key components of a SEM instrument are the electron gun, magnetic lenses, scan coils, and the electron detector (**Figure 21**). The electron beam emitted from the gun is directed to the sample surface by two magnetic lenses: the condenser and the objective lens. The condenser lens focuses the electrons emitted by the source before it enters the objective aperture. Here, a strong condenser lens is needed to ensure that the electron beam does not spread too widely. Right before the beam enters the objective lens, its direction is controlled with the scanning coil. Finally, the objective lens focuses the beam onto the sample surface. When impinging on the surface, the electron beam induces the emission of multiple types of particles and photons, including X-rays, visible photons (cathodoluminescence), secondary electrons (SE) and backscattered electrons (BSE). As indicated in **Figure 21**, these different products are all generated at different sample surface depths. SEs are generated close to the surface and, thus, carry surface (topography) information. BSEs are emitted from deeper inside the sample (bulk) and thus can be used to identify material composition.

Like any other microscopy technique, the aim of SEM is to obtain the best possible image resolution. To achieve this, there are many factors to consider. For example, since the sample surface is flooded with electrons during imaging, the sample must be sufficiently conductive to transfer excess charge to ground. Hence, to obtain an image with high resolution from an insulating sample (e.g., glass) is usually more difficult than from a metal. Similarly, the used acceleration voltage of the electron beam is important for the obtained resolution. Higher acceleration voltage leads to deeper electron penetration on the sample surface, which also broadens the interaction volume. This broadening means that the scattered electron signal comes from larger area, which consequently reduces the lateral resolution.<sup>236,238</sup> The working distance (i.e. distance between objective lens and sample surface) determines the depth of focus and a shorter working distance means an increase of depth of focus. Hence, to have the

right working distance is crucial for imaging structures with high aspect ratio and for imaging at an angle. Finally, good resolution is enabled only when the microscope chamber pressure is sufficiently low to minimize electron scattering from molecules in the chamber. Practically, I used a Zeiss Supra 60 VP and I prepared the imaged nanostructures on reasonably conducting silicon substrates to minimize charging effects. As the typical working distance, I used 5 mm, together with an accelerating voltage of 10-15 kV.

## 2. Energy Dispersive X-Ray Spectroscopy (EDX)

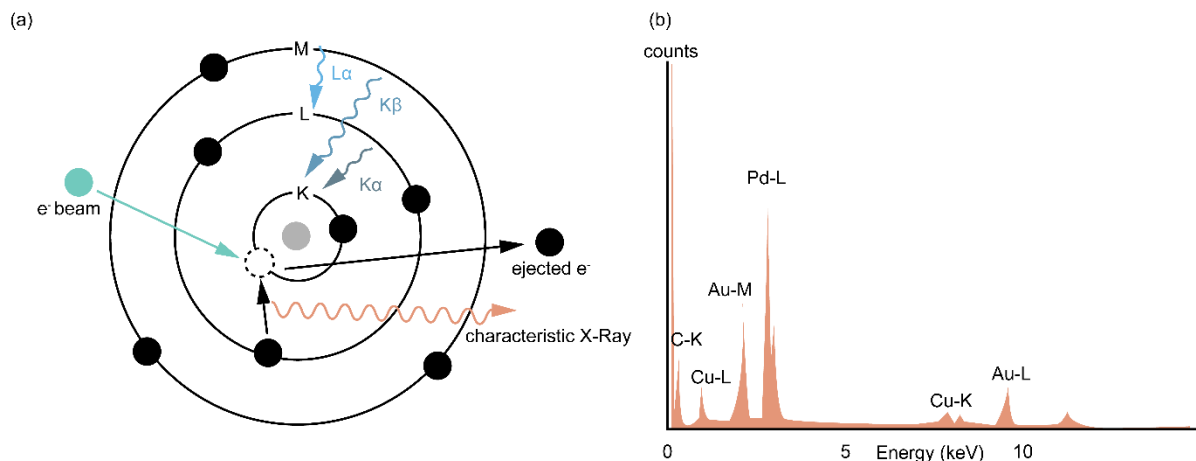


Figure 22: (a) Illustration of the energy dispersive X-ray spectroscopy (EDX) principle. The incoming electron beam knocks out a core electron from the sample. Subsequently, an electron from a higher-energy orbital relaxes to fill the abandoned orbital, thereby emitting an X-ray photon with an energy characteristic for the specific orbital transition. (b) A typical EDX spectrum in which X-ray intensity counts are displayed as a function of energy. Each peak represents an orbital transition specific to an element and can thus be regarded as the element's "fingerprint". Courtesy of Dr. S. Lerch.

EDX is a useful spectroscopy method that can be combined with electron microscopy. In principle, one can simply add an X-ray detector to an electron microscope to perform EDX since, as depicted in **Figure 21**, X-rays are produced upon impact of the electron beam on the specimen. These X-rays stem from a volume that extends approximately 5  $\mu\text{m}$  below the specimen surface and there are two kinds of generated X-rays: characteristic and Bremsstrahlung. Bremsstrahlung is the product of the beam electrons' kinetic energy loss due to interaction with the atomic cores of the specimen. Characteristic X-rays are generated by electronic transitions of the specimen's atoms upon interaction with the incoming electron beam. Specifically, the beam knocks a core electron from its orbital, thereby creating a hole. Subsequently, an electron from an outer orbital undergoes a transition to occupy the available core hole. This transition leads to the emission of X-rays that carry element-specific energy corresponding to the specific transition, which therefore can be used to identify the elements present in the specimen. For EDX, only characteristic X-rays are of interest. EDX can be used for both qualitative and quantitative analysis. However, there are limitations, such as peak overlap, poor energy resolution ( $\sim 100$  eV) and difficulties to detect lighter elements.

### 3. Transmission Electron Microscopy (TEM)

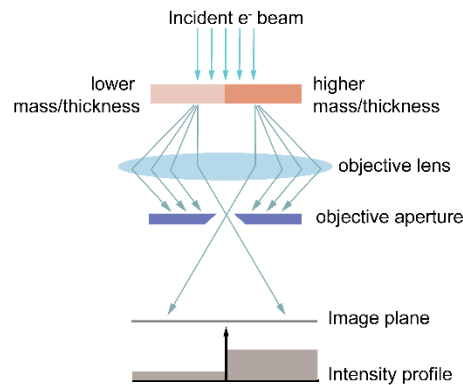


Figure 23: Illustration of the transmission electron microscope (TEM) imaging mechanism (not to scale). The amount of electron transmission through the specimen depends on the local mass/thickness. The lower (higher) mass/thickness the higher (lower) the intensity profile on the image plain. The objective lens and aperture ensure that only transmitted electrons reach the image plane, while the scattered electrons are omitted.

For nanoparticles smaller than 100 nm, high resolution imaging is difficult using SEM. Therefore, transmission electron microscopy (TEM) is employed instead. In the high-resolution mode (HR-TEM), direct imaging of the atomic arrangement can be achieved.

The TEM imaging principle is illustrated in **Figure 23**. In brief, the electron beam is generated by similar system as found in an SEM (**Figure 21**) and directs the beam of electrons, which is in the 80-200 kV range and therefore a lot higher than in SEM, towards the specimen. The intensity of the transmitted electrons depends on the local mass/density of the specimen. Hence, bright/dark colors in a TEM image represent areas with low/high electron density. To allow electron transmission, both specimen and support for TEM imaging must be as thin as possible (< 100 nm).

## 4. X-Ray Photoelectron Spectroscopy (XPS)

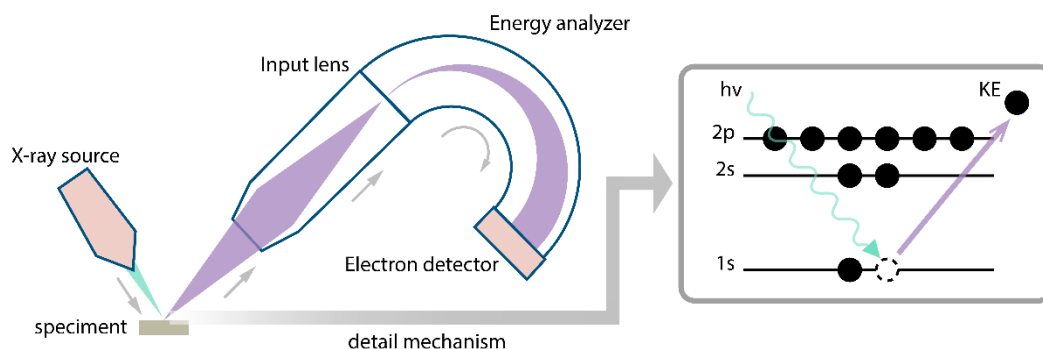


Figure 24: Schematic depiction and mechanism of X-ray photoelectron spectroscopy (XPS) (not to scale), as simplified from ref.<sup>239</sup>

XPS enables non-destructive surface characterization of a material with a surface sensitivity of 0.5-10 nm (depending strongly on the material) and composition detection limit of 0.1-1 atomic percent.<sup>240,241</sup> The working principle is as follows. An X-ray beam is irradiated on to the sample surface and knocks out a core electron to the vacuum level, leaving behind a core hole (**Figure 24**). Accordingly, dictated by the energy conservation principle, the core electron binding energy,  $BE$ , can be expressed as:

$$BE = hv - \phi - KE, \quad \text{eq. 7}$$

where  $hv$  is the energy of the incoming X-ray photons (in my case 1486.6 eV for Al-K $\alpha$  radiation),  $\phi$  is the work function of the specimen and  $KE$  is the kinetic energy of the ejected electrons. By analyzing the kinetic energy of the ejected electrons (practically done by sorting the electron in a perpendicular magnetic field), one can thus obtain the core electron binding energy. Since the core electron binding energies are unique for each element of the periodic table, it can be used for surface elemental analysis. Furthermore, small shifts in binding energy generally contain information about, for example, the oxidation state of the surface. An oxide has generally a higher binding energy than a metal because the valence electrons are displaced towards the oxygen atoms, which leads to a more positively charged site. This more positive core, thus, increases attraction to the remaining electrons<sup>242</sup>. Practically, shifts towards higher  $BE$  usually means increasing oxidation state, while shift towards lower  $BE$  means more reduced state. For example, the 3d<sub>5/2</sub> peak of PdO is 336.4 eV, which is higher than the metallic Pd peak at 335.4 eV.<sup>243</sup>

For my work, I have used a PHI 5000 XPS system and samples prepared on a conducting substrate such as Si. As reference for the energy scale, I used the carbon 1s peak by shifting the entire spectrum to match the carbon 1s standard value of 384.5 eV. I used XPS extensively to investigate surface segregation in the Pd-alloy system (**Paper II**) and to quantify surfactant/stabilizer ligands on Pd nanofabricated Pd (**Paper V**).



## 5. Quartz Crystal Microbalance (QCM)

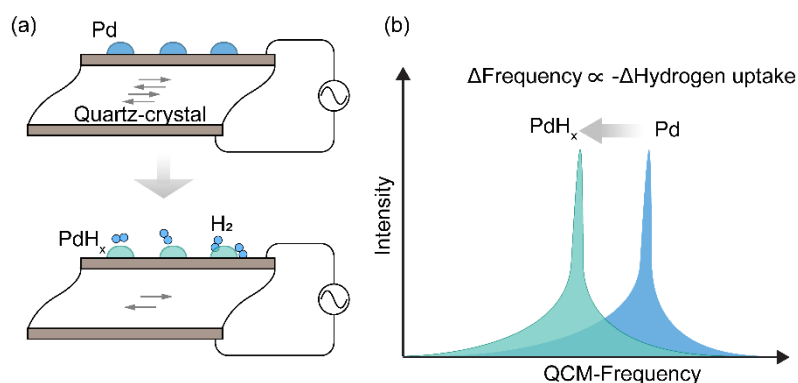


Figure 25: Quartz crystal microbalance (QCM). (a) A schematic depiction of measuring hydrogen absorbed by Pd nanoparticles using a QCM crystal (not to scale). (c) Typical response of the QCM sensor. The frequency shift ( $\Delta f$ ) is proportional to the mass change (hydrogen uptake by the Pd) on the crystal ( $\Delta m$ ).

I have used QCM to quantify the amount of hydrogen absorbed by nanofabricated Pd and Pd alloy nanoparticles, and to correlate this information with their optical LSPR response in **Paper I**. The QCM is basically a highly sensitive scale that employs a simple harmonic oscillation principle, where the resonance frequency change ( $\Delta f$ ) scales linearly with the change in mass per unit area ( $\Delta m$ ) on the resonator. The weighing mechanism is illustrated in **Figure 25(a)**: an applied external AC bias drives a shear oscillation of the piezoelectric QCM crystal. For my project, I nanofabricated Pd alloy nanoparticles on the QCM crystal. The relation between frequency change of the QCM crystal and the mass change on top of it is formally known as Sauerbrey equation.<sup>244</sup>

$$\Delta f = -C_f \Delta m, \quad \text{eq. 8}$$

where  $C_f$  is the sensitivity factor that depends on the used crystal type. The typical response of the QCM sensor is depicted in **Figure 25(b)**, where there is a sharp harmonic peak over the frequency sweep. For the 10 MHz SC-cut crystals I have used in this work,  $C_f$  is 4.8 ng cm<sup>-2</sup> Hz<sup>-1</sup>. The QCM instrument unit I used was a QSense Explorer by Biolin Scientific.

## 6. Small Angle X-ray Scattering (SAXS)

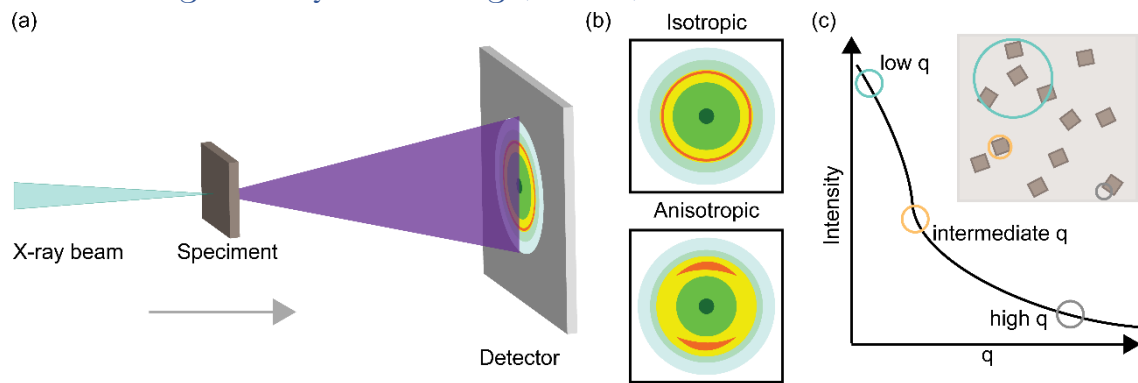


Figure 26: Small Angle X-ray Scattering (SAXS). (a) A simplified SAXS experimental setup (not to scale). An X-ray beam is focused on a small area on the specimen. The specimen scatters the X-ray photons, which then are recorded by a photodetector placed at long distance. For SAXS, only photons scattered with a small scattering angle of a few radians are collected. (b) Typical 2D-projections of the scattered photons produced by an isotropic (top) or anisotropic (bottom) material. (c) Typical intensity ( $I$ ) vs scattering angle ( $q$ ) curve of which the  $q$  domains correspond to a certain length-scale regime in the sample (color coded).

Small Angle X-ray Scattering is a non-destructive characterization technique to determine averaged particles shape, size, and distribution of a specimen. The small angle refers to  $0.1^\circ$  to  $10^\circ$ .<sup>245</sup> The basic SAXS setup is depicted in **Figure 26(a)**, where a specimen of typically about hundred micrometer thickness is placed between an X-ray source (4.4 – 17.9 keV)<sup>246</sup> and a photon detector. The X-ray beam is focused on the specimen surface and scattered photons within a small collection angle of a few radian only are collected by the detector in a transmission configuration. The typically obtained 2D projection of the scattered photons is shown in **Figure 26(b)**. The 2D projected pattern carries information about the preferred orientation of material sub-units (the nanoparticles dispersed in the polymer matrix in my case) in each specific pixel ( $40 \times 40 \mu\text{m}$ ). A typical 2D projection of the scattered electron is depicted in **Figure 26(b)**. An isotropic or anisotropic feature can be determined by the symmetry of the projection.

SAXS's ability to characterize samples across a very wide range of length scales can be demonstrated by plotting the scattering intensity ( $I$ ) vs the scattering angle ( $q$ ), as depicted in **Figure 26(c)**. Presented on the example of my polymer-nanoparticle composites, the profile of the  $I$  vs  $q$  curve carries information all the way from particle structure at atomic level (high  $q$ -range) to the particle distribution in the matrix (low  $q$ -range). Formally,  $I$  vs  $q$  can be represented as:

$$I(q) = k P(q)S(q) \quad \text{eq. 9}$$

Therefore, the scattered intensity is a product of the material character- ( $k$ ), form- ( $P$ ) and structure-factor ( $S$ ). The form factor carries information on the shape of the particles and its intra-particle structure. The structure factor relates to particle-particle interactions e.g. average distance between particles and the particles ordering. In principle, by obtaining the nanoparticle size/shape from TEM, one can construct the  $P$  and therefore calculate the  $S$  to get the interparticle information.



# Chapter 7 Hydrogen Sensor Test Setups

In this chapter, I will discuss the four different hydrogen sensor test setups I have used, where the selection of a specific setup was dictated by the type of metrics I intended to measure.

No	Setup	Measurement type
1	Vacuum chamber	Pressure composition isotherm and hydrogenation kinetics measurements in vacuum/pure hydrogen
2	Atmospheric pressure flow reactor (Insplorion X1)	Cross-sensitivity and poisoning/deactivation tests at ambient conditions in Ar or synthetic air
3	Fiber optic feedthrough reactor	3D-printed sensor cap testing at ambient conditions in Ar or synthetic air
4	Fast-switch mini reactor	Fast hydrogenation kinetics measurements in synthetic air background at ambient pressure

Table 3 List of hydrogen sensor test setups used in this thesis.

## 1. Vacuum Chamber

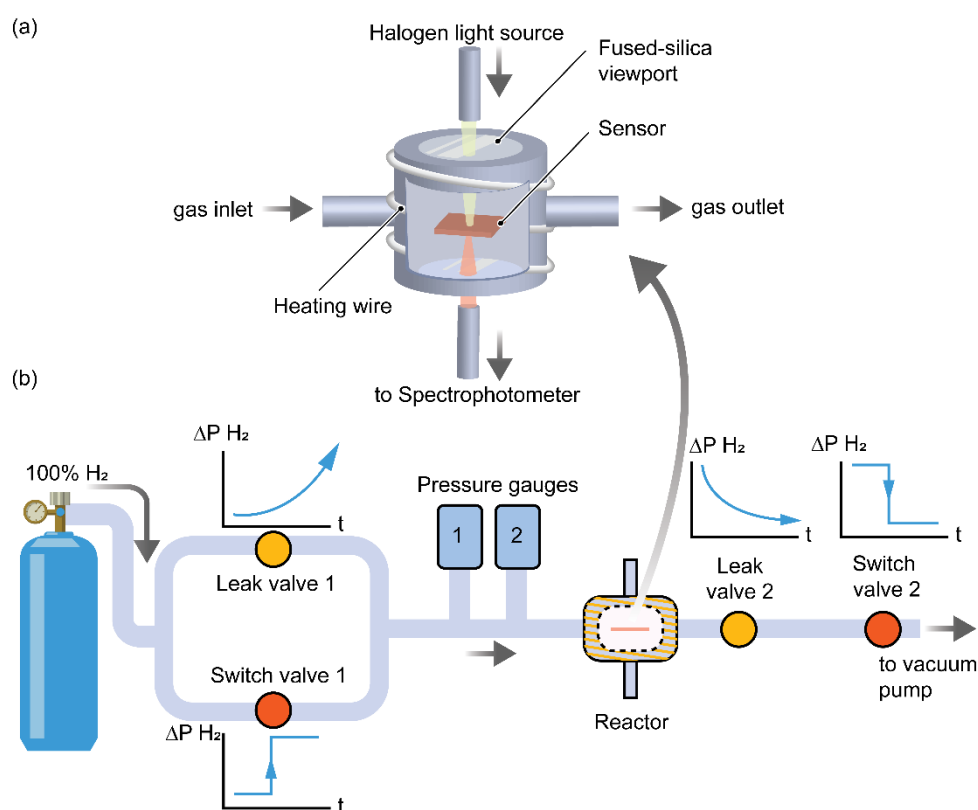


Figure 27: Schematic of the vacuum chamber hydrogen sensor test setup. (a) The vacuum chamber with the pure hydrogen inlet/outlet and two fused silica viewports for transmission-mode optical measurements. The chamber is wrapped with a heating coil for the temperature conditioning. (b) Schematic of gas lines and control system. The gas pressure in the chamber is controlled using either leak valves (for continuous pressure change in the isotherm measurements) or switch valves (for stepwise pressure change in the kinetics measurements). Two capacitive pressure gauges with different dynamic range are installed for absolute pressure monitoring.

The vacuum chamber (effective volume  $\approx 40$  mL), illustrated in **Figure 27(a)**, is wrapped with a heating coil and the interior temperature is monitored by a thermocouple in contact with the hydrogen sensor chip. The heating coil and the thermocouple are connected to a Eurotherm thermocontroller (Eurotherm 3216), which regulates the chamber temperature in a feedback-loop manner. The chamber is equipped with two fused-silica viewports (1.33" CF Flange, Accu-Glass), which enable transmission mode optical measurements using a fiber-coupled polychromatic halogen light source (Avantes AvaLight-Hal) and a fixed-grating spectrophotometer (Avantes SensLine AvaSpec-2048XL).

The chamber is connected to a pure 100% hydrogen source at one end and to a turbo vacuum pump at the other end, as depicted in **Figure 27(b)**. Hydrogen pressure in the chamber is controlled by either a leak valve or a pneumatic valve. The leak valve is utilized in the hydrogen pressure-composition measurements, which require a gradual pressure ramp up to 1 atm. The leak valve #1 is Variable Leak Valve model 951-5106/52035 (Varian Vacuum Technology) and leak valve #2 is Metering Bellows Sealed Valve model SS/4BMW/VCR (Swagelok). The pneumatic valve (Nupro) is used for the kinetics measurement, where fast switching is critical. The chamber pressure is monitored by two capacitance pressure gauges (MKS Baratron 626C) of different pressure range. The first manometer is used to monitor 1-1000 mbar pressure, while the second one is for 1-1000  $\mu$ bar.

## 2. Atmospheric Pressure Flow Reactor (Insplorion X1)

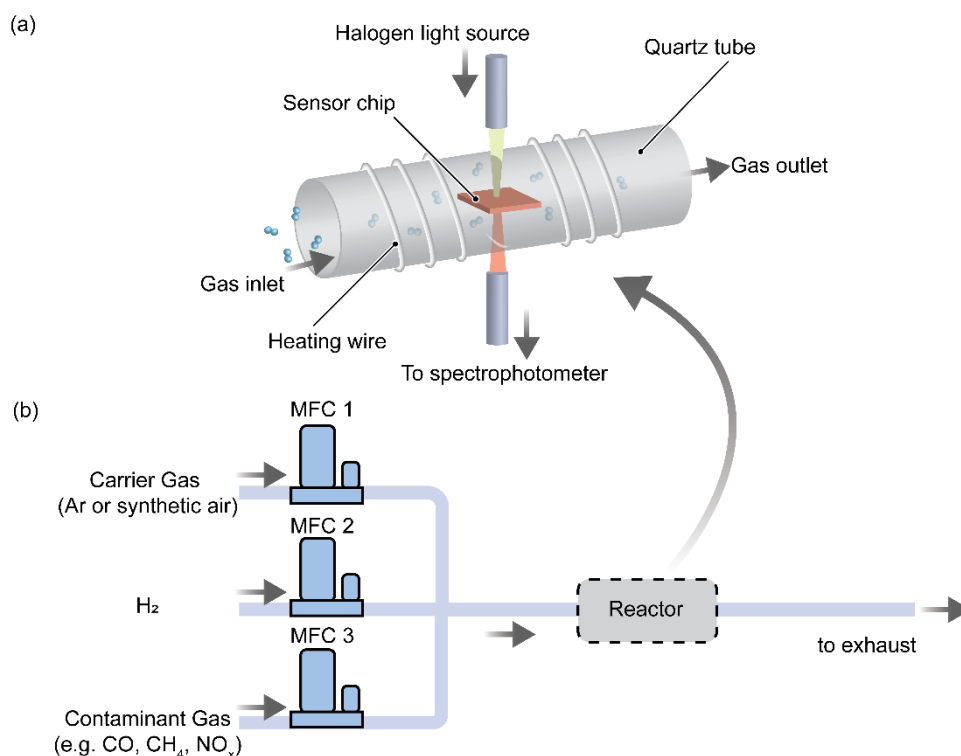


Figure 28: Schematic of the Insplorion X1 atmospheric pressure flow reactor. (a) The sensor chip is positioned inside a resistive heating coil-wrapped quartz tube, which enables transmission-mode optical monitoring of the sensor under controlled temperature and gas environment at atmospheric pressure. The gas composition in the reactor is controlled with mass flow controllers (MFCs) as depicted in (b).

The Insplorion X1 flow reactor has the largest volume (effective volume  $\approx 190$  mL) of the systems I have used. I have mainly applied it for the sensor cross-sensitivity and poisoning test experiments included in **Paper II**, **III**, and **IV**. A schematic of the reactor is depicted in **Figure 28(a)**. The reactor itself is comprised of a quartz tube, which enables transmission-mode optical monitoring of the sensor chip mounted inside. The quartz tube is wrapped with a resistive heating coil. The temperature is controlled with a Eurotherm 3216 thermocontroller in a feedback-loop manner. In my case, the testing temperature was usually set to 30°C.

The gas mixture in the reactor is controlled using mass flow controllers (MFC, Bronkhorst EL-Flow Select series). The optical response is monitored and recorded using the Insplorer® software. The software employs 20<sup>th</sup> order polynomial fitting to calculate the sensor optical descriptors.

### 3. The Fiber Optic Feedthrough Reactor

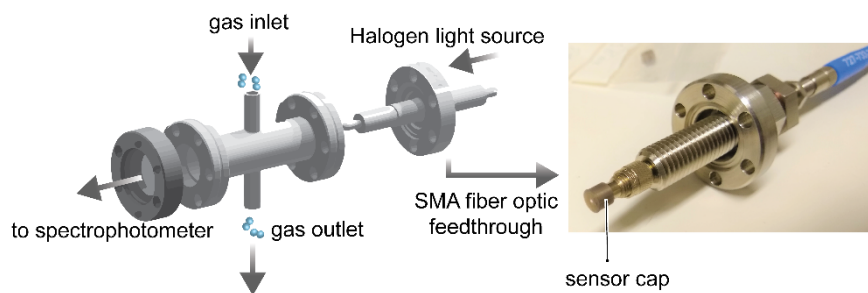


Figure 29: CAD-drawing of the fiber optic feedthrough reactor. Its key components are the fused-silica viewport and the SMA-type optical feedthrough. Inset: the 3D printed sensor cap is plugged on the inner tip of the optical feedthrough, which externally connects to an optical fiber that guides the light to the spectrophotometer.

The fiber optic feed-through reactor (effective volume  $\approx 15$  mL) was developed for the specific purpose of testing the 3D printed sensor caps presented in **Paper VI** and **Paper VII**. This reactor is equipped with an SMA fiber optic feedthrough (1.33" CF Flange, Accu-Glass) and a fused-silica viewport (1.33" CF Flange, Accu-Glass), as depicted in **Figure 29**. The 3D printed sensor cap is positioned on the feedthrough inner tip and the optical response is monitored in transmission mode through a fused-silica viewport using conventional fiber optics. The gas mixture is controlled by the MFC system depicted in **Figure 28(b)**.

## 4. Fast-Switch Mini Reactor

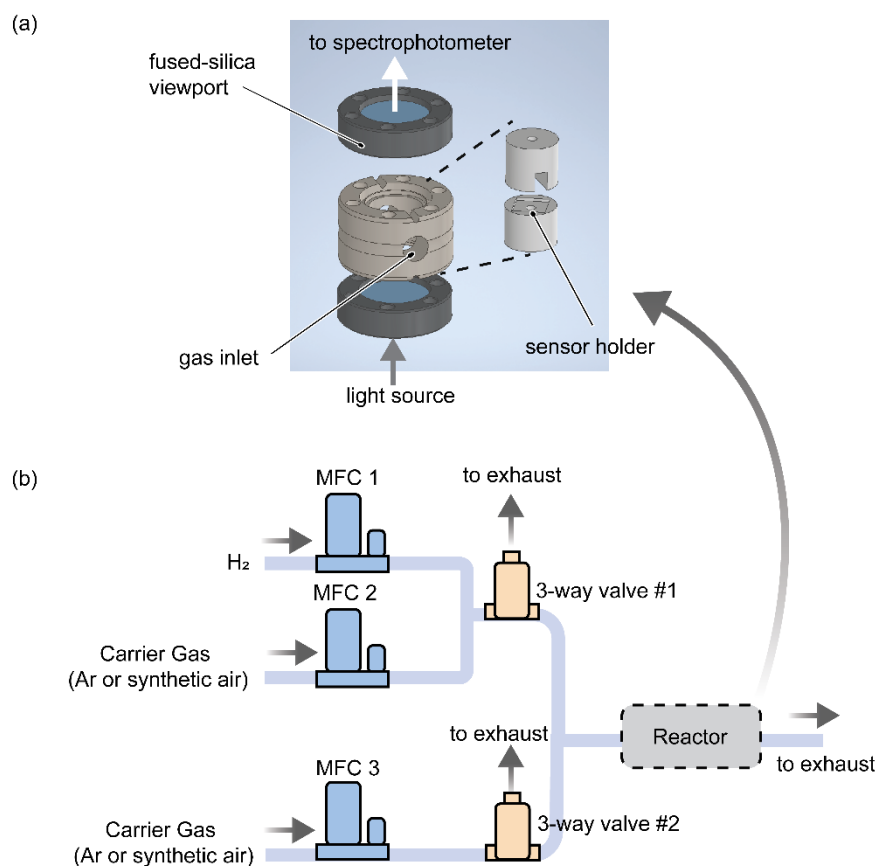


Figure 30: Schematic of the fast-switch mini reactor. (a) The reactor chamber was constructed from an off-the-shelf vacuum spacer equipped with a gas in- and outlet, sandwiched between two fused-silica viewports. The sensor holder is 3D printed out of PLA polymer. (b) The gas mixing and fast-switch system. A specific hydrogen concentration is prepared by mixing pure hydrogen and the selected carrier gas. The hydrogen-carrier gas mixture and the pure carrier gas entry to the reactor are regulated by two 3-way valves, which operate in a counterbalance manner.

A schematic drawing of the fast-switch mini reactor is presented in **Figure 30**. I have co-developed this reactor towards the very end of my thesis work and it has therefore not yet been used in the appended papers. Nevertheless, I think it is worth to discuss it shortly, to outline future opportunities, and to give some perspective on the sensor response and recovery time differences I have observed in my measurements using the other three setups described above, when comparing experiments in synthetic air carrier gas measured in X1 with measurements in pure hydrogen/vacuum.

To this end, we built the fast-switch mini reactor in an attempt to become able to measure ultrafast sensor response/recovery times in more realistic conditions than in the vacuum chamber I usually used. For this purpose, the fast-switch mini reactor chamber is comprised of a customized DN 16 CF spacer flange (Pfeifer Vacuum) equipped with a gas in- and outlet, and two fused-silica viewports (1.33" CF Flange, Accu-Glass). The sensor holder placed inside the chamber was 3D printed from polylactic acid (PLA) and serves the purpose of reducing the effective chamber volume to ca. 1.5 mL. Another distinct feature of this reactor is that it is



equipped with two units of three-way electronic switches (Peter Paul) connected to the diluted hydrogen supply and the synthetic air carrier gas, respectively, where they are operated in a counterbalance manner. Hence, in contrast to the Insplorion X1 flow reactor I have used for my work when assessing sensors in synthetic air, here the hydrogen – carrier gas mixture is prepared *before* it enters the reactor, thereby eliminating any gas mixing time factors from measurements of hydrogen sensor response times – a critical factor if ultrafast sensors are to be correctly characterized.<sup>247</sup>

Furthermore, thanks to its small volume and by using the maximum flow rate available to the system (2000 mL/min= 33.3 mL/s), the fast-switch reactors' gas-exchange time constant can be determined to:<sup>247</sup>

$$\tau = \frac{V}{v} = \frac{1.5 \text{ mL}}{33.3 \text{ mL/s}} = 45 \text{ ms}$$

where  $V$  is the reactor effective volume and  $v$  is the gas flow rate. In principle, an even lower time constant can be obtained by either reducing the reactor's effective volume or even further increasing the gas flow rate. This enables the assessment of sensor response times in the sub-second regime in simulated realistic (air) environments. At the same time, it highlights the importance of understanding that in flow-type reactors like the one at hand here, a measured sensor response will depend on the used gas flow rate, unless it is ensured that the system is operated in a regime where the flow rate is high enough that the gas exchange time constant is smaller than the intrinsic response time of the tested sensor.<sup>248</sup> Therefore, to investigate the optimum flow rate for a specific test, it is necessary to extract sensor signal onset times ( $\Delta t_{onset}$ ) for different H<sub>2</sub> flow rates. In the example included here, I used a 50  $\mu\text{m}$   $\times$  0.0035 wt.% Pd:Teflon H<sub>2</sub> sensor developed in **Paper VII** and performed the test at 25 °C using 100 vol.-% H<sub>2</sub> and flow rates ranging from 11 to 300 mL/min (**Figure 31(a)**). The correspondingly obtained  $\Delta t_{onset}$  vs. flow rate values are presented in **Figure 31(b)**, which shows that the onset time decreases exponentially with increasing flow rate and indicates that the onset time starts to level off at ~200 mL/min. This indicates that the instrument gas exchange time constant now is of the same order as the intrinsic sensor response time, which in turn means that a flow rate of at least 300 mL/min should be used to assess the true intrinsic kinetic response of the used 50  $\mu\text{m}$   $\times$  0.0035 wt.% Pd:Teflon H<sub>2</sub> sensor.

Finally, to give some perspective on H<sub>2</sub> sensor kinetics I previously have measured in the vacuum system and in synthetic air in the X1 flow reactor, I have tested the 190 nm  $\times$  25 nm Pd@PTFE/PMMA H<sub>2</sub> sensor I presented in **Paper IV** in the fast-switch mini flow reactor. In this case, I carried out the test by exposing the sensor to 80 mbar pure H<sub>2</sub> (vacuum chamber) and 8 vol.% H<sub>2</sub> in synthetic air (fast-switch reactor). As shown in **Figure 31(c)**, the sensor response is indeed somewhat slower in the flow-mode measurement in synthetic air than in vacuum but not dramatically. Furthermore, the similar response to the flow rate confirms that we are measuring the intrinsic response of the sensor. On the other hand, for the reverse situation of hydrogen desorption and sensor recovery, it appears that the sensor actually responds faster in synthetic air than in vacuum **Figure 31(b)**. In summary, these preliminary test results indicate that the fast response times I have measured using the vacuum setup for numerous sensor types in my thesis, also likely still are relevant when the sensors are operated in a real application situation in air.

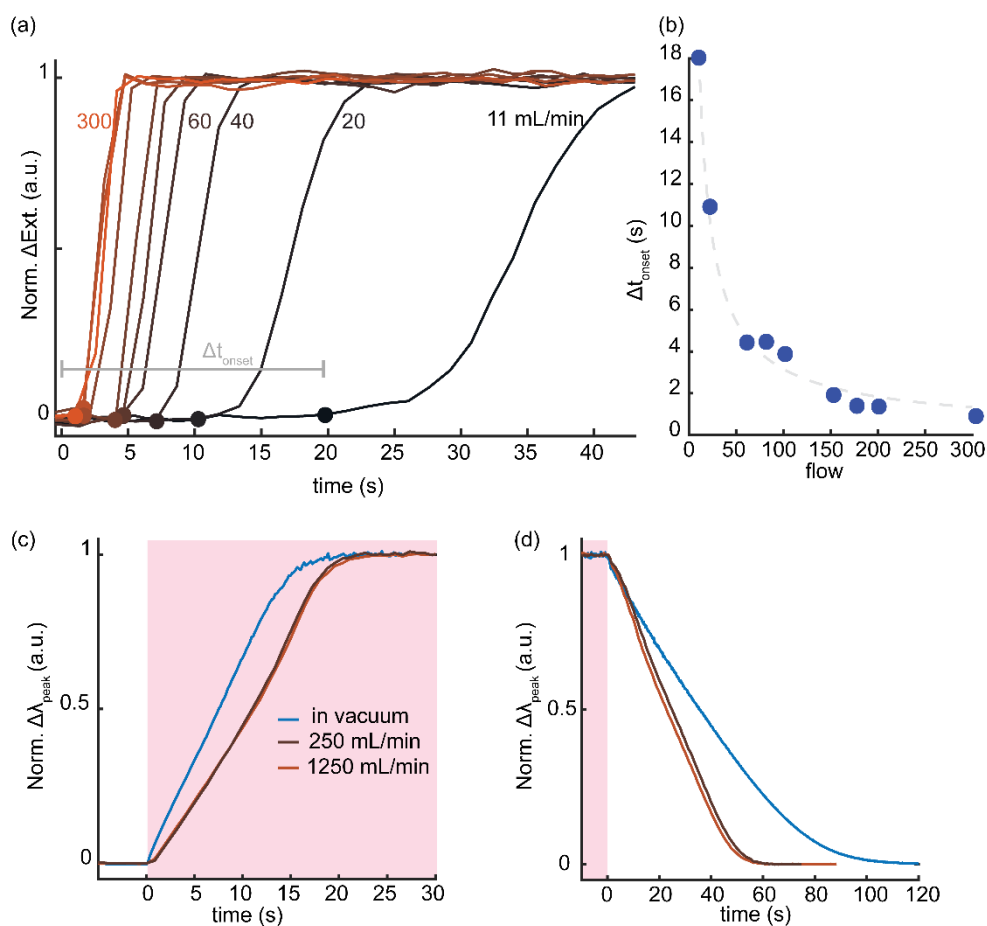


Figure 31: (a) Temporal optical  $\Delta\text{Ext}$  response of a  $50\ \mu\text{m} \times 0.0035\ \text{wt.}\%$  Pd:Teflon nanocomposite H<sub>2</sub> sensor to 100%-H<sub>2</sub> exposure in the fast-switch mini flow reactor at different flow rates: 11, 20, 40, 60, 80, 100, 150, 175, 200, and 300 mL/min. The synthetic air and 100%-H<sub>2</sub> valves were switched at  $t = 0$ . Onset time ( $\Delta t_{\text{onset}}$ ) is calculated from the time difference between the signal onset (signified by the dots) and  $t=0$ . (b)  $\Delta t_{\text{onset}}$  vs. flow rate obtained from (a). The test was done at 25°C. (c) Absorption and (d) desorption temporal  $\Delta\lambda_{\text{peak}}$  response of a  $190\ \text{nm} \times 25\ \text{nm}$  Pd@PTFE/PMMA sensor to 80 mbar H<sub>2</sub> (vacuum system) and 8 vol.% H<sub>2</sub> in synthetic air (fast-switch mini reactor). For the synthetic air background, two flow rates were tested: 250 and 1250 mL/min. The red shaded area denotes the H<sub>2</sub> exposure.



# Chapter 8 - Conclusion and Outlook

## 1. Conclusion

In this thesis, I have developed and demonstrated the utilization of nanoplasmonic-polymer hybrid or nanocomposite materials in an urgent energy-related application, namely hydrogen safety sensors. The nanoplasmonic Pd nanoparticles serve in this application as the active sensing material, while the polymer ameliorates some of the intrinsic shortcomings of Pd in hydrogen sensor applications. Specifically, it is acting as a filtering membrane that protects the Pd surface from poisoning/deactivating species and at the same time it enhances the sensing performance, i.e., it accelerates the response/recovery time via the reduction of the apparent hydrogen sorption activation energy and it improves sensitivity via a refractive index effect. In this way, the hybrid material concept developed in this thesis significantly advances hydrogen sensor technology with respect to: (i) ultrafast response/recovery time; (ii) hysteresis-free response; (iii) stability in poisoning/deactivation conditions. These advances were facilitated by optimizing both the Pd nanoparticles themselves by alloying and by tailoring their surface-to-volume ratio, and by rationally selecting appropriate polymer materials. Therefore, this thesis covers a broad spectrum of hydrogen sensor development, which ranges from fundamental studies to mechanistically unravel performance-limiting features, to application studies at simulated realistic conditions. This makes this thesis unique and sets it apart from most other hydrogen sensor studies, which either typically focus on the application side, without providing a clear insight about the fundamental mechanisms, or which investigate fundamental mechanisms without relating them to real application scenarios.

As the key findings, in the *first track*, **Paper I** laid the foundation for the hydrogen sensor development based on the nanoplasmonic effect by unravelling the correlation between the optical plasmonic response and the actual amount of hydrogen absorbed in Pd and PdAu and PdCu alloy nanoparticles. **Paper II** demonstrated the possibility to use PdCu alloys as a means to alleviate sensor deactivation in CO poisoning conditions and showed that hysteresis-free and CO-poisoning-free sensors can be obtained by ternary PdAuCu alloys. Moreover, **Paper III** discussed the systematic optimization of the alloyant composition to obtain the highest sensitivity, most efficient hysteresis suppression and highest CO poisoning resistance. **Paper IV** presented thin film polymer coatings as efficient and selective membranes to protect Pd from poisoning and deactivation. Furthermore, it demonstrated that polymer coatings improve hydrogen sorption kinetics and sensor limit of detection. **Paper V** discussed the impact of molecular stabilizers/surfactants on the hydrogen sorption kinetics of Pd nanoparticles, with the main finding that cationic surfactants decelerate the kinetics, while polymeric capping agents accelerate them.

Along the *second track* of this thesis, as a key result, we developed a scalable processing scheme to produce Pd plasmonic nanoparticle-polymer nanocomposite materials via colloidal synthesis of the Pd nanoparticles and melt-processing of the composite by mixing the matrix polymer material with the colloidal Pd nanoparticles. This nanocomposite material was then used as precursor for the production of filaments used to 3D print sensor caps compatible

with off-the-shelf fiber optics, and to melt-press a sensor plate used as transducer in a commercial plasmonic hydrogen sensor prototype device. In addition, we learnt that the response/recovery time of sensors made from this nanocomposite material is limited by the H<sub>2</sub> diffusion in the used PMMA polymer matrix (**Paper VI**). To alleviate this limitation, in **Paper VII**, we developed a nanocomposite using an amorphous fluorinated polymer matrix instead, since it has two orders higher H<sub>2</sub> permeability, and thereby succeeded with reducing the response time to the range of few seconds for a 3D printed hydrogen sensor. Similarly, to alleviate the hysteresis-problem of neat Pd nanoparticle signal transducers, in **Paper VIII**, we developed a colloidal synthesis route to produce hysteresis-free PdAu alloy nanoparticles that, as a future step, could be used in the bulk-processed nanocomposite material to obtain hysteresis-free response. Finally, in **Paper IX**, we have provided our perspective on the state-of-the-art in hydrogen safety sensor technology with focus on Pd-based solutions, and summarized strategies already available or strategies that still need to be further developed, to ultimately achieve high-performance Pd-based hydrogen sensors in par with the stringent performance targets defined by their stakeholders.

## 2. Next Steps

### 2.1. 2D sensors

Alloying Pd with Au increases the hydrogen sorption rate, as we have corroborated by identifying a correspondingly decreasing apparent activation energy. However, a question that remains to be answered is if the acceleration is caused only by the intrinsic PdAu ligand effect or if also the nanoparticle morphology in terms of grain structure is important. The latter since alloying induces strain/stress, which strongly correlates with the grain size<sup>249,250</sup> and influences the grain growth,<sup>251,252</sup> and since it is known that grain boundaries enable fast hydrogen diffusion.<sup>89,97,253</sup> Therefore, studies correlating nanoparticle grain structure with alloy composition and sorption kinetics are of high relevance.

In the surfactant effect study (**Paper V**), we found that cationic surfactants significantly decelerate the hydrogen ab/desorption rate. However, when colloiddally synthesizing Pd and Pd alloy nanoparticles, the use of cationic surfactants is often unavoidable due to their unmatched ability to produce well-defined particle shapes with well-defined facets. Therefore, one way to mitigate their detrimental effect on sorption kinetics could be to remove the surfactants from the nanoparticle surface, once they are implemented in the sensor. Therefore, finding an efficient, yet gentle, recipe to execute such “surface cleaning” is worthwhile to investigate.

When it comes to the polymer coating, I would suggest to further investigate the polymer film thickness effect on both hydrogen sorption time and the sensor selectivity, as well as on deactivation resistance. As I discussed in **Chapter 4**, reducing the thickness of a glassy polymer coating should improve the gas selectivity. Furthermore, I suggest to systematically study the correlation between the exact polymer chemistry and the apparent activation energy of hydrogen sorption since it is quite likely that the “kinetics acceleration effect” that we have

identified can be further enhanced with a polymer chemistry tailored for the purpose, by optimizing the bond between the polymer and the Pd surface.

Finally, the development of a hydrogen sensor able to operate in high-humidity remains a challenge unsolved to this day. Therefore, I suggest an attempt to find a solution to this challenge by combining appropriate Pd alloying with tailored polymer coatings.

## 2.2. 3D sensors

The Teflon matrix used in **Paper VII**, is among the most expensive polymer materials and its high price is therefore likely a factor that could hamper its large-scale application in hydrogen sensors. Therefore, I suggest the investigation of alternative amorphous polymers, with similar hydrogen permeabilities but with lower cost - for example Poly[1-(trimethylsilyl)-1-propyne] (PTMSP)<sup>254</sup> or polymers of intrinsic microporosity (PIM).<sup>255</sup> Similarly, the use of neat Pd colloidal nanoparticles for the nanocomposites developed in **Paper VI** and **Paper VII** obviously limits sensor performance due to hysteresis. A logical next step is therefore to use the colloidal PdAu nanoparticles developed in **Paper VIII** as component for a nanocomposite material that will enable hysteresis-free hydrogen sensing.

## 3. Outlook

The work presented in this thesis is a significant contribution to the advancement of hydrogen sensor technology, by pushing the nanoplasmonic hydrogen sensors closer to meeting industrial application requirements. Furthermore, it has identified a number of urgent, yet unsolved, limitations of high-performance Pd-based hydrogen sensors, like the lack of stability in high humidity. Therefore, I also hope that my work can serve as a “trigger” to the hydrogen sensor community to start addressing these issues. In the bigger picture, the progress in hydrogen safety sensors enabled by my work also contributes to hydrogen energy technology in general, and I am enthusiastic to see its imminent large-scale implementation in the coming couple of years.

Looking beyond the specific hydrogen sensor application, the plasmonic nanoparticle-polymer hybrid materials we have developed constitute a new platform for optical gas sensor development in general. A specific nanoplasmonic material can be used in combination with a selective polymer matrix to enable the selective detection of species like NO<sub>x</sub>, SO<sub>x</sub> or CO. Furthermore, the scalable processing scheme may inspire the development of other nanoplasmonics-based technologies, like plasmonic data recording/storage or photothermal materials, where fabrication cost is an important factor for the dissemination of the respective technology. Finally, the nanocomposite material concept developed may also be of interest for solid-state hydrogen storage or hydrogen purification applications.



## Acknowledgement

Time has just passed in the blink of an eye and now I am in the end of my PhD journey. I would say it is an amazing experience for both the sweet and bitter parts. All the accomplishments in this thesis should be seen as collective works from the wonderful individuals around me. For their support direct- and indirectly, I would like to thank these people.

First of all, I acknowledge The Swedish Foundation for Strategic Research Framework project RMA15-0052 for the financial support of this project. I hope this work fulfills the vision of the SSF.

I thank my supervisor Christoph Langhammer for everything. Your guidance and positive encouragement help me grow. I learnt a lot from you. Your work ethics and leadership are inspiring, and I will take those home. You are a great supervisor who sets high standard bar on research yet kind and open. I am grateful to be your graduate student.

My examiner and the head of Chemical Physics Division Henrik Grönbeck to make the division a nice working place. I really appreciate your sincere helps and discussions during my time in the division and thank you for your feedback to this thesis.

All members of the SSF Plastic Plasmonic project. All the PIs: Christian Müller (also my co-supervisor), Kasper-Moth Poulsen, Anders Hellman, and Paul Erhart. Young, smart, ambitious PIs but relax and humorous. I always learn new perspective from you. All the project foot-soldiers: Ida Östergren, Alicja Stolaś, Sarah Lerch, Robson Rosa da Silva, Amir M. Pourrahimi, Anja Lund, Lucy Cusinato, Magnus Rahm, Pernilla Tanner. I am proud to be in this great team.

My countrymen Ferry Nugroho who made my PhD started smoothly and always helped more than I asked. Your contribution to this thesis is enormous, I can't imagine to have achieved this much without all your support. *Sukses dan sampai jumpa di Indonesia.*

My Chalmers collaborators: Barbara Berke and Marianne Liebi for the assistance and patient discussions with the SAXS. You added a depth to this work. Vladimir Zhdanov for the theoretical analysis discussion, I am always impressed with your beautiful equations.

My external collaborators: Matteo Minelli (Bologna University), Manuel Guizar-Sicairos (PSI Switzerland), Olof Andersson (Insplorion), Herman Schreuders, Lars J. Bannenberg, Bernard Dam (Delft University of Technology), Alice B. da Silva Fanta, Shima Kadkhodazadeh, Jacob B. Wagner (TU Denmark). I appreciate all your long-distance assistance and discussion.

All Langhammer group members. Christopher Tiburski, Johan Tenghamn, David Tomecek, David Albinsson, Sara Nilsson, Joachim Fritzsche, Olga Serebrennikova, Ievgen Nedrygailov, Svetlana Alekseeva, Björn Altenburger, Ishara Fernando, Barbora Spackova, Jordi Piella-Bagaria. Former group members: Arturo Susarrey-Arce, Su Liu, Zafer Say, Stephan Bartling, Colin Murphy, Irem Tanyeli. Special thanks for Stephan and Ievgen who spent a lot of time to help me with my reactors set up. All of you are good people who are always there to offer helps and never say no. Outside work, I also had a good time with you guys, thanks for everything!



My former master student Sarah Z. Khairunissa for the contribution included in this thesis.

Lars Hellberg for all your assistance with all the technical aspects for my research. You never run out of solution when I come with technical issues or questions.

All members Chemical Physics for the support, *fika*, *snacka*, Chemical Physics kick-offs (sadly we have to skip one this year 😞) and your smiles in the corridor. All the seniors: Dinko, Björn, Anders, Igor who always welcome when I need helps and feedbacks. Lin Chen, Alvaro, Ying Xing, Gerard, Emma and everyone... for all the interesting chat about life and cultures. Thanks for sharing.

My office-mates in the only office-room where Chemical and Biological Physics people blend: Inna, Mokhtar, Irem, Silver, Quentin, David, Adrián, Barbora. Thanks for all the good stories and the laughter behind the door :-D.

Chalmers MC2 cleanroom staffs for the nanofabrication supports.

All components of Physics Department: the administration, workshop, operational staffs who work behind the stage but without them we cannot function. Lasse and Lennart for keeping the gas supply. Jan-Åke for the workshop assistance.

All the teachers of the courses I took with here at Chalmers. I enjoy GTS!

Our neighbor Biological Physics Division. I sometimes asked help from them and had good chats in our sharing pantry.

Living abroad has never been easy, I thank all my friends outside the academic life. Thanks for all your kindness, care and time. My friends in the Indonesian community: Adit, Nesia, Kurnia, Divie. My Chalmers and GU fellows Iqbaal, Maul, Alit, Faris, Victor, Rahmatdi, Sandoko, good luck with your works guys. And all friends I cannot mention one by one here.

Finally, I thank moral support, prayer and unconditional love from my family in Indonesia especially my mother, father, aunt, brothers, and sister. Love you all.

## References

1. Nanoeffects in Ancient Technology and Art and in Space. in *Fundamentals and Applications of Nano Silicon in Plasmonics and Fullerenes* 497–518 (Elsevier, 2018). doi:10.1016/b978-0-323-48057-4.00016-5
2. Mie, G. Beiträge zur Optik trüber Medien, speziell kolloidaler Metallösungen. *Ann. Phys.* **330**, 377–445 (1908).
3. Tong, L. *et al.* Recent Advances in Plasmonic Sensors. *Sensors* **14**, 7959–7973 (2014).
4. Anker, J. N. *et al.* Biosensing with plasmonic nanosensors. *Nat. Mater.* **7**, 442–453 (2008).
5. Atwater, H. A. & Polman, A. Plasmonics for improved photovoltaic devices. *Nat. Mater.* **9**, 205–213 (2010).
6. Sagle, L. B., Ruvuna, L. K., Ruemmele, J. a & Van Duyne, R. P. Advances in localized surface plasmon resonance spectroscopy biosensing. *Nanomedicine (Lond)*. **6**, 1447–62 (2011).
7. Brongersma, M. L., Halas, N. J. & Nordlander, P. Plasmon-induced hot carrier science and technology. *Nat. Nanotechnol.* **10**, 25–34 (2015).
8. Barnes, W. L. Particle plasmons: Why shape matters. *Am. J. Phys.* **84**, 593–601 (2016).
9. Jamkhande, P. G., Ghule, N. W., Bamer, A. H. & Kalaskar, M. G. Metal nanoparticles synthesis: An overview on methods of preparation, advantages and disadvantages, and applications. *Journal of Drug Delivery Science and Technology* **53**, 101174 (2019).
10. Willets, K. A., Duyne, R. Van & Van Duyne, R. P. Localized Surface Plasmon Resonance Spectroscopy and Sensing. *Annu. Rev. Phys. Chem.* **58**, 267–297 (2007).
11. Andrady, A. L. & Neal, M. A. Applications and societal benefits of plastics. *Philos. Trans. R. Soc. B Biol. Sci.* **364**, 1977–1984 (2009).
12. Thompson, R. C., Swan, S. H., Moore, C. J. & Vom Saal, F. S. Our plastic age. *Philosophical Transactions of the Royal Society B: Biological Sciences* **364**, 1973–1976 (2009).
13. Liz-Marzán, L. M. Tailoring surface plasmons through the morphology and assembly of metal nanoparticles. *Langmuir* **22**, 32–41 (2006).
14. Kelly, K. L., Coronado, E., Zhao, L. L. & Schatz, G. C. The Optical Properties of Metal Nanoparticles: The Influence of Size, Shape, and Dielectric Environment. *J. Phys. Chem. B* **107**, 668–677 (2003).
15. Song, J. *et al.* SERS-encoded nanogapped plasmonic nanoparticles: Growth of metallic nanoshell by templating redox-active polymer brushes. *J. Am. Chem. Soc.* **136**, 6838–6841 (2014).
16. Ghosh Chaudhuri, R. & Paria, S. Core/shell nanoparticles: Classes, properties, synthesis mechanisms, characterization, and applications. *Chemical Reviews* **112**, 2373–2433 (2012).

17. Sierra-Martin, B. & Fernandez-Barbero, A. Inorganic/polymer hybrid nanoparticles for sensing applications. *Advances in Colloid and Interface Science* **233**, 25–37 (2016).
18. Claes, N. *et al.* Characterization of silver-polymer core-shell nanoparticles using electron microscopy. *Nanoscale* **10**, 9186–9191 (2018).
19. Jeon, K. J. *et al.* Air-stable magnesium nanocomposites provide rapid and high-capacity hydrogen storage without using heavy-metal catalysts. *Nat. Mater.* **10**, 286–290 (2011).
20. Hanemann, T. & Szabó, D. V. Polymer-Nanoparticle Composites: From Synthesis to Modern Applications. *Materials (Basel)*. **3**, 3468–3517 (2010).
21. Thoniyot, P., Tan, M. J., Karim, A. A., Young, D. J. & Loh, X. J. Nanoparticle–Hydrogel Composites: Concept, Design, and Applications of These Promising, Multi-Functional Materials. *Advanced Science* **2**, (2015).
22. Pastoriza-Santos, I., Kinnear, C., Pérez-Juste, J., Mulvaney, P. & Liz-Marzán, L. M. Plasmonic polymer nanocomposites. *Nature Reviews Materials* **3**, 375–391 (2018).
23. No Title. Available at: [www.freepik.com](http://www.freepik.com).
24. Figueres, C. *The Future We Choose: Surviving the Climate Crisis by Christiana Figueres.* (Alfred A. Knoff, 2020).
25. Coral Bleaching During & Since the 2014-2017 Global Coral Bleaching Event Status and an Appeal for Observations. *National Environmental Satellite, Data, and Information Service (NESDIS)* Available at: [https://coralreefwatch.noaa.gov/satellite/analyses\\_guidance/global\\_coral\\_bleaching\\_2014-17\\_status.php](https://coralreefwatch.noaa.gov/satellite/analyses_guidance/global_coral_bleaching_2014-17_status.php). (Accessed: 21st October 2020)
26. Great Barrier Reef experiences massive coral bleaching. *Science* Available at: <https://www.sciencemag.org/news/2020/04/great-barrier-reef-experiences-massive-coral-bleaching>. (Accessed: 21st October 2020)
27. Masson-Delmotte, V. *et al.* *Global warming of 1.5°C.* (2019).
28. Züttel, A., Remhof, A., Borgschulte, A. & Friedrichs, O. Hydrogen: the future energy carrier. *Philos. Trans. R. Soc. A Math. Phys. Eng. Sci.* **368**, 3329–3342 (2010).
29. Crabtree, G. W., Dresselhaus, M. S. & Buchanan, M. V. The Hydrogen Economy. *Phys. Today Appl. Phys. Lett. Appl. Phys. Lett.* **57**, (2004).
30. Morgan, T. The hydrogen economy - A non-technical Review. *United Nations Environment Programme* (2006). Available at: [www.unep.fr/energy/](http://www.unep.fr/energy/). (Accessed: 17th May 2017)
31. Här är de SSF-ARC-center som får dela på 200 miljoner kronor. (2020). Available at: <https://strategiska.se/pressmeddelande/har-ar-de-ssf-arc-center-som-far-dela-pa-200-miljoner-kronor/>. (Accessed: 13th October 2020)
32. Hübert, T., Boon-Brett, L., Black, G. & Banach, U. Hydrogen sensors - A review. *Sensors Actuators, B Chem.* **157**, 329–352 (2011).
33. Hübert, T., Boon-Brett, L., Palmisano, V. & Bader, M. A. Developments in gas sensor

- technology for hydrogen safety. in *International Journal of Hydrogen Energy* **39**, 20474–20483 (Pergamon, 2014).
34. Lower and Upper Explosive Limits for Flammable Gases and Vapors (LEL/UEL). Available at: [https://www.mathesongas.com/pdfs/products/Lower-\(LEL\)-&-Upper-\(UEL\)-Explosive-Limits-.pdf](https://www.mathesongas.com/pdfs/products/Lower-(LEL)-&-Upper-(UEL)-Explosive-Limits-.pdf). (Accessed: 1st December 2020)
  35. Kumamoto, A., Iseki, H., Ono, R. & Oda, T. Measurement of minimum ignition energy in hydrogen-oxygen-nitrogen premixed gas by spark discharge. in *Journal of Physics: Conference Series* **301**, 12039 (Institute of Physics Publishing, 2011).
  36. Randall, C. Norway: Explosion at hydrogen filling station. *electrive.com* (2019). Available at: <https://www.electrive.com/2019/06/11/norway-explosion-at-fuel-cell-filling-station/>. (Accessed: 21st October 2020)
  37. Hampel, C. Cause found for fire at H2 refilling station in Norway. *Electrive.Com* (2019). Available at: <https://www.electrive.com/2019/07/01/cause-found-explosion-at-h2-refuelling-station-in-norway/>. (Accessed: 21st October 2020)
  38. Boon-Brett, L. *et al.* Identifying performance gaps in hydrogen safety sensor technology for automotive and stationary applications. *Int. J. Hydrogen Energy* **35**, 373–384 (2010).
  39. Buttner, W., Burgess, R. M., Post, M. & Rivkin, C. *Summary and Findings from the NREL/DOE Hydrogen Sensor Workshop (June 8, 2011)*. (2011).
  40. Clerbaux, C. *et al.* Carbon monoxide pollution from cities and urban areas observed by the Terra/MOPITT mission. *Geophys. Res. Lett.* **35**, L03817 (2008).
  41. Jimenez, G. *et al.* A Comparative Assessment of Hydrogen Embrittlement: Palladium and Palladium-Silver (25 Weight% Silver) Subjected to Hydrogen Absorption/Desorption Cycling. *Adv. Chem. Eng. Sci.* **06**, 246–261 (2016).
  42. Volkov, A. Y., Novikova, O. S., Kostina, A. E. & Antonov, B. D. Effect of alloying with palladium on the electrical and mechanical properties of copper. *Phys. Met. Metallogr.* **117**, 945–954 (2016).
  43. Nam, S.-E., Seong, Y.-K., Lee, J. W. & Lee, K.-H. Preparation of highly stable palladium alloy composite membranes for hydrogen separation. *Desalination* **236**, 51–55 (2009).
  44. Noh, H., Flanagan, T. B., Gavra, Z., Johnson, J. R. & Reilly, J. J. The disappearance of hysteresis for the hydride phase transition in palladium-nickel alloys. *Scr. Metall. Mater.* **25**, 2177–2180 (1991).
  45. Luo, S., Wang, D. & Flanagan, T. B. Thermodynamics of Hydrogen in fcc *Pd–Au Alloys*. *J. Phys. Chem. B* **114**, 6117–6125 (2010).
  46. Isaac, N. A. *et al.* Optical hydrogen sensing with nanoparticulate Pd–Au films produced by spark ablation. *Sensors Actuators B Chem.* **221**, 290–296 (2015).
  47. Westerwaal, R. J. *et al.* Thin film based sensors for a continuous monitoring of hydrogen concentrations. *Sensors Actuators B Chem.* **165**, 88–96 (2012).
  48. Favier, F., Walter, E. C., Zach, M. P., Benter, T. & Penner, R. M. Hydrogen sensors and

- switches from electrodeposited palladium mesowire arrays. *Science* (80-. ). **293**, 2227–2231 (2001).
49. Walter, E. C., Favier, F. & Penner, R. M. Palladium mesowire arrays for fast hydrogen sensors and hydrogen-actuated switches. *Anal. Chem.* **74**, 1546–1553 (2002).
  50. Lee, J. S., Kim, S. G., Cho, S. & Jang, J. Porous palladium coated conducting polymer nanoparticles for ultrasensitive hydrogen sensors. *Nanoscale* **7**, 20665–20673 (2015).
  51. Kim, S. M. *et al.* High-Performance, Transparent Thin Film Hydrogen Gas Sensor Using 2D Electron Gas at Interface of Oxide Thin Film Heterostructure Grown by Atomic Layer Deposition. *Adv. Funct. Mater.* **29**, 1807760 (2018).
  52. Graunke, T., Schmitt, K., Raible, S. & Wöllenstein, J. Towards enhanced gas sensor performance with fluoropolymer membranes. *Sensors (Switzerland)* **16**, (2016).
  53. Chen, M. *et al.* Response Characteristics of Hydrogen Sensors Based on PMMA-Membrane-Coated Palladium Nanoparticle Films. *ACS Appl. Mater. Interfaces* **9**, 27193–27201 (2017).
  54. Hong, J. *et al.* A Highly Sensitive Hydrogen Sensor with Gas Selectivity Using a PMMA Membrane-Coated Pd Nanoparticle/Single-Layer Graphene Hybrid. *ACS Appl. Mater. Interfaces* **7**, 3554–3561 (2015).
  55. Fredriksson, H. *et al.* Hole-mask colloidal lithography. *Adv. Mater.* **19**, 4297–4302 (2007).
  56. Fredriksson, H. *et al.* Hole-Mask Colloidal Lithography. *Adv. Mater.* **19**, 4297–4302 (2007).
  57. Wadell, C. *et al.* Hysteresis-Free Nanoplasmonic Pd-Au Alloy Hydrogen Sensors. *Nano Lett.* **15**, 3563–3570 (2015).
  58. Cottington, I. E. “Palladium; or, New Silver”. *Platin. Met. Rev.* **35**, 141 (1991).
  59. Adams, B. D. & Chen, A. The role of palladium in a hydrogen economy. *Mater. Today* **14**, 282–289 (2011).
  60. Behm, R. J., Penka, V., Cattania, M. G., Christmann, K. & Ertl, G. Evidence for ‘subsurface’ hydrogen on Pd(110): An intermediate between chemisorbed and dissolved species. *J. Chem. Phys.* **78**, 7486–7490 (1982).
  61. Knapton, A. G. Palladium Alloys for Hydrogen Diffusion Membranes. *Platin. Met. Rev.* **21**, 44–50 (1977).
  62. Schneemann, A. *et al.* Nanostructured Metal Hydrides for Hydrogen Storage. *Chemical Reviews* **118**, 10775–10839 (2018).
  63. Ohno, S., Wilde, M. & Fukutani, K. Novel insight into the hydrogen absorption mechanism at the Pd(110) surface. *J. Chem. Phys.* **140**, 134705 (2014).
  64. Auer, W. & Grabke, H. J. The Kinetics of Hydrogen Absorption in Palladium ( $\alpha$ - and  $\beta$ -phase) and Palladium-Silver-Alloys. *Berichte der Bunsengesellschaft für Phys. Chemie* **78**, 58–67 (1974).

65. Johansson, M. *et al.* Hydrogen adsorption on palladium and palladium hydride at 1bar. *Surf. Sci.* **604**, 718–729 (2010).
66. Goto, K., Hirata, T., Yamamoto, I. & Nakao, W. Swelling response behavior of palladium during hydrogen absorption and discharge. *Int. J. Hydrogen Energy* **43**, 11092–11099 (2018).
67. Caravella, A., Scura, F., Barbieri, G. & Drioli, E. Sieverts law empirical exponent for PD-based membranes: Critical analysis in pure H<sub>2</sub> permeation. *J. Phys. Chem. B* **114**, 6033–6047 (2010).
68. Ono *et al.* A Heterothermic Kinetic Model of Hydrogen Absorption in Metals with Subsurface Transport. *Metals (Basel)*. **9**, 1131 (2019).
69. Conrad, H., Ertl, G. & Latta, E. E. Adsorption of hydrogen on palladium single crystal surfaces. *Surf. Sci.* **41**, 435–446 (1974).
70. He, J. W., Harrington, D. A., Griffiths, K. & Norton, P. R. The interaction of hydrogen with a Pd(100) surface. *Surf. Sci.* **198**, 413–430 (1988).
71. Jewell, L. L. & Davis, B. H. Review of absorption and adsorption in the hydrogen-palladium system. *Applied Catalysis A: General* **310**, 1–15 (2006).
72. Ramos De Debiaggi, S. *et al.* Hydrogen absorption in Pd thin-films. in *International Journal of Hydrogen Energy* **39**, 8590–8595 (Elsevier Ltd, 2014).
73. Xu, D. *et al.* Ultrathin palladium nanosheets with selectively controlled surface facets. *Chem. Sci.* **9**, 4451–4455 (2018).
74. Delmelle, R. & Proost, J. An in situ study of the hydriding kinetics of Pd thin films. in *Physical Chemistry Chemical Physics* **13**, 11412–11421 (Royal Society of Chemistry, 2011).
75. Manchester, F. D., San-Martin, A. & Pitre, J. M. The H-Pd (hydrogen-palladium) System. *J. Phase Equilibria* **15**, 62–83 (1994).
76. Jang, B., Lee, K. Y., Noh, J. S. & Lee, W. Nanogap-based electrical hydrogen sensors fabricated from Pd-PMMA hybrid thin films. *Sensors Actuators, B Chem.* **193**, 530–535 (2014).
77. McKeown, S. J., Wang, X., Yu, X. & Goddard, L. L. Realization of palladium-based optomechanical cantilever hydrogen sensor. *Microsystems Nanoeng.* **3**, 16087 (2017).
78. Kumar, S. & Balasubramaniam, R. Theoretical analysis of hysteresis during hydrogen transformations in the vanadium-hydrogen system. *Int. J. Hydrogen Energy* **20**, 211–220 (1995).
79. Moorthy, A. Theoretical and Experimental Study of Pressure Hysteresis in the Palladium Hydride Phase Transformation. (California Institute of Technology, 2018).
80. Hayee, F. *et al.* In-situ visualization of solute-driven phase coexistence within individual nanorods. *Nat. Commun.* **9**, 1775 (2018).
81. Baldi, A., Narayan, T. C., Koh, A. L. & Dionne, J. A. In situ detection of hydrogen-induced phase transitions in individual palladium nanocrystals. *Nat. Mater.* **13**, 1143–

- 1148 (2014).
82. Syrenova, S. *et al.* Hydride formation thermodynamics and hysteresis in individual Pd nanocrystals with different size and shape. *Nat. Mater.* **14**, 1236–1244 (2015).
  83. Schwarz, R. B., Khachatryan, A. K., Caro, A., Baskes, M. I. & Martinez, E. Coherent phase decomposition in the Pd–H system. *J. Mater. Sci.* **55**, 4864–4882 (2020).
  84. Schwarz, R. B. & Khachatryan, A. G. Thermodynamics of open two-phase systems with coherent interfaces: Application to metal–hydrogen systems. *Acta Mater.* **54**, 313–323 (2006).
  85. Fisser, M., Badcock, R. A., Teal, P. D. & Hunze, A. Optimizing the sensitivity of palladium based hydrogen sensors. *Sensors Actuators, B Chem.* **259**, 10–19 (2018).
  86. Nugroho, F. A. A. *et al.* Metal–polymer hybrid nanomaterials for plasmonic ultrafast hydrogen detection. *Nat. Mater.* **18**, (2019).
  87. Langhammer, C., Zhdanov, V. P., Zorić, I. & Kasemo, B. Size-dependent hysteresis in the formation and decomposition of hydride in metal nanoparticles. *Chem. Phys. Lett.* **488**, 62–66 (2010).
  88. Johnson, N. J. J. *et al.* Facets and vertices regulate hydrogen uptake and release in palladium nanocrystals. *Nat. Mater.* **18**, 454–458 (2019).
  89. Delmelle, R. *et al.* Effect of structural defects on the hydriding kinetics of nanocrystalline Pd thin films. *Int. J. Hydrogen Energy* **40**, 7335–7347 (2015).
  90. Langhammer, C., Zhdanov, V. P., Zorić, I. & Kasemo, B. Size-Dependent Kinetics of Hydriding and Dehydriding of Pd Nanoparticles. *Phys. Rev. Lett.* **104**, 135502 (2010).
  91. Yamauchi, M., Ikeda, R., Kitagawa, H. & Takata, M. Nanosize Effects on Hydrogen Storage in Palladium. (2008). doi:10.1021/JP710447J
  92. Pundt, A. *et al.* Hydrogen and Pd-clusters. *Mater. Sci. Eng. B* **108**, 19–23 (2004).
  93. Langhammer, C., Zhdanov, V. P., Zorić, I. & Kasemo, B. Size-dependent hysteresis in the formation and decomposition of hydride in metal nanoparticles. *Chem. Phys. Lett.* **488**, 62–66 (2010).
  94. Narayan, T. C. *et al.* Direct visualization of hydrogen absorption dynamics in individual palladium nanoparticles. *Nat. Commun.* **8**, 14020 (2017).
  95. Suzana, A. F. *et al.* Structure and dynamics of a single palladium nanoparticle in the hydride phase transformation revealed by X-ray imaging.
  96. Li, G. *et al.* Shape-dependent hydrogen-storage properties in Pd nanocrystals: Which does hydrogen prefer, octahedron (111) or cube (100)? *J. Am. Chem. Soc.* **136**, 10222–10225 (2014).
  97. Iwaoka, H., Arita, M. & Horita, Z. Hydrogen diffusion in ultrafine-grained palladium: Roles of dislocations and grain boundaries. *Acta Mater.* **107**, 168–177 (2016).
  98. Yau, A., Harder, R. J., Kanan, M. W. & Ulvestad, A. Imaging the Hydrogen Absorption

- Dynamics of Individual Grains in Polycrystalline Palladium Thin Films in 3D. *ACS Nano* **11**, 10945–10954 (2017).
99. Stuhr, U. *et al.* An investigation of hydrogen diffusion in nanocrystalline Pd by neutron spectroscopy. *J. Alloys Compd.* **253–254**, 393–396 (1997).
  100. Kirchheim, R. Hydrogen solubility and diffusivity in defective and amorphous metals. *Progress in Materials Science* **32**, 261–325 (1988).
  101. Janßen, S. *et al.* Hydrogen diffusion in nanocrystalline Pd by means of quasielastic neutron scattering. *Nanostructured Mater.* **9**, 579–582 (1997).
  102. Johnson, N. J. J., Lam, B., Sherbo, R. S., Fork, D. K. & Berlinguette, C. P. Ligands Affect Hydrogen Absorption and Desorption by Palladium Nanoparticles. *Chem. Mater.* **31**, 8679–8684 (2019).
  103. Ford, R. R. Carbon Monoxide Adsorption on the Transition Metals. *Adv. Catal.* **21**, 51–150 (1970).
  104. Bradshaw, A. M. The structure and chemistry of adsorbed carbon monoxide. *Surf. Sci.* **80**, 215–225 (1979).
  105. Sung, S. S. & Hoffmann, R. How Carbon Monoxide Bonds to Metal Surfaces. *J. Am. Chem. Soc.* **107**, 578–584 (1985).
  106. Amandusson, H., Ekedahl, L. G. & Dannetun, H. Effect of CO and O<sub>2</sub> on hydrogen permeation through a palladium membrane. *Appl. Surf. Sci.* **153**, 259–267 (2000).
  107. O'Brien, C. P. & Lee, I. C. CO Poisoning and CO Hydrogenation on the Surface of Pd Hydrogen Separation Membranes. *J. Phys. Chem. C* **121**, 16864–16871 (2017).
  108. Ruppel, G., Morkel, M., Freund, H. J. & Hirschl, R. Sum frequency generation and density functional studies of CO-H interaction and hydrogen bulk dissolution on Pd(111). *Surf. Sci.* **554**, 43–59 (2004).
  109. Fonseca, S., Maia, G. & Pinto, L. M. C. Hydrogen adsorption in the presence of coadsorbed CO on Pd(111). *Electrochem. commun.* **93**, 100–103 (2018).
  110. Wong, Y. T. & Hoffmann, R. Chemisorption of carbon monoxide on three metal surfaces: Ni(111), Pd(111), and Pt(111). A comparative study. *J. Phys. Chem.* **95**, 859–867 (1991).
  111. Uvdal, P., Karlsson, P. A., Nyberg, C., Andersson, S. & Richardson, N. V. On the structure of dense CO overlayers. *Surf. Sci.* **202**, 167–182 (1988).
  112. Yudanov, I. V *et al.* CO Adsorption on Pd Nanoparticles: Density Functional and Vibrational Spectroscopy Studies. (2003). doi:10.1021/jp022052b
  113. Lopez, N., Łodziana, Z., Illas, F. & Salmeron, M. When langmuir is too simple: H<sub>2</sub> dissociation on Pd(111) at high coverage. *Phys. Rev. Lett.* **93**, 146103 (2004).
  114. Mitsu, T., Rose, M. K., Fomin, E., Ogletree, D. F. & Salmeron, M. Dissociative hydrogen adsorption on palladium requires aggregates of three or more vacancies. *Nature* **422**, 705–707 (2003).



115. O'Brien, C. P. & Lee, I. C. The interaction of CO with PdCu hydrogen separation membranes: An operando infrared spectroscopy study. *Catal. Today* (2017). doi:10.1016/j.cattod.2017.09.039
116. Debauge, Y., Abon, M., Bertolini, J. C., Massardier, J. & Rochefort, A. Synergistic alloying behaviour of Pd50Cu50 single crystals upon adsorption and co-adsorption of CO and NO. *Appl. Surf. Sci.* **90**, 15–27 (1995).
117. Rochefort, A. & Fournier, R. Quantum Chemical Study of CO and NO Bonding to Pd<sub>2</sub>, Cu<sub>2</sub>, and PdCu. *J. Phys. Chem.* **100**, 13506–13513 (1996).
118. Illas, F. *et al.* Interaction of CO and NO with PdCu(111) Surfaces. *J. Phys. Chem. B* **102**, 8017–8023 (1998).
119. Sakong, S., Mosch, C. & Groß, A. CO adsorption on Cu-Pd alloy surfaces: Ligand versus ensemble effects. *Phys. Chem. Chem. Phys.* **9**, 2216–2225 (2007).
120. Ma, Y., Diemant, T., Bansmann, J. & Behm, R. J. The interaction of CO with PdAg/Pd(111) surface alloys - A case study of ensemble effects on a bimetallic surface. *Phys. Chem. Chem. Phys.* **13**, 10741–10754 (2011).
121. Tan, Q. *et al.* Highly Dispersed Pd-CeO<sub>2</sub> Nanoparticles Supported on N-Doped Core-Shell Structured Mesoporous Carbon for Methanol Oxidation in Alkaline Media. *ACS Catal.* **9**, 6362–6371 (2019).
122. Xu, F., Xu, R. & Mu, S. Enhanced SO<sub>2</sub> and CO poisoning resistance of CeO<sub>2</sub> modified Pt/C catalysts applied in PEM fuel cells. *Electrochim. Acta* **112**, 304–309 (2013).
123. Tang, Q., Mao, Z., Ma, S. & Huang, K. Enhanced methanol oxidation and CO tolerance using CeO<sub>2</sub>-added eggshell membrane-templated Pd network electrocatalyst. *RSC Adv.* **2**, 11465–11471 (2012).
124. Allison, E. G. & Bond, G. C. The Structure and Catalytic Properties of Palladium-Silver and Palladium-Gold Alloys. *Catal. Rev.* **7**, 233–289 (1972).
125. Okamoto, H. & Massalski, T. B. The Au-Pd (Gold-Palladium) system. *Bull. Alloy Phase Diagrams* **6**, 229–235 (1985).
126. Burch, R. & Buss, R. G. Absorption of hydrogen by palladium-copper alloys. Part 1.— Experimental measurements. *J. Chem. Soc. Faraday Trans. 1 Phys. Chem. Condens. Phases* **71**, 913 (1975).
127. Subramanian, P. . & Laughlin, D. . Cu-Pd (Copper-Palladium). *J. Phase Equilibria* **12**, 231–243 (1991).
128. Kamakoti, P. *et al.* Prediction of hydrogen flux through sulfur-tolerant binary alloy membranes. *Science* **307**, 569–73 (2005).
129. Zhang, K. & Way, J. D. Palladium-copper membranes for hydrogen separation. *Sep. Purif. Technol.* **186**, 39–44 (2017).
130. Piper, J. Diffusion of hydrogen in copper-palladium alloys. *J. Appl. Phys.* **37**, 715–721 (1966).

131. Tang, J. *et al.* Mass transport in the PdCu phase structures during hydrogen adsorption and absorption studied by XPS under hydrogen atmosphere. *Appl. Surf. Sci.* **480**, 419–426 (2019).
132. Liu, L. C., Gong, H. R., Zhou, S. F. & Gong, X. Adsorption, diffusion, and permeation of hydrogen at PdCu surfaces. *J. Memb. Sci.* **588**, 117206 (2019).
133. Sakamoto, Y., Ishimaru, N. & Mukai, Y. Thermodynamics of Solution of Hydrogen in Pd-Cu and Pd-Cu-Au Solid Solution Alloys. *Berichte der Bunsengesellschaft für Phys. Chemie* **95**, 680–688 (1991).
134. Honrado Guerreiro, B., Martin, M. H., Roué, L. & Guay, D. Hydrogen Solubility of Magnetron Co-Sputtered FCC and BCC PdCuAu Thin Films. *J. Phys. Chem. C* **120**, 5297–5307 (2016).
135. Galipaud, J., Martin, M. H., Roué, L. & Guay, D. Pulsed Laser Deposition of PdCuAu Alloy Membranes for Hydrogen Absorption Study. *J. Phys. Chem. C* **119**, 26451–26458 (2015).
136. Jia, H. *et al.* High-temperature stability of Pd alloy membranes containing Cu and Au. *J. Memb. Sci.* **544**, 151–160 (2017).
137. Guerreiro, B. M. H. Palladium-Copper-Gold Alloys for the Separation of Hydrogen Gas. *Doctoral Thesis* (Université du Québec, 2015).
138. Namba, K. *et al.* Acceleration of hydrogen absorption by palladium through surface alloying with gold. *Proc. Natl. Acad. Sci. U. S. A.* **115**, 7896–7900 (2018).
139. OBrien, C. P., Miller, J. B., Morreale, B. D. & Gellman, A. J. The kinetics of H 2-D 2 exchange over Pd, Cu, and PdCu surfaces. *J. Phys. Chem. C* **115**, 24221–24230 (2011).
140. Namba, K. *et al.* Acceleration of hydrogen absorption by palladium through surface alloying with gold. *Proc. Natl. Acad. Sci.* **115**, 201800412 (2018).
141. Nugroho, F. A. A., Eklund, R., Nilsson, S. & Langhammer, C. A fiber-optic nanoplasmonic hydrogen sensor via pattern-transfer of nanofabricated PdAu alloy nanostructures. *Nanoscale* **10**, 20533–20539 (2018).
142. Westerwaal, R. J. *et al.* Nanostructured Pd–Au based fiber optic sensors for probing hydrogen concentrations in gas mixtures. *Int. J. Hydrogen Energy* **38**, 4201–4212 (2013).
143. Burch, R. & Buss, R. G. Absorption of hydrogen by palladium–copper alloys. Part 2.—Theoretical analysis. *J. Chem. Soc. Faraday Trans. 1 Phys. Chem. Condens. Phases* **71**, 922 (1975).
144. Hayashi, Y., Yamazaki, H., Ono, D., Masunishi, K. & Ikehashi, T. Investigation of PdCuSi metallic glass film for hysteresis-free and fast response capacitive MEMS hydrogen sensors. *Int. J. Hydrogen Energy* **43**, 9438–9445 (2018).
145. Løvvik, O. M. Surface segregation in palladium based alloys from density-functional calculations. *Surf. Sci.* **583**, 100–106 (2005).
146. Zhao, M., Sloof, W. G. & Böttger, A. J. Modelling of surface segregation for palladium

- alloys in vacuum and gas environments. *Int. J. Hydrogen Energy* **43**, 2212–2223 (2018).
147. Okube, M. *et al.* Topologically sensitive surface segregations of Au-Pd alloys in electrocatalytic hydrogen evolution. *ChemElectroChem* **1**, 207–212 (2014).
  148. Mezey, L. Z., Hofer, W., Varga, P. & Giber, J. The drastic effect of oxygen on surface segregation. *Surf. Interface Anal.* **16**, 520–525 (1990).
  149. Kim, H. Y. & Henkelman, G. CO adsorption-driven surface segregation of Pd on Au/Pd bimetallic surfaces: Role of defects and effect on CO oxidation. *ACS Catal.* **3**, 2541–2546 (2013).
  150. Soto-Verdugo, V. & Metiu, H. Segregation at the surface of an Au/Pd alloy exposed to CO. *Surf. Sci.* **601**, 5332–5339 (2007).
  151. Dekura, S., Kobayashi, H., Kusada, K. & Kitagawa, H. Hydrogen in Palladium and Storage Properties of Related Nanomaterials: Size, Shape, Alloying, and Metal-Organic Framework Coating Effects. *ChemPhysChem* **20**, 1158–1176 (2019).
  152. Palm, K. J., Murray, J. B., Narayan, T. C. & Munday, J. N. Dynamic Optical Properties of Metal Hydrides. *ACS Photonics* **5**, 4677–4686 (2018).
  153. Silkin, V. M., Díez Muiño, R., Chernov, I. P., Chulkov, E. V & Echenique, P. M. Tuning the plasmon energy of palladium–hydrogen systems by varying the hydrogen concentration. *J. Phys. Condens. Matter* **24**, 104021 (2012).
  154. El Matbouly, H. *et al.* Assessment of commercial micro-machined hydrogen sensors performance metrics for safety sensing applications. *Int. J. Hydrogen Energy* **39**, 4664–4673 (2014).
  155. Gremaud, R. *et al.* Hydrogenography: An optical combinatorial method to find new light-weight hydrogen-storage materials. *Adv. Mater.* **19**, 2813–2817 (2007).
  156. ElKabbash, M. *et al.* Hydrogen Sensing Using Thin-Film Perfect Light Absorber. *ACS Photonics* **6**, 1889–1894 (2019).
  157. Schreuders, H., Radeva, T., Ngene, P., Westerwaal, R. & Dam, B. Eye readable metal hydride based hydrogen tape sensor for health applications. in *Photonics Applications for Aviation, Aerospace, Commercial, and Harsh Environments V* (eds. Kazemi, A. A., Kress, B. C. & Mendoza, E. A.) **9202**, 920203 (International Society for Optics and Photonics, 2014).
  158. Zhang, Y. *et al.* Recent advancements in optical fiber hydrogen sensors. *Sensors Actuators B Chem.* **244**, 393–416 (2017).
  159. Langhammer, C., Zorić, I., Larsson, E. M. & Kasemo, B. Localized surface plasmons shed light on nanoscale metal hydrides. *Adv. Mater.* **22**, 4628–4633 (2010).
  160. Wadell, C., Syrenova, S. & Langhammer, C. Plasmonic Hydrogen Sensing with Nanostructured Metal Hydrides. **12**, 28 (2020).
  161. Mayer, K. M. & Hafner, J. H. Localized Surface Plasmon Resonance Sensors. *Chem. Rev.* **111**, 3828–3857 (2011).

162. Lee, K.-S. & El-Sayed, M. A. Gold and Silver Nanoparticles in Sensing and Imaging: Sensitivity of Plasmon Response to Size, Shape, and Metal Composition. *J. Phys. Chem. B* **110**, 19220–19225 (2006).
163. Langhammer, C., Yuan, Z., Zorić, I. & Kasemo, B. Plasmonic Properties of Supported Pt and Pd Nanostructures. *Nano Lett.* **6**, 833–838 (2006).
164. Hao, E. & Schatz, G. C. Electromagnetic fields around silver nanoparticles and dimers. *J. Chem. Phys.* **120**, 357–366 (2004).
165. Hu, J. *et al.* Surface plasmon resonance in periodic hexagonal lattice arrays of silver nanodisks. *J. Nanomater.* **2013**, 1–7 (2013).
166. Maier, S. A. *Plasmonics: Fundamentals and applications. Plasmonics: Fundamentals and Applications* (Springer US, 2007). doi:10.1007/0-387-37825-1
167. Shahbazyan, T. V. & Stockman, M. I. *Plasmonics: Theory and applications. Plasmonics: Theory and Applications* (Springer Netherlands, 2013). doi:10.1007/978-94-007-7805-4
168. Wadell, C., Syrenova, S. & Langhammer, C. Plasmonic hydrogen sensing with nanostructured metal hydrides. *ACS Nano* **8**, 11925–11940 (2014).
169. Langhammer, C., Zorić, I., Kasemo, B. & Clemens, B. M. Hydrogen storage in Pd nanodisks characterized with a novel nanoplasmonic sensing scheme. *Nano Lett.* **7**, 3122–3127 (2007).
170. Rahm, J. M. *et al.* A Library of Late Transition Metal Alloy Dielectric Functions for Nanophotonic Applications. *Adv. Funct. Mater.* **30**, 2002122 (2020).
171. Gao, X. *et al.* Visual detection of microRNA with lateral flow nucleic acid biosensor. *Biosens. Bioelectron.* **54**, 578–84 (2014).
172. Unser, S., Bruzas, I., He, J. & Sagle, L. Localized Surface Plasmon Resonance Biosensing: Current Challenges and Approaches. *Sensors (Basel)*. **15**, 15684–716 (2015).
173. Kim, S.-W. *et al.* Easy-to-Fabricate and High-Sensitivity LSPR Type Specific Protein Detection Sensor Using AAO Nano-Pore Size Control. *Sensors* **17**, 856 (2017).
174. Bingham, J. M., Anker, J. N., Kreno, L. E. & Van Duyne, R. P. Gas Sensing with High-Resolution Localized Surface Plasmon Resonance Spectroscopy. *J. Am. Chem. Soc.* **132**, 17358–17359 (2010).
175. Chen, B., Liu, C., Xie, Y., Jia, P. & Hayashi, K. Localized Surface Plasmon Resonance Gas Sensor Based on Molecularly Imprinted Polymer Coated Au Nano-Island Films: Influence of Nanostructure on Sensing Characteristics. *IEEE Sens. J.* **16**, 3532–3540 (2016).
176. Joy, N. A. *et al.* Selective Plasmonic Gas Sensing: H<sub>2</sub>, NO<sub>2</sub>, and CO Spectral Discrimination by a Single Au-CeO<sub>2</sub> Nanocomposite Film. *Anal. Chem.* **84**, 5025–5034 (2012).
177. Nugroho, F. A. A. *et al.* Plasmonic Nanospectroscopy for Thermal Analysis of Organic Semiconductor Thin Films. *Anal. Chem.* **89**, 2575–2582 (2017).

178. Langhammer, C. & Larsson, E. M. Nanoplasmonic In Situ Spectroscopy for Catalysis Applications. *ACS Catal.* **2**, 2036–2045 (2012).
179. Langhammer, C., Larsson, E. M., Kasemo, B. & Zorić, I. Indirect nanoplasmonic sensing: Ultrasensitive experimental platform for nanomaterials science and optical nanocalorimetry. *Nano Lett.* **10**, 3529–3538 (2010).
180. Antosiewicz, T. J. *et al.* Plasmon-Assisted Indirect Light Absorption Engineering in Small Transition Metal Catalyst Nanoparticles. 1591–1599 (2015). doi:10.1002/adom.201500284
181. Susarrey-Arce, A. *et al.* A nanofabricated plasmonic core-shell-nanoparticle library. *Nanoscale* **11**, 21207–21217 (2019).
182. Liu, N., Tang, M. L., Hentschel, M., Giessen, H. & Alivisatos, A. P. Nanoantenna-enhanced gas sensing in a single tailored nanofocus. *Nat. Mater.* **10**, 631–6 (2011).
183. Yang, A. *et al.* Hetero-oligomer Nanoparticle Arrays for Plasmon-Enhanced Hydrogen Sensing. (2014). doi:10.1021/nn502502r
184. Syrenova, S., Wadell, C. & Langhammer, C. Shrinking-hole colloidal lithography: Self-aligned nanofabrication of complex plasmonic nanoantennas. *Nano Lett.* **14**, 2655–2663 (2014).
185. Bernardo, P., Drioli, E. & Golemme, G. Membrane gas separation: A review/state of the art. *Ind. Eng. Chem. Res.* **48**, 4638–4663 (2009).
186. Minelli, M. & Sarti, G. C. Elementary prediction of gas permeability in glassy polymers. *J. Memb. Sci.* **521**, 73–83 (2017).
187. Suloff, E. C. Sorption Behavior of an Aliphatic Series of Aldehydes in the Presence of Poly(ethylene terephthalate) Blends Containing Aldehyde Scavenging Agents. (Virginia Polytechnic Institute and State University, 2002).
188. Semicrystalline Polymers. in *Electron Microscopy of Polymers* 295–327 (Springer Berlin Heidelberg, 2008). doi:10.1007/978-3-540-36352-1\_17
189. Klopffer, M. H. & Flaconnèche, B. Transport Properties of Gases in Polymers: Bibliographic Review. *Oil Gas Sci. Technol.* **56**, 223–244 (2001).
190. Sastri, V. R. Materials Used in Medical Devices. in *Plastics in Medical Devices* 21–32 (Elsevier, 2010). doi:10.1016/b978-0-8155-2027-6.10003-0
191. Thomas, S., Wilson, R., Anil Kumar, S. & George, S. C. *Transport Properties of Polymeric Membranes*. *Transport Properties of Polymeric Membranes* (Elsevier, 2017). doi:10.1016/c2015-0-06823-x
192. Nagy, E. *Basic equations of mass transport through a membrane layer*. *Basic Equations of Mass Transport through a Membrane Layer* (Elsevier, 2018). doi:10.1016/C2016-0-04043-3
193. Selke, S. E. M., Culter, J. D., Selke, S. E. M. & Culter, J. D. *Plastics Packaging*. in *Plastics Packaging I–XX* (Carl Hanser Verlag GmbH & Co. KG, 2016). doi:10.3139/9783446437197.fm

194. Lasseuguette, E. & Ferrari, M. C. Polymer membranes for sustainable gas separation. in *Sustainable Nanoscale Engineering: From Materials Design to Chemical Processing* 265–296 (Elsevier, 2019). doi:10.1016/B978-0-12-814681-1.00010-2
195. V. P. Shantarovich, †, I. B. Kevdina, †, Yu. P. Yampolskii, \*, A. & Alentiev‡, A. Y. Positron Annihilation Lifetime Study of High and Low Free Volume Glassy Polymers: Effects of Free Volume Sizes on the Permeability and Permselectivity. *Macromolecules* **33**, 7453–7466 (2000).
196. Hofmann, D., Entrialgo-Castano, M., Lerbret, A., Heuchel, M. & Yampolskii, Y. Molecular modeling investigation of free volume distributions in stiff chain polymers with conventional and ultrahigh free volume: Comparison between molecular modeling and positron lifetime studies. *Macromolecules* **36**, 8528–8538 (2003).
197. Thran, A., Kroll, G. & Faupel, F. *Correlation Between Fractional Free Volume and Diffusivity of Gas Molecules in Glassy Polymers*. *J Polym Sci B: Polym Phys* **37**, (1999).
198. Choudalakis, G. & Gotsis, A. D. Permeability of polymer/clay nanocomposites: A review. *Eur. Polym. J.* **45**, 967–984 (2009).
199. Robeson, L. M., Smith, Z. P., Freeman, B. D. & Paul, D. R. Contributions of diffusion and solubility selectivity to the upper bound analysis for glassy gas separation membranes. *J. Memb. Sci.* **453**, 71–83 (2014).
200. Merkel, T. C., Bondar, V., Nagai, K., Freeman, B. D. & Yampolskii, P. Y. Gas sorption, diffusion, and permeation in poly(2,2-bis(trifluoromethyl)-4,5-difluoro-1,3-dioxole-co-tetrafluoroethylene). *Macromolecules* **32**, 8427–8440 (1999).
201. Hu, C. C., Chang, C. S., Ruan, R. C. & Lai, J. Y. Effect of free volume and sorption on membrane gas transport. *J. Memb. Sci.* **226**, 51–61 (2003).
202. Shishatskii, A. M., Yampol'skii, Y. P. & Peinemann, K. V. Effects of film thickness on density and gas permeation parameters of glassy polymers. *J. Memb. Sci.* **112**, 275–285 (1996).
203. Budd, P. M. & McKeown, N. B. Highly permeable polymers for gas separation membranes. *Polymer Chemistry* **1**, 63–68 (2010).
204. Dlubek, G., Pionteck, J., Rätzke, K., Kruse, J. & Faupel, F. Temperature dependence of the free volume in amorphous teflon AF1600 and AF2400: A pressure-volume-temperature and positron lifetime study. *Macromolecules* **41**, 6125–6133 (2008).
205. Fu, Y. J. *et al.* The correlation between free volume and gas separation properties in high molecular weight poly(methyl methacrylate) membranes. *Eur. Polym. J.* **43**, 959–967 (2007).
206. Wright, C. T. & Paul, D. R. Gas sorption and transport in poly(tertiary-butyl methacrylate). *Polymer (Guildf)*. **38**, 1871–1878 (1997).
207. Scholes, C. A., Kanehashi, S., Stevens, G. W. & Kentish, S. E. Water permeability and competitive permeation with CO<sub>2</sub> and CH<sub>4</sub> in perfluorinated polymeric membranes. *Sep. Purif. Technol.* **147**, 203–209 (2015).

208. Robeson, L. M. Correlation of separation factor versus permeability for polymeric membranes. *J. Memb. Sci.* **62**, 165–185 (1991).
209. Choudalakis, G. & Gotsis, A. D. Permeability of polymer/clay nanocomposites: A review. *European Polymer Journal* **45**, 967–984 (2009).
210. Nugroho, F. A. A. *et al.* Metal–polymer hybrid nanomaterials for plasmonic ultrafast hydrogen detection. *Nat. Mater.* **18**, 489–495 (2019).
211. Darmadi, I. *et al.* Bulk-Processed Pd Nanocube–Poly(methyl methacrylate) Nanocomposites as Plasmonic Plastics for Hydrogen Sensing. *ACS Appl. Nano Mater.* **3**, 8438–8445 (2020).
212. Sebók, B., Schülke, M., Réti, F. & Kiss, G. Diffusivity, permeability and solubility of H<sub>2</sub>, Ar, N<sub>2</sub>, and CO<sub>2</sub> in poly(tetrafluoroethylene) between room temperature and 180 °C. *Polym. Test.* **49**, 66–72 (2016).
213. Rowe, B. W., Freeman, B. D. & Paul, D. R. Physical aging of ultrathin glassy polymer films tracked by gas permeability. *Polymer (Guildf)*. **50**, 5565–5575 (2009).
214. Huang, Y. & Paul, D. R. Physical aging of thin glassy polymer films monitored by gas permeability. *Polymer (Guildf)*. **45**, 8377–8393 (2004).
215. Huang, Y., Wang, X. & Paul, D. R. Physical aging of thin glassy polymer films: Free volume interpretation. *J. Memb. Sci.* **277**, 219–229 (2006).
216. Wang, Y., He, J., Liu, C., Chong, W. H. & Chen, H. Thermodynamics versus Kinetics in Nanosynthesis. *Angew. Chemie Int. Ed.* **54**, 2022–2051 (2015).
217. Grumezescu, A. M. *Fabrication and Self-Assembly of Nanobiomaterials: Applications of Nanobiomaterials. Fabrication and Self-Assembly of Nanobiomaterials: Applications of Nanobiomaterials* (Elsevier Inc., 2016). doi:10.1016/C2015-0-00353-7
218. Capek, I. *Noble Metal Nanoparticles*. (Springer Japan, 2017). doi:10.1007/978-4-431-56556-7
219. Yu, Y. & Zhang, G. Colloidal Lithography. in *Updates in Advanced Lithography* **8**, 3–34 (InTech, 2013).
220. Colson, P., Henrist, C. & Cloots, R. Nanosphere Lithography: A Powerful Method for the Controlled Manufacturing of Nanomaterials. *J. Nanomater.* **2013**, 1–19 (2013).
221. Zhang, G. & Wang, D. Colloidal Lithography-The Art of Nanochemical Patterning. *Chem. - An Asian J.* **4**, 236–245 (2009).
222. Ai, B., Möhwald, H., Wang, D. & Zhang, G. Advanced Colloidal Lithography Beyond Surface Patterning. *Adv. Mater. Interfaces* **4**, 1600271 (2017).
223. Yang, S.-M., Jang, S. G., Choi, D.-G., Kim, S. & Yu, H. K. Nanomachining by Colloidal Lithography. *Small* **2**, 458–475 (2006).
224. Fredriksson, H. *et al.* Hole–Mask Colloidal Lithography. *Adv. Mater.* **19**, 4297–4302 (2007).

225. Albinsson, D., Nilsson, S., Antosiewicz, T. J., Zhdanov, V. P. & Langhammer, C. Heterodimers for in Situ Plasmonic Spectroscopy: Cu Nanoparticle Oxidation Kinetics, Kirkendall Effect, and Compensation in the Arrhenius Parameters. *J. Phys. Chem. C* **123**, 6284–6293 (2019).
226. Cookson, J. The Preparation of Palladium Nanoparticles. *Platin. Met. Rev.* **56**, 83–98 (2012).
227. Li, J., Wu, Q. & Wu, J. Synthesis of Nanoparticles via Solvothermal and Hydrothermal Methods. in *Handbook of Nanoparticles* 1–28 (Springer International Publishing, 2015). doi:10.1007/978-3-319-13188-7\_17-1
228. Patil, A. B. & Bhanage, B. M. Sonochemistry: A Greener Protocol for Nanoparticles Synthesis. in *Handbook of Nanoparticles* 1–20 (Springer International Publishing, 2015). doi:10.1007/978-3-319-13188-7\_4-1
229. Hsu, S.-W., Rodarte, A. L., Som, M., Arya, G. & Tao, A. R. Colloidal Plasmonic Nanocomposites: From Fabrication to Optical Function. *Chem. Rev.* **acs.chemrev.7b00364** (2018). doi:10.1021/acs.chemrev.7b00364
230. Ferhan, A. R. & Kim, D.-H. Nanoparticle polymer composites on solid substrates for plasmonic sensing applications. *Nano Today* **11**, 415–434 (2016).
231. Heilmann, A. *Polymer Films with Embedded Metal Nanoparticles*. **52**, (Springer Berlin Heidelberg, 2003).
232. Nugroho, F. A. A., Iandolo, B., Wagner, J. B. & Langhammer, C. Bottom-Up Nanofabrication of Supported Noble Metal Alloy Nanoparticle Arrays for Plasmonics. *ACS Nano* **10**, 2871–2879 (2016).
233. Ngene, P. *et al.* Polymer-Induced Surface Modifications of Pd-based Thin Films Leading to Improved Kinetics in Hydrogen Sensing and Energy Storage Applications. *Angew. Chemie Int. Ed.* **53**, 12081–12085 (2014).
234. Niu, W. *et al.* Seed-mediated growth of nearly monodisperse palladium nanocubes with controllable sizes. *Cryst. Growth Des.* **8**, 4440–4444 (2008).
235. Liu, X. *et al.* Facile synthesis of pd nanocubes with assistant of iodide and investigation of their electrocatalytic performances towards formic acid oxidation. *Nanomaterials* **9**, (2019).
236. Ul-Hamid, A. Contrast Formation in the SEM. in *A Beginners' Guide to Scanning Electron Microscopy* 77–128 (Springer International Publishing, 2018). doi:10.1007/978-3-319-98482-7\_3
237. Encyclopædia Britannica. Scanning electron microscope. *Encyclopædia Britannica* Available at: <https://www.britannica.com/technology/scanning-electron-microscope/media/526571/110970>. (Accessed: 20th February 2019)
238. Egerton, R. F. The Scanning Electron Microscope. in *Physical Principles of Electron Microscopy* 125–153 (Springer US, 2005). doi:10.1007/0-387-26016-1\_5
239. Physical Electronics, I. X-Ray Photoelectron Spectroscopy (XPS) Surface Analysis



- Technique. Available at: <https://www.phis.com/surface-analysis-techniques/xps-esca.html>. (Accessed: 21st February 2019)
240. Haasch, R. T. X-Ray Photoelectron Spectroscopy (XPS) and Auger Electron Spectroscopy (AES). in *Practical Materials Characterization* 93–132 (Springer New York, 2014). doi:10.1007/978-1-4614-9281-8\_3
  241. van der Heide, A. Introduction. in *X-Ray Photoelectron Spectroscopy* 1–12 (John Wiley & Sons, Inc., 2011). doi:10.1002/9781118162897.ch1
  242. Olefjord, I. X-ray photoelectron spectroscopy. in *Surface Characterization* 5, 291–319 (Wiley-VCH Verlag GmbH, 2013).
  243. X-ray Photoelectron Spectroscopy (XPS) Reference Pages: Palladium. Available at: <http://www.xpsfitting.com/search/label/Palladium>. (Accessed: 22nd February 2019)
  244. Sauerbrey, G. Verwendung von Schwingquarzen zur Wägung dünner Schichten und zur Mikrowägung. *Zeitschrift für Phys.* **155**, 206–222 (1959).
  245. Schnablegger, H. & Singh, Y. *The SAXS Guide*. (Anton Paar GmbH, 2013).
  246. cSAXS – X12SA: Coherent Small-Angle X-ray Scattering. Available at: <https://www.psi.ch/en/sls/csaxs>. (Accessed: 24th November 2020)
  247. Hübert, T., Majewski, J., Banach, U., Detjens, M. & Tiebe, C. Response Time Measurement of Hydrogen Sensors. in *undefined* (2017).
  248. Ortiz Cebolla, R. *et al.* Test methodologies for hydrogen sensor performance assessment: Chamber vs. flow-through test apparatus. *Int. J. Hydrogen Energy* **43**, 21149–21160 (2018).
  249. Ghosh, J., Chattopadhyay, S. K., Meikap, A. K., Chatterjee, S. K. & Chatterjee, P. Study of microstructure in vanadium-palladium alloys by X-ray diffraction technique. *Bull. Mater. Sci.* **30**, 447–454 (2007).
  250. Ott, D. & Raub, C. J. Grain size of gold and gold alloys - A review and some recent developments. *Gold Bull.* **14**, 69–74 (1981).
  251. Saini, A. An investigation of the cause of leak formation in palladium composite membranes. *Worcester Polytechnic Institute* (Worcester Polytechnic Institute, 2006).
  252. Gil, F. J., Picas, J. A., Manero, J. M., Forn, A. & Planell, J. A. Effect of the addition of palladium on grain growth kinetics of pure titanium. *J. Alloys Compd.* **260**, 147–152 (1997).
  253. Yau, A., Harder, R. J., Kanan, M. W. & Ulvestad, A. Imaging the Hydrogen Absorption Dynamics of Individual Grains in Polycrystalline Palladium Thin Films in 3D. *ACS Nano* **11**, 10945–10954 (2017).
  254. Masuda, T., Isobe, E., Higashimura, T. & Takada, K. Poly[1-(trimethylsilyl)-1-propyne]: A New High Polymer Synthesized with Transition-Metal Catalysts and Characterized by Extremely High Gas Permeability. *J. Am. Chem. Soc.* **105**, 7473–7474 (1983).
  255. Mc Keown, N. B. & Budd, P. M. Polymers of intrinsic microporosity (PIMs): Organic

materials for membrane separations, heterogeneous catalysis and hydrogen storage. *Chem. Soc. Rev.* **35**, 675–683 (2006).

256. Nojiri, K. Mechanism of Dry Etching. in *Dry Etching Technology for Semiconductors* 11–30 (Springer International Publishing, 2015). doi:10.1007/978-3-319-10295-5\_2